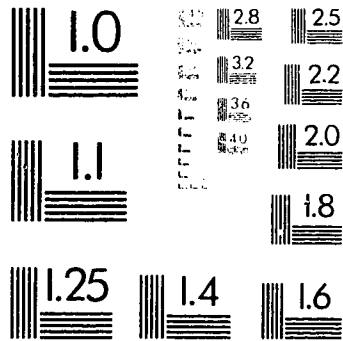




PM-1 3½"x4" PHOTOGRAPHIC MICROCOPY TARGET  
NBS 1010a ANSI/ISO #2 EQUIVALENT



PRECISION<sup>SM</sup> RESOLUTION TARGETS

**UNIVERSITY OF ALBERTA**

**FINITE ELEMENT ANALYSIS OF A LARGE PRESSURIZED VESSEL  
AND LAMINATED CYLINDRICAL VESSELS**

by

**PAUL C. GIVENS**



**A thesis submitted to the Faculty of Graduate Studies in partial fulfillment of the  
requirements for the degree of Masters of Science**

**Department of Mechanical Engineering**

**Edmonton, Alberta**

**Fall, 1996**



National Library  
of Canada

Acquisitions and  
Bibliographic Services Branch

395, Wellington Street  
Ottawa, Ontario  
K1A 0N4

Bibliothèque nationale  
du Canada

Direction des acquisitions et  
des services bibliographiques

395, rue Wellington  
Ottawa (Ontario)  
K1A 0N4

*Your file: Votre référence*

*Our file: Notre référence*

**The author has granted an irrevocable non-exclusive licence allowing the National Library of Canada to reproduce, loan, distribute or sell copies of his/her thesis by any means and in any form or format, making this thesis available to interested persons.**

**L'auteur a accordé une licence irrévocable et non exclusive permettant à la Bibliothèque nationale du Canada de reproduire, prêter, distribuer ou vendre des copies de sa thèse de quelque manière et sous quelque forme que ce soit pour mettre des exemplaires de cette thèse à la disposition des personnes intéressées.**

**The author retains ownership of the copyright in his/her thesis. Neither the thesis nor substantial extracts from it may be printed or otherwise reproduced without his/her permission.**

**L'auteur conserve la propriété du droit d'auteur qui protège sa thèse. Ni la thèse ni des extraits substantiels de celle-ci ne doivent être imprimés ou autrement reproduits sans son autorisation.**

ISBN 0-612-18263-0

**Canada**

University of Alberta

**Library Release Form**

**Name of Author:** Paul Christopher Givens

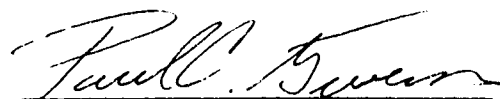
**Title of Thesis:** Finite Element Analysis of a Large Pressurized Vessel and Laminated Cylindrical Vessels

**Degree:** Masters of Science

**Year this Degree Granted:** 1996

Permission is hereby granted to the University of Alberta to reproduce single copies of this thesis and to lend or sell such copies for private, scholarly, or scientific research purposes only.

The author reserves all other publication and other rights in association with the copyright in the thesis, and except as hereinbefore provided, neither the thesis nor any substantial portion thereof may be printed or otherwise reproduced in any material form whatever without the author's prior written permission.



10917 University Avenue  
Edmonton, Alberta, Canada  
T6G 1Y1

October 4, 1996

**University of Alberta**

**Faculty of Graduate Studies and Research**

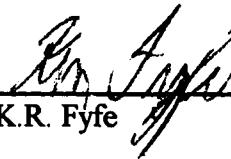
The undersigned certify that they have read, and recommended to the Faculty of Graduate Studies and Research for acceptance, a thesis entitled *Finite Element Analysis of a Large Pressurized Vessel and Laminated Cylindrical Vessels* submitted by Paul Christopher Givens in partial fulfillment of the requirements for the degree of Masters of Science,



Dr. F. Ellyin



Dr. A.W. Lipsett



Dr. K.R. Fyfe



Dr. B. Patchett

## ABSTRACT

Both large steel pressurized vessels and pressurized laminated cylindrical shells represent engineering problems for which there are no analytical solutions. A method of stress analysis of Syncrude Canada Limited's two coker burner large steel pressurized vessels is necessary because of planned increases in the vessels' design loads and a history of fatigue crack failures. Pressurized laminated cylindrical shells are an attractive alternative to shells made of conventional engineering materials. However, the ply stacking sequence of laminated shells must be custom designed for the end-use loading conditions in order to most competitively use the material.

A method is developed whereby a detailed stress/strain analysis of the coker burner pressurized vessels and the laminated cylindrical shells with  $(+\theta, -\theta, +\theta, +\theta, -\theta, +\theta)$  and multi-directional lay-up angles could be performed. This is accomplished by developing and testing finite element models for use with the ANSYS program. Thus, the stress/strain response of the burner vessels subjected to internal pressure and the laminated shells subjected to internal pressure and axial load is obtained.

Emphasis is given to discussion of the results for the burner vessel nozzle-shell intersections, and an elastic-plastic limit load calculation is presented for two of the nozzle-shell intersections subjected to combined internal pressure and external nozzle loads. Elastic peak stress results were compared against experiments and found to be 50% lower. Out-of-plane bending was determined to be more critical than in-plane bending and shear forces in the elastic-plastic case.

The results for the laminated shells are used to demonstrate both the rationale for describing the response of the shells in terms of strain rather than stress, and that the radial displacement is smallest for angles of  $\theta$  greater than  $70^\circ$ .

## TABLE OF CONTENTS

	<u>Page</u>
CHAPTER 1 FINITE ELEMENT ANALYSIS OF A LARGE PRESSURIZED VESSEL AND LAMINATED CYLINDRICAL SHELLS	1
1.1 INTRODUCTION	1
1.2 ANALYSIS OF A LARGE STEEL PRESSURIZED VESSEL	2
1.3 ANALYSIS OF PRESSURIZED LAMINATED CYLINDRICAL SHELLS	3
ANALYSIS OF A LARGE STEEL PRESSURIZED VESSEL	
CHAPTER 2 ELASTIC ANALYSIS OF A LARGE STEEL PRESSURIZED VESSEL	6
2.1 INTRODUCTION	6
2.1.1 The Coker Burner Pressure Vessels	6
2.1.2 'Coker 2000'	7
2.1.3 Context of this Finite Element Analysis	8
2.1.4 Benefits from Performing this Finite Element Analysis	9
2.2 REVIEW OF DESIGN METHODS	10
2.2.1 Design by Rules	10
2.2.2 Design by Analysis	11
2.2.3 Hydrostatic Testing	13
2.3 PHYSICAL CONDITIONS	13
2.3.1 Vessel Geometry	13
2.3.2 Attachment Geometry	14
2.3.3 Fabrication Material	14
2.4 FINITE ELEMENT MODEL	15
2.4.1 FEA Software and Hardware	15
2.4.2 Submodeling Technique	16

2.4.3	Major Openings	16
2.4.4	Global Model	17
2.4.5	Submodels	18
2.5	INTERNAL PRESSURE CONDITIONS	19
2.5.1	Simulated Loading	19
2.5.2	Boundary Conditions	20
2.6	RESULTS FROM INTERNAL PRESSURE SIMULATION	21
2.6.1	Global Model Results	21
2.6.2	Submodel Results	23
2.6.3	Convergence of Stress	25
2.6.4	Comparison to Physical Experiments	26
2.6.5	Evaluating Finite Element Results	27
2.7	DISCUSSION AND SUMMARY OF RESULTS	29
2.8	CONCLUSIONS	30
CHAPTER 3	ELASTIC-PLASTIC ANALYSIS OF A LARGE STEEL PRESSURIZED VESSEL SUBJECTED TO NOZZLE EXTERNAL LOADS	65
3.1	INTRODUCTION	65
3.2	PHYSICAL CONDITIONS	66
3.2.1	Nozzle Geometry	66
3.2.2	Fabrication Material	67
3.3	FINITE ELEMENT MODEL	68
3.3.1	FEA Software and Hardware	68
3.3.2	Hardening Behaviour	68
3.4	LOADING AND BOUNDARY CONDITIONS	69
3.4.1	Direction Notation	69
3.4.2	Boundary Conditions	70
3.4.3	Applied Loads	70
3.5	RESULTS	71
3.5.1	Plastic Limit Loads	71
3.5.2	Allowable Load	74



3.5.3	Effect of Substep Size	75
3.5.4	Effect of Element Size	76
3.6	DISCUSSION OF RESULTS	76
3.7	SUMMARY OF RESULTS	78
3.8	CONCLUSIONS	79

## ANALYSIS OF PRESSURIZED LAMINATED CYLINDRICAL SHELLS

CHAPTER 4	ANALYSIS OF PRESSURIZED $\pm\theta$ LAMINATED CYLINDRICAL SHELLS	113
4.1	INTRODUCTION	113
4.2	GEOMETRY	114
4.3	FINITE ELEMENT ANALYSIS	115
4.4	BIAXIAL LOAD RATIOS	116
4.5	RESULTS	117
4.6	EFFECT OF ELEMENT SIZE	118
4.7	COMPARISON TO PHYSICAL EXPERIMENTS	118
4.8	DISCUSSION	119
4.9	CONCLUSIONS	121
CHAPTER 5	ANALYSIS OF PRESSURIZED MULTI-DIRECTIONAL LAMINATED CYLINDRICAL SHELLS	133
5.1	INTRODUCTION	133
5.2	GEOMETRY	134

5.3	FINITE ELEMENT MODEL	134
5.4	BIAXIAL LOAD RATIOS	135
5.5	RESULTS	136
5.6	COMPARISON TO PHYSICAL EXPERIMENTS	137
5.7	DISCUSSION	138
5.8	CONCLUSIONS	140
CHAPTER 6	CONCLUSIONS	149
APPENDIX A	SUBMODELLING TECHNIQUE DETAILS	153
APPENDIX B	SHELL ELEMENT DETAILS	155
APPENDIX C	PLASTIC LIMIT LOAD DETAILS	158
APPENDIX D	BRICK ELEMENT DETAILS	162

## LIST OF TABLES

Table 1-1	Description of Nozzles and Manways	32
Table 2-2	Details of Nozzles and Manways	33
Table 2-3	Design Temperatures and Pressures	34
Table 2-4	Summary of Far-Field Comparison	34
Table 2-5	Details of Nozzle S6 and a Nozzle from the Literature	34
Table 3-1	Calculated Limit Loads for Nozzles S6 and N7	81
Table 4-1	Biaxial Load Ratios Considered	123
Table 4-2	Accuracy of $\pm 55^\circ$ Finite Element Results Based on Physical Experiments	123
Table 5-1	Biaxial Load Ratios Considered	142

## LIST OF FIGURES

Figure 1-1	A photograph of the two coker burner vessels at Syncrude Canada Limited, Mildred Lake, Alberta.	5
Figure 2-1	A plot of the lines of the global model.	35
Figure 2-2	A plot of the element discretization of the global model.	36
Figure 2-3	A plot of the element discretization of Submodel N7.	37
Figure 2-4	A plot of the global model nodes showing the internal pressure loading.	38
Figure 2-5	A plot of global model nodes showing the prescribed boundary conditions.	39
Figure 2-6	A plot of the numerically predicted circumferential stress developed in the top head near nozzle S6 under pure internal pressure loading.	40
Figure 2-7	Variation in the circumferential and longitudinal stress components along a longitudinal cut through nozzle S6 with the distance from the nozzle-shell juncture, non-dimensionalized through dividing by the nozzle diameter. The far-field stress from shell theory [9] is superimposed on this plot.	41
Figure 2-8	Circumferential and longitudinal stress developed in the submodels under internal pressure	
(a)	Submodel N7 - Circumferential Stress	42
(b)	Submodel N7 - Longitudinal Stress	43
(c)	Submodel S1 - Circumferential Stress	44
(d)	Submodel S1 - Longitudinal Stress	45
(e)	Submodel S2 - Circumferential Stress	46

(f)	Submodel S2 - Longitudinal Stress	47
(g)	Submodel S3 - Circumferential Stress	48
(h)	Submodel S3 - Longitudinal Stress	49
(i)	Submodel S5 - Circumferential Stress	50
(j)	Submodel S5 - Longitudinal Stress	51
(k)	Submodel S6 - Circumferential Stress	52
(l)	Submodel S6 - Longitudinal Stress	53
(m)	Submodel S10 - Circumferential Stress	54
(n)	Submodel S10 - Longitudinal Stress	55

Figure 2-9 Deflected shape due to interanal pressure superimposed over the undeformed shape for a circumferential and longitudinal cut through each submodel.

(a)	Submodel N7 - Circumferential Cut	56
(b)	Submodel N7 - Longitudinal Cut	56
(c)	Submodel S1 - Circumferential Cut	57
(d)	Submodel S1 - Longitudinal Cut	57
(e)	Submodel S2 - Circumferential Cut	58
(f)	Submodel S2 - Longitudinal Cut	58
(g)	Submodel S3 - Circumferential Cut	59
(h)	Submodel S3 - Longitudinal Cut	59
(i)	Submodel S5 - Circumferential Cut	60
(j)	Submodel S5 - Longitudinal Cut	60
(k)	Submodel S6 - Longitudinal Cut	61
(l)	Submodel S10 - Longitudinal Cut	61

Figure 2-10 Results of a physical experiment showing the trend of the normal and circumferential stress components for a radial cylindrical nozzle in a spherical head [11].

62

Figure 2-11 Variation of normal and tangential components of stress with distance from the juncture for Submodel S6 subjected to internal pressure. The far-field stress from shell theory [9] is superimposed on this plot.

62

Figure 3-1 A plot of the cyclic curve for ASTM A-516 Grade 70 mild steel [12] the piecewise linear approximation of the cyclic curve.

82

Figure 3-2	Definition of inplane and outplane directions.	82
Figure 3-3	Equivalent stress due to the boundary conditions only.	83
Figure 3-4a	Submodel S6 subjected to a simulated outplane moment.	84
Figure 3-4b	Submodel S6 subjected to a simulated inplane shear force.	85
Figure 3-4c	Submodel N7 subjected to a simulated inplane shear force.	86
Figure 3-4d	Submodel N7 subjected to a simulated outplane shear force.	87
Figure 3-4e	Submodel N7 subjected to a simulated inplane moment.	88
Figure 3-4f	Submodel N7 subjected to a simulated outplane moment.	89
Figure 3-5	Definition of plastic limit, or limit load, and allowable load.	90
Figure 3-6a	Bending moment verses displacement for Submodel S6 subjected to an outplane bending moment.	91
Figure 3-6b	Shearing load verses displacement for Submodel S6 subjected to an inplane shear force.	91
Figure 3-6c	Shearing load verses displacement for Submodel N7 subjected to and inplane shear force.	92
Figure 3-6d	Shearing load verses displacement for Submodel N7 subjected to an outplane shear force.	92

Figure 3-6e	Bending moment displacement for Submodel N7 subjected to an inplane moment.	93
Figure 3-6f	Bending moment verses displacement for Submodel N7 subjected to an outplane moment.	93
Figure 3-7a	Moment verses displacement for Submodel S6.	94
Figure 3-7b	Moment verses displacement for Submodel N7.	94
Figure 3-8	Inplane moment verses displacement indicated by dial gauges [11].	95
Figure 3-9a	Equivalent plastic strain distribution at the plastic limit for Submodel S6 subjected to an outplane moment.	96
Figure 3-9b	Equivalent plastic strain distribution at the plastic limit for Submodel S6 subjected to an inplane shear.	97
Figure 3-9c	Equivalent plastic strain distribution at the plastic limit for Submodel N7 subjected to an inplane shear.	98
Figure 3-9d	Equivalent plastic strain distribution at the plastic limit for Submodel N7 subjected to an outplane shear.	99
Figure 3-9e	Equivalent plastic strain distribution at the plastic limit for Submodel N7 subjected to an inplane moment.	100
Figure 3-9f	Equivalent plastic strain distribution at the plastic limit for Submodel N7 subjected to an outplane moment.	101

Figure 3-10a	Equivalent stress distribution at the plastic limit for Submodel S6 subjected to an outplane moment.	102
Figure 3-10b	Equivalent stress distribution at the plastic limit for Submodel S6 subjected to an inplane shear force.	103
Figure 3-10c	Equivalent stress distribution at the plastic limit for Submodel N7 subjected to an inplane shear force.	104
Figure 3-10d	Equivalent stress distribution at the plastic limit for Submodel N7 subjected to an outplane shear force.	105
Figure 3-10e	Equivalent stress distribution at the plastic limit for Submodel N7 subjected to an inplane moment.	106
Figure 3-10f	Equivalent stress distribution at the plastic limit for Submodel N7 subjected to an outplane moment.	107
Figure 3-11a	Moment verses displacement for Submodel S6 subjected to an outplane moment.	108
Figure 3-11b	Moment verses displacement for Submodel N7 subjected to an outplane moment.	108
Figure 3-12	Moment verses displacement for Submodel S6 subjected to an outplane moment.	109
Figure 4-1	Geometry of the Finite Element Analysis Model	124



- Figure 4-2a Radial displacement response verses stacking angle  $\theta$  for a biaxial load ratio of H0:A1. The radial displacements for  $(+70^\circ, -70^\circ, 0^\circ)_S$  and  $(+90^\circ, -90^\circ, 0)_S$  are also shown, as well as an experimental result for  $\pm 55^\circ$ . 125
- Figure 4-2b Radial displacement response verses stacking angle  $\theta$  for a biaxial load ratio of H1:A3. The radial displacements for  $(+70^\circ, -70^\circ, 0^\circ)_S$  and  $(+90^\circ, -90^\circ, 0)_S$  are also shown. 125
- Figure 4-2c Radial displacement response verses stacking angle  $\theta$  for a biaxial load ratio of H1:A2. The radial displacements for  $(+70^\circ, -70^\circ, 0^\circ)_S$  and  $(+90^\circ, -90^\circ, 0)_S$  are also shown. 126
- Figure 4-2d Radial displacement response verses stacking angle  $\theta$  for a biaxial load ratio of H1:A1. The radial displacements for  $(+70^\circ, -70^\circ, 0^\circ)_S$  and  $(+90^\circ, -90^\circ, 0)_S$  are also shown, as well as an experimental result for  $\pm 55^\circ$ . 126
- Figure 4-2e Radial displacement response verses stacking angle  $\theta$  for a biaxial load ratio of H3:A2. The radial displacements for  $(+70^\circ, -70^\circ, 0^\circ)_S$  and  $(+90^\circ, -90^\circ, 0)_S$  are also shown. 127
- Figure 4-2f Radial displacement response verses stacking angle  $\theta$  for a biaxial load ratio of H2:A1. The radial displacements for  $(+70^\circ, -70^\circ, 0^\circ)_S$  and  $(+90^\circ, -90^\circ, 0)_S$  are also shown, as well as an experimental result for  $\pm 55^\circ$ . 127
- Figure 4-2g Radial displacement response verses stacking angle  $\theta$  for a biaxial load ratio of H3:A1. The radial displacements for  $(+70^\circ, -70^\circ, 0^\circ)_S$  and  $(+90^\circ, -90^\circ, 0)_S$  are also shown. 128
- Figure 4-2h Radial displacement response verses stacking angle  $\theta$  for a biaxial load ratio of H4:A1. The radial displacements for  $(+70^\circ, -70^\circ, 0^\circ)_S$  and  $(+90^\circ, -90^\circ, 0)_S$  are also shown. 128

Figure 4-2i	Radial displacement response verses stacking angle $\theta$ for a biaxial load ratio of H2:A0. The radial displacements for $(+70^\circ, -70^\circ, 0^\circ)_S$ and $(+90^\circ, -90^\circ, 0)_S$ are also shown, as well as an experimental result for $\pm 55^\circ$ .	129
Figure 4-3	Stacking angle for minimum radial dilation verses hoop-to-axial load ratio.	129
Figure 4-4a	Variation of hoop stress through the thickness for a biaxial load ratio of 2H:1A.	130
Figure 4-4b	Variation of axial stress through the thickness for a biaxial load ratio of 2H:1A.	130
Figure 4-4c	Variation of radial stress through the thickness for a biaxial load ratio of 2H:1A.	131
Figure 4-4d	Variation of in-plane shear stress through the thickness for a biaxial load ratio of 2H:1A.	131
Figure 5-1	Sketch of tube geometry and direction notation.	143
Figure 5-2a	Variation of stress through the thickness for a biaxial load ratio of 1H:0A.	144
Figure 5-2b	Variation of stress through the thickness for a biaxial load ratio of 2H:1A.	144
Figure 5-2c	Variation of stress through the thickness for a biaxial load ratio of 1H:1A.	145

Figure 5-2d	Variation of stress through the thickness for a biaxial load ratio of 0H:1A.	145
Figure 5-3a	Variation of strain through the thickness for a biaxial load ratio of 1H:0A. The measured strain from a physical experiment [3] is superimposed on this plot.	146
Figure 5-3b	Variation of strain through the thickness for a biaxial load ratio of 2H:1A. The measured strain from a physical experiment [3] is superimposed on this plot.	146
Figure 5-3c	Variation of strain through the thickness for a biaxial load ratio of 1H:1A. The measured strain from a physical experiment [3] is superimposed on this plot.	147
Figure 5-3d	Variation of strain through the thickness for a biaxial load ratio of 0H:1A. The measured strain from a physical experiment [3] is superimposed on this plot.	147
Figure A-1	Example of the submodelling technique. The finite element displacement results from the global model analysis are prescribed as displacement boundary conditions on the cut boundary of the submodel.	154
Figure B-1	Direction notation and nodal labelling for SHELL93 nodal degrees of freedom.	155
Figure C-1	Bending moment verses displacement for Submodel S6 subjected to an outplane bending moment.	159
Figure C-2	Shearing load verses displacement for Submodel S6 subjected to an inplane shear force.	159

Figure C-3	Shearing load verses displacement for Submodel N7 subjected to an inplane shear force.	160
Figure C-4	Shearing load verses displacement for Submodel N7 subjected to an outplane shear force.	160
Figure C-5	Bending moment displacement for Submodel N7 subjected to an inplane moment.	161
Figure C-6	Bending moment verses displacement for Submodel N7 subjected to an outplane moment.	161
Figure D-1	Direction notation for SOLID64 displacements and nodal degrees of freedom.	162

## LIST OF SYMBOLS

All nomenclature is listed in the order of appearance in text.

I.D.	inner diameter
$E$	modulus of elasticity
$\nu$	Poisson's Ratio
$S_y$	Yield Stress
$S_u$	Tensile Strength
FEA	finite element analysis
$d_i$	inside diameter of nozzle
$D_i$	inside diameter of shell (sphere or cylinder)
$D_m$	mean diameter of shell (sphere or cylinder)
$d_m$	mean diameter of nozzle
$T$	thickness of shell
$t$	thickness of nozzle
$P$	internal pressure
$S$	stress in shell calculated by mean diameter formula, for cylinders (= $PD_m/(2T)$ ) and for spheres (= $PD_m/(4T)$ )
$s$	stress in nozzle calculated by mean diameter formula (= $Pd_m/(2t)$ )
$d_i/D_i$	diameter ratio
$D_i/T$	diameter-to-thickness ratio
$s/S$	stress ratio

$t/T$	thickness ratio
$S_m$	maximum allowable stress intensity <sup>1</sup> ( = smaller of $2S_y/3$ or $S_u/3$ )
$t/T$	thickness ratio
T.L.	tangent line of head-shell joint
$u/d$	distance $u$ from a nozzle/shell intersection normalized by the nozzle mean diameter $d$ ; $u$ is positive along the shell and negative along the nozzle.
$UZ$	nodal degree of freedom parallel to global z-axis
$\sigma_n$	stress component normal to a cut
$\sigma_t$	stress component tangential to a cut
$\sigma_H$	circumferential (hoop) stress component
$\epsilon$	strain
$\sigma$	stress
$E_0$	least squares fit coefficient
$n$	cyclic strain hardening coefficient
$\theta$	ply orientation angle
$E_1$	elastic modulus parallel to fibre orientation
$E_2$	elastic modulus transverse to fibre orientation

---

<sup>1</sup> The term stress intensity used in this thesis is as defined by the ASME Code Section 8 Division 2. Specifically, the stress intensity is equal to two times the Tresca stress value. This use of stress intensity should be distinguished from that used in the study of fracture mechanics.

$\nu_{12}$	Poisson's ratio
$G_{12}$	shear modulus
$H:A$	ratio of average hoop (H) stress to average axial (A) stress
$\sigma_{\theta}$	transverse shear stress component
$\sigma_r$	transverse shear stress component
$a$	inside radius of tube
$\sigma_{\theta\theta}$	circumferential stress component
$\sigma_{rr}$	radial stress component
$\sigma_{zz}$	axial stress component
$\mu s$	$10^{-6}$ in./in.
$p$	internal pressure
$\sigma_{\theta r}$	in-plane shear stress component

**CHAPTER 1**  
**FINITE ELEMENT ANALYSIS OF A LARGE PRESSURIZED VESSEL**  
**AND LAMINATED CYLINDRICAL SHELLS**

**1.1 INTRODUCTION**

Designers of large steel pressurized vessels and pressurized laminated cylindrical shells are presented with engineering problems for which there are no analytical solutions. However, this thesis demonstrates that the finite element method can be applied to such internal pressure problems in order to obtain a solution that provides results that are useful to designers. It further details verification of the results and reminds the reader that since the nature of these problems are such that there are no analytical results with which to compare to the finite element results, the finite element results must be used and interpreted with some caution and by persons trained in finite element methods.

Chapters 2 and 3 of this thesis present the analysis of a large steel pressurized vessel. Chapters 4 and 5 present the analysis of pressurized laminated cylindrical shells. In none of the cases presented is there an analytical solution that is available to designers.



## **1.2 ANALYSIS OF A LARGE STEEL PRESSURIZED VESSEL**

Syncrude Canada Limited's coker burner pressure vessels 8-1C-2 and 8-2C-2 are two similar steel pressure vessels 54 feet [17 m] in diameter and 68 feet [21 m] tall and critical components of Syncrude Canada Limited's Mildred Lake Upgrading Plant; Figure 1-1 is a photograph of the coker burner pressure vessels. These pressure vessels have frequently been in need of repairs and replacement parts. When such a problem occurs at a location where the vessel shell has been pierced for a nozzle opening, designers are required to perform a stress analysis in order to effect a temporary repair, such as a leak-box, and/or fabricate a replacement part. The extremely large size of these vessels and the 14 nozzles piercing them represent complex geometry such that obtaining required information using analytical methods is difficult or impossible.

A method is developed whereby detailed elastic stress/strain analysis of the nozzle-shell intersection regions of the coker burner vessels could be performed. This is accomplished by developing a finite element model for use with the commercial program ANSYS, a program that is currently available on-site at Syncrude. This model is tested using an internal pressure load case. The results from this analysis are discussed in terms of stress and are shown to compare well with the published experimental data.

The finite element model developed herein hence offers three key advantages. The first is that it includes all of the major openings into the vessel. The second is that it can predict the deformed geometry under a particular load case. Finally, the developed model can easily facilitate numerical experimentation of new nozzle-shell juncture configurations.

The design methods used in the pressure vessel industry to determine limits on external loads applied to nozzles are generally based on approximate approaches with large factors of safety. Although these large factors of safety compensate for the unknown and omitted items, the resulting components are heavily over-designed. This practice is not cost effective and wastes both material and fabrication time. Such practice also leads to thick reinforcements and as such can cause high thermal gradients in the shell wall.

A method is developed with which an elastic-plastic analysis of two of the nozzles opening into the burner vessels could be performed. This is accomplished by developing models of the nozzle/shell intersections which take into account the nonlinear stress-strain response of the material. An analysis of the two nozzles was performed using the ANSYS program. The results from this analysis are used to determine the plastic limits of the nozzle-shell juncture region subjected to combined external loading and internal pressure. A design approach using this plastic limit load is discussed.

### **1.3 ANALYSIS OF PRESSURIZED LAMINATED CYLINDRICAL SHELLS**

Laminated fibre reinforced plastics (FRP) cylindrical shells are a cost effective alternative to conventional materials in piping products, downhole tubes, and projectile casings and barrels. Since the mechanical properties of laminated shells are strongly dependent upon the ply stacking sequence of the lamina layers, this sequence must be custom designed for the particular end use loading conditions in order to most effectively and competitively use the material.

A method is developed which can predict the lamina lay-up sequence for laminated cylindrical shells subjected to combined internal pressure and axial loading that yields minimum diametral strain. This is accomplished using the finite element method to model the lamina lay-up  $(+\theta, -\theta, +\theta, +\theta, -\theta, +\theta)$  subjected to combined internal pressure and axial loading. A finite element stress and strain analysis was performed using the ANSYS program, and a comparison between the strain response of the various laminates was carried out to determine the lay-up offering the least diametral strain.

The highest fibre angle for which laminated FRP shells can be continuously wound is approximately  $70^\circ$ . The effect that this manufacturing limitation has on diametral strain is determined.

The stress/strain response of multi-directional laminate cylindrical shells subjected to biaxial loading is determined. This is accomplished using the finite element method to model a stacking sequence of  $[\pm 70^\circ, \pm 45^\circ, \pm 45^\circ, +70^\circ, 0^\circ, -45^\circ, \pm 45^\circ, \pm 45^\circ, \pm 45^\circ, \pm 45^\circ]$  as an axisymmetric cylindrical shell. Internal pressure and axial load conditions were simulated. A finite element stress and strain analysis was performed using the ANSYS program, and the stress and strain distribution through the wall thickness of the shells are plotted.



Figure 1-1: A photograph of the two coker burner pressure vessels at Syncrude Canada Limited, Mildred Lake, Alberta.

## **ANALYSIS OF A LARGE STEEL PRESSURIZED VESSEL**

Syncrude Canada Limited's two coker burner pressure vessels represent internal pressure problems that cannot currently be solved using analytical methods. Chapters Two and Three of this thesis present solutions to pressure vessel problems that are obtained by applying the finite element method and the submodelling technique in a new way.

### **CHAPTER 2**

#### **ELASTIC ANALYSIS OF A LARGE STEEL PRESSURIZED VESSEL**

##### **2.1 INTRODUCTION**

###### **2.1.1 The Coker Burner Pressure Vessels**

The two coker burner vessels, serial numbers 8-1C-2 and 8-2C-2, (hereafter referred to as the burner vessels) at Syncrude Canada Limited's Primary Upgrading plant are critical components of Syncrude Canada Limited's Plant 8 fluid coking process. This process involves spraying bitumen, a heavy tar-like oil extracted from mined oil sand, through nozzles into one of two heated chambers called the coker pressure vessels (cokers). Inside the cokers the bitumen molecules "crack" into gas, naphtha, gas oil, and coke. The heat required for the cracking process is provided by burning some of the product coke in the burner vessels and by returning the hot coke to the cracking chamber.

The coke is returned to the cokers through piping that connects the cokers and the burner vessels and is propelled through the piping using steam injected standpipes.

The injection of steam into these standpipes produces cyclic loading and vibration of the standpipes [1]. This type of vibration has previously been determined by metallurgical examination to be the cause of through thickness fatigue cracking at the intersection of a major nozzle piercing the burner vessel [2, 3]. Through thickness cracking of an operating pressure vessel requires an immediate repair, and for a case in which the failure occurs because of fatigue effects, a replacement part needs to be designed with an adequate fatigue life.

The burner vessels were originally designed to meet the requirements of the ASME Boiler and Pressure Vessel Code Section VIII Division 1 only. Therefore, none of the burner vessel components were designed to resist fatigue failures due to cyclic service by the vessels' vendor. The Division 1 design methodology is not currently considered to be adequate to meet the loading requirements of the burner pressure vessels.

A photograph of the coker burner vessels is shown in Figure 1-1.

### **2.1.2 Coker 2000**

Syncrude Canada Limited established in 1995 a corporate goal of producing 90 million barrels of Syncrude Sweet Blend (SSB) oil. A key milestone of this goal is called 'Coker 2000'. The purpose of this project is to increase the process load on the cokers and the burner pressure vessels until these vessels are running at one and a half times their

original capacity. This project is to be completed by the year 2000.

One of the major obstacles of this project is that these vessels are already operating at their maximum allowable working pressures. Therefore, a sophisticated analysis method, such as the one demonstrated in this chapter, is required in order to demonstrate that the vessels' design is adequate to carry the load increases that will accomplish 'Coker 2000'.

### **2.1.3 Context of this Finite Element Analysis**

A stress and strain analysis of the nozzle-vessel intersections is required in the case of both temporary repairs and reinforcements, as well as for the design and installation of replacement components. An analytical analysis of the nozzle/shell intersection problem is difficult or impossible for many practical configurations, such as those with reinforcement pads.

It was the objective of this project to develop a tool with which Syncrude Canada Limited could perform on-site stress/strain analyses of the entire burner pressure vessel using the finite element method. This project was unique from previous finite element analyses [3] in that it considered the entire vessel with all of the major openings. This was accomplished by applying the submodelling technique in a new way.

#### **2.1.4 Benefits from Performing this Finite Element Analysis**

The development of the burner vessel finite element model provides the designers at Syncrude Canada Limited a tool with which detailed stress/strain analyses of the vessel and its components can be performed. This tool can be used to demonstrate that the burner pressure vessels' design is adequate to carry the steadily increasing design loads required to accomplish 'Coker 2000' . Further, it can be used compare alternate configurations for replacement components, as well as to predict and compare an estimate of the fatigue life that can be expected from existing and replacement components.

Most of the openings into the burner vessel have been designed with heavy reinforcement pads on the shell side of the nozzle-shell juncture. However, numerical and physical experiments indicate that to minimize the stress in the shell, the reinforcement material should be added to the nozzle thickness instead of the shell thickness [4, 5]. It was found by the present analysis that for the case of pure internal pressure loading heavy reinforcement of the shell resulted in relatively high local stresses in the shell at the outside edge of the reinforcing pads.

Finally, the method that is developed for analysing the burner pressure vessels can be used for analysing pressure vessels in general. This method is obtained by applying the finite element method and the submodelling technique in a new way. The developed method allows a pressure vessel such as the burner vessel to be modelled complete with all of the openings piercing the vessel.



## **2.2 REVIEW OF DESIGN METHODS**

All pressure vessels that are in service in Canada and the United States are required by the respective national legislation to meet the design criteria of the ASME Boiler and Pressure Vessel Code Section VIII. Section VIII of this code is divided into two different design methodologies: Division 1, called Design by Rules, and Division 2, called Design by Analysis. The following Sections 2.2.1 and 2.2.2 of this thesis detail the use of these codes, as well as some limitations.

### **2.2.1 Design by Rules**

Division 1 presents a method of pressure vessel design termed *design by rules*. These rules make use of standard configurations that experience has shown are adequate to carry pressure loading. Non-standard configurations for welded joints, nozzle-shell intersections, and reinforcement strategies as detailed in the code are not permitted according to the rules of Division 1. This, combined with a factor of safety of four on the allowable stress intensity, is the rationale in Division 1 for no requirement of a detailed stress analysis of pressure vessels designed to this division.

Since a detailed stress analysis is not usually performed in the design of Division 1 pressure vessels, the true factor of safety of such vessels is never actually determined. The safety factor four applied in order to determine the allowable stress intensities does not consider any local stress increases or peak stresses that may exist at locations such as

nozzle-shell intersections. For example, if the stress near a nozzle shell intersection were twice as high as the far-field stress in a vessel, and since the factor of safety on the far-field stress is four, then the safety factor of the vessel based on stress would be two. However, since a detailed stress analysis of the vessel is not usually performed, the actual factor of safety on the vessel is not typically calculated or known.

The lack of a requirement for a detailed stress calculation in Division 1 is of particular importance when a vessel is to be designed for cyclic loading. In the case of cyclic service conditions, peak stresses developed at locations such as the nozzle-shell intersections strongly influence the number of loading cycles that the vessel can be expected to withstand. Thus, any pressure vessels that are expected to be subjected to cyclic loading conditions are required to be designed in accordance with Section VIII Division 2 of the ASME Code.

### **2.2.2 Design by Analysis**

Division 2 of Section VIII of the ASME Code provides a methodology for designing pressure vessels that are not governed by Division 1. This methodology is termed *design by analysis*. Specifically, all pressure vessels which are to be designed for cyclic service or make use of non-standard configurations are governed by Division 2.

Design by analysis requires that the stress at any given point be determined. Further, it requires that this be done using one of the following methods: numerical analysis, experimental stress analysis, or the stress index method. Analytical methods are

not mentioned in Division 2 at the present time because there does not as yet exist any analytical solutions for determining the stress distribution around nozzle-shell intersection regions.

Experimental analysis requires construction and testing of geometrically similar components to those which will be used in service. This is time consuming and expensive since it requires the fabrication of additional components and testing machines capable of simulating the design conditions. More importantly, experimental analysis does not easily or economically facilitate experimenting with changes in the geometry in order to improve a component's design.

The stress index method makes use of various formulas based on data gathered from experimental tests. This method is useful only if the opening to be considered is isolated from other openings. Further, the stress index method is not conservative when comparing experimental data for a small vessel diameter to nozzle thickness ratio,  $D/t$ , against larger  $D/t$  ratios [6]. This limitation means that large vessels, such as the burner vessels considered by this analysis, are not well suited to using the stress index method.

Numerical analysis using the finite element method can satisfy the requirement of Division 2 that the stresses at every point be checked against the appropriate allowable stresses. Further, this method facilitates experimenting with changes to the geometry in order to investigate improvements of components' design.

The curved geometry typical of pressure vessels, however, presents a difficult problem using the finite element method. This arises because of the high stress gradients that are developed near nozzle-shell intersections. It is desirable but difficult because of

the curved geometry to obtain a fine discretization scheme in these regions.

This thesis presents the use of the submodelling technique to overcome this difficulty. The use of this technique is detailed in Section 2.4.2, and the technique itself is detailed in Appendix A.

### **2.2.3 Hydrostatic Testing**

In both methodologies, design by analysis and design by rules, there is a final mandatory check of a pressure vessel that is performed to ensure that the design of the vessel is adequate for internal pressure. This test is termed the *hydrostatic test*, or frequently, the *hydrotest*. This test involves filling a vessel full of water and applying an internal pressure of 1.5 times the design pressure of the vessel. If no leaks develop during the hydrotest then the vessel is considered to have passed the hydrotest. If a leak develops, then the hydrotest is not passed.

## **2.3 PHYSICAL CONDITIONS**

### **2.3.1 Vessel Geometry**

The burner vessels are vertical pressure vessels of 652" [16 561 mm] inner diameter and 324" [8 230 mm] from the tangent of the top head and shell to the tangent of the bottom head and shell. The top head is semi-spherical, and the bottom head is 2:1

semi-ellipsoidal. The geometry and specifications used in this study were taken from the certified as built drawings for the burner vessel, Equipment Number 8-1C-2, which were plotted from Syncrude Canada Limited's on-line drawing library.

### **2.3.2 Attachment Geometry**

There were 14 nozzles and manways opening into each burner vessel. These openings are listed in Table 2-1. Nozzles with openings of 3" [76 mm] or less were not included in this table or this analysis, as the effects of such openings are very localized and are unlikely to produce significant stress intensities. That is, nozzles with nozzle-shell inside diameter ratios, or  $d_i/D_i$  ratios, of less than 0.005 were not included in the scope of this study.

The term  $d_i/D_i$  ratio and all subsequent terms are defined in the nomenclature section of this thesis.

### **2.3.3 Fabrication Material**

The burner vessels' heads, shells, and all manway and nozzle necks at the attachment juncture were fabricated from ASTM A-516 Grade 70 low alloy steel, except for the neck of nozzle N4 and the neck of nozzle N8, which were fabricated from A-106-B and A-403 Type 304 stainless steel, respectively. The material properties used for A-516-

70 were as follows:

Elastic Modulus	$E = 28.7 \times 10^6$ psi
Poisson's Ratio	$\nu = 0.3$
Yield Stress	$S_y = 38000$ psi
Tensile Strength	$S_u = 70000$ psi

Material properties for the A-106-B and A-403 Type 304 materials were not used, since these nozzles were not considered to be major openings and were therefore not included in this analysis; the consideration defining major openings is given in Section 2.4.3.

The corrosion allowance on the shell, heads, and nozzles was specified as 1/16" [1.6 mm]. Corrosion allowance was deducted from the appropriate thicknesses in this analysis.

## **2.4 FINITE ELEMENT MODEL**

### **2.4.1 FEA Software and Hardware**

All modelling and analyses were performed using the commercial program ANSYS version 5.0 running on the IBM RISC System/6000 hardware located in the University of Alberta's Mechanical Engineering Building. The ANSYS program was limited to a wavefront of 700 equations.

### **2.4.2 Submodelling Technique**

The finite element model of the burner vessel was developed using the submodelling technique. This technique is detailed in Appendix A of this thesis.

The curvature of typical of pressure vessel geometry has previously made it very difficult to practically develop an adequate mesh for a model of an entire vessel complete with its openings. The high mesh density near a nozzle-shell intersection meant that a complicated transition region from this high mesh density to a low far-field mesh density was needed in order to limit the time and resources required to solve the finite element problem to a practical level.

The use of the submodelling technique in this analysis reduced the need for complicated transition regions near the nozzle openings. By making use of this technique, this analysis has demonstrated that a finite element model of the entire burner vessel and all of its major openings can be practically solved using the current standard RISC System/6000 workstation technology. Further, it facilitates future experimentation with different designs in regions of interest, such as different fillet radii, and nozzle external loadings from the attachments.

### **2.4.3 Major Openings**

Eight nozzles and manways were identified as being the major openings into the burner vessel. The criterion for consideration as a major opening was a diameter ratio,

$d_i/D_i$ , of greater than 0.01. As described in Table 2-2, the four manways mark numbers M2 through M5 were of a low  $d_i/D_i$  ratio. Further, since these four manways were remote from other openings and not likely to be subjected to significant external loads, it was considered unlikely that a highly refined analysis of them would be required. The eight nozzles which were thus selected as major openings are shown in bold letters in Table 2-2 and are the following: mark numbers N7, S1, S2, S3, S5, S6, S10, and M1.

Although the present finite element model only includes the eight major openings, the model is generated in such a way that all of the nozzle and manway openings of greater than 3" [76 mm] diameter could be easily included should a future need arise. This was accomplished by including all of the nozzles and manways of greater than 3" [76 mm] diameter in the ANSYS global and submodel solid models. These ANSYS solid models are the representations of the physical geometry within the software from which the actual finite element models (nodes and elements) are generated.

#### **2.4.4 Global Model**

The use of the Submodelling technique required that the analysis of the burner vessel be performed in two steps. The first step was a global analysis in order to obtain results away from the nozzle-shell intersections. The second step was to apply the submodelling technique using the results from the global analysis in order to obtain results near the nozzle-shell intersections.

The global analysis involved developing a *global model* of the burner vessel



complete with all of the major openings. This part of the analysis made use of a mesh which produced adequate results away from the nozzle-shell intersections, but which was too coarse to produce satisfactory results in the local regions near the nozzle openings.

The solid modelling technique was used to generate the finite element model. That is, a solid model representing the vertices, edges, and faces of the physical geometry with keypoints, lines, and areas, respectively, was first created and then automatically meshed to generate the nodes and elements which compose the finite element model.

The solid model of the burner vessel consisted of 618 areas, 1354 lines, and 773 keypoints. A plot showing the lines of the burner vessel solid model is shown in Figure 2-1. Appropriate meshing controls were prescribed to the solid model to ensure that all elements were quadrilateral and, as close as was practical, of an aspect ratio of 1:1. The model was constructed using 2555, 8 node ANSYS Shell93 isoparametric shell elements [7]. A plot showing the element discretization of the global model is shown in Figure 2-2.

As stated earlier, in order to facilitate the possible future need to analyse one of the nozzles that was not considered to be one of the eight major openings, the global solid model included, in addition to these eight, all of the nozzle and manway openings of greater than 3" (76 mm) diameter. Hence, the developed model could easily facilitate an analysis of one of the smaller nozzles should such a future need arise.

#### **2.4.5 Submodels**

The second step in the analysis of the burner vessel was the analysis of an

independent, more finely meshed model, or submodel, of each nozzle-shell intersection region. The displacement results obtained after performing a finite element analysis of the global model of the first step were prescribed as displacements along the boundary of the more finely meshed submodels.

The discretization of the global model into lines and areas was done in such a way that the submodels of the nozzle-shell intersection regions could easily be obtained by selecting the appropriate areas, lines, and keypoints from the global model. Figure 2-3 shows an example of an element plot of one of the submodels, Submodel N7.

This is a new application of the submodelling technique that made an analysis of the burner vessel with all of its major openings possible. This type of analysis could not have been practically accomplished without using this technique. The submodelling technique is described in detail in Appendix A of this thesis.

## **2.5 INTERNAL PRESSURE CONDITIONS**

### **2.5.1 Simulated Loading**

A stress/strain analysis of the finite element model subjected to the pure internal pressure was performed. The magnitudes of internal pressure simulated on each component were in accordance with the design conditions detailed on the as-built fabrication drawing 8-1C-2 number 1 revision 8. These design conditions have been summarized in Table 2-3. A plot of the global model nodes showing this simulated

internal pressure loading is shown in Figure 2-4.

### **2.5.2 Boundary Conditions**

The burner vessels are vertical, skirt supported pressure vessels. The skirt support consists of a cylindrical shell welded to each burner vessel near the tangent line of the bottom head of the vessel cylindrical shell (bottom tangent line). In order to simulate this type of support, kinematic boundary conditions were prescribed to all nodes located on the locus of the bottom tangent line. The nodes to which these boundary conditions were prescribed were constrained from any displacement along the axial direction of the burner vessel. A plot of the global model nodes showing location of these prescribed constraints is shown in Figure 2-5. In this figure, the prescribed constraints are depicted using a small blue triangle and constrain displacement in the z-direction as defined in the figure.

The ANSYS program used to create the burner vessel finite element model had a wavefront limitation of 700. With only the above constraints prescribed, the solution wavefront was found to be 1366. To enable the internal pressure simulation to continue, a further assumption was necessary. Specifically, that subjected to pure internal pressure, the bending forces that are developed near an opening are of significance only in regions near that opening. Thus, in accordance with this assumption, the rotational degrees of freedom were constrained for each node, suppressing the bending of the shell elements of the global model. Therefore, membrane forces only were considered in the global model. This was considered adequate since the submodels, which consider combined membrane

and bending forces acting in the shell near openings, demonstrate that the bending forces attenuate rapidly with the distance from the opening. This attenuation is evident in Figure 2-8k.

Once the solution for the global model was obtained, kinematic boundary conditions were then prescribed to the individual submodels using the cut-boundary displacement method. That is, the appropriate nodal degree of freedom value from the results of the global analysis was prescribed as a boundary condition for each node along the cut boundary of the submodel. This method is described in detail in the Appendix A of this thesis.

## **2.6 RESULTS FROM THE INTERNAL PRESSURE SIMULATION**

### **2.6.1 Global Model Results**

The purpose of the finite element analysis of the global model was to provide the stress, strain, and displacement fields in regions remote from the discontinuities and openings. Further, the global analysis was to provide an indication of how rapidly the local stresses associated with discontinuities and openings diminished with distance, or the attenuation length of the local stresses.

Figure 2-6 shows a plot of the circumferential stress in pounds per square inch developed in the hemi-spherical top head of the global model near the region of the radial cylindrical nozzle mark number S6. The circumferential stress away from the nozzle-shell

intersection shown in this figure can be compared to the results predicted by the theory of shells of revolution. This comparison is detailed explicitly in Figure 2-7 and is discussed in the following paragraph.

The variation in the normal and tangential stress components along a longitudinal cut through the nozzle and shell with distance from the nozzle-shell juncture are plotted in Figure 2-7. The stress components have been non-dimensionalized by the allowable stress intensity of 23,333 psi for SA-516-70 steel [8], and the distance from the juncture was taken as positive along the vessel meridian and was non-dimensionalized by the inside diameter of the nozzle opening. The tangential and normal stress components predicted by shell theory for the spherical shell are also plotted in Figure 2-7 for easy comparison to the stresses predicted by the global model. This figure demonstrates the strong agreement between the finite element results and the shell theory. Details on the theory of shells of revolution can be found in several texts [5, 9, 10].

The circumferential stress component,  $\sigma_H$ , and the longitudinal stress component,  $\sigma_L$ , for a closed thin walled spherical shell and a closed thin walled cylindrical shell were calculated using the following equations:

$$\text{Spherical shell:} \quad \sigma_H = \sigma_L = pD_m/2T \quad (2.1)$$

$$\text{Cylindrical shell:} \quad \begin{aligned} \sigma_H &= pD_m/4t \\ \sigma_L &= pD_m/2T \quad (\text{closed}) \end{aligned} \quad (2.2)$$

where:

$$\begin{aligned} p &= \text{internal pressure} \\ D_m &= \text{shell mean diameter} \\ T &= \text{shell thickness} \end{aligned}$$

and compared to the numerical results from Figure 2-7 for a  $u/d$  ratio of  $\pm 1$ , respectively. For the spherical shell, the numerically calculated stress components differed from those calculated using Equation 2.1 by 5% in the circumferential direction and 5% in the longitudinal direction. Note since there were no longitudinal piping loads applied to the finite element models, the theoretical longitudinal stress for a spherical shell was reduced to account for nozzle S6, an opening of 96" [2438 mm] diameter. The theoretical far-field stresses for a spherical shell have been superimposed on the finite element results plotted in Figure 2-7 for the sake of comparison. For the open cylindrical nozzle the difference was 5% in the circumferential direction and 1% in the longitudinal direction. A similar comparison of the far-field stress for the cylindrical section of the global model near nozzle S5 was done using Equation 2.2. The results of this comparison are listed in Table 2-4. Since the dominant stress component in determining proximity to yielding is the circumferential component, the solution for the far-field stress using the global model is considered adequate. Note that the burner vessel geometry is such that the longitudinal stress,  $\sigma_L$ , would vary along the cylindrical axis, from fully closed towards a less constrained condition, and also that the internal pressure varies along the cylindrical axis as indicated in Table 2-3.

### **2.6.2 Submodel Results**

The cut-boundary displacement method was used to prescribe the boundary conditions of the submodels. In constraining the rotational degrees of freedom of the

global model, it was assumed that the deflection under pure internal pressure would occur by dilation only. This assumption is reasonable for areas remote from discontinuities. This assumption is acceptable for the global model, since the global model is to provide results for regions away from the discontinuities. However, this assumption cannot be made for the submodels since they include regions of discontinuity, such as nozzle openings, where local bending stresses would occur. Hence, the rotational degrees of freedom of the submodels were left unconstrained.

The internal pressure loading prescribed to the submodels was in accordance with the design pressure of the burner vessel, as described in Table 2-3. Similar to the global model, no external loads, such as radial thrust, shearing loads or moments, were applied to the nozzle ends in the submodels.

Figure 2-8a to 2-8n shows the circumferential and longitudinal stresses developed in each submodel (N7, S1, S2, S3, S5, S6, and S10) under the internal pressure. These plots indicate that the maximum stress occurs on the shell side of the nozzle-shell juncture for configurations with no reinforcement pad, such as in the case of Submodel S6. However, when a reinforcement pad configuration was used, the location of the maximum stress could be found at the outside edge of the reinforcement pad on the shell-side of the juncture, such as in the case of Submodels S2 and S3.

The deflected shapes of a circumferential and a longitudinal cut through the nozzle-shell juncture for each submodel are shown in Figure 2-9a to 2-9l for Submodels N7, S1, S2, S3, S5, S6, and S10. These plots suggest that the stiffening of the shell at the intersection of a cylindrical nozzle prevents the shell from deforming in a membrane

dominated manner near the junction. Thus, relatively high local stresses in the vicinity of the nozzle openings result from the bending of the shell required for the deformation compatibility with the higher stiffness of the nozzle-shell juncture. Similar behaviour is observed if a reinforcement pad is used. In the latter case, the location of the maximum stress is at the edge of the pad. For example, in the case of Submodel S5, a reinforcement pad was included. It is seen from Figures 2-9i and 2-9j that the bending of the shell under internal pressure results in a local maximum located at the outside edge of the reinforcement pad. The circumferential and longitudinal stress distributions corresponding to Figures 2-9i and 2-9j are shown in Figures 2-8i and 2-8j. The edge of the reinforcement pad in the stress contour plots is two elements away along the shell from the nozzle/shell juncture.

### **2.6.3 Convergence of Stress**

The convergence of the burner vessel model was tested by comparing the maximum circumferential stress in the vicinity of nozzle S6 as predicted by two different solutions. The first was the solution of Submodel S6, which made use of 960 elements. The second was a solution obtained by re-meshing the solid model of Submodel S6 using 2340 elements.

The stress predicted by the two models did not significantly vary. This suggests that the solution has converged for the mesh density used in Submodel S6, since more than doubling this number of elements produces no significant change in the magnitude of the



predicted stress.

#### **2.6.4 Comparison to Physical Experiments**

In order to further test the accuracy of the developed model, the finite element results for Submodel S6 from the internal pressure simulation, were compared to the results of physical experiments found in the literature. Note that no exactly matching geometry was available; hence, the trends for similar geometries will be discussed.

Figure 2-10 illustrates the trend of the normal and tangential stress components at the mid-surface for a cylindrical nozzle intersecting a spherical shell reported in a photoelastic experimental study [11]. These stresses are reported in the literature for the outside and inside surfaces of the shells. The mid-surface values of these components were calculated assuming a linear stress distribution between the inside and outside surfaces. The mid-surface values are plotted in order to facilitate easy comparison to the finite element results obtained.

The experimental geometry and the geometry of nozzle S6 are detailed in Table 2-5 for comparison. The material used in the experiments was Araldite 6020, an epoxy resin. The fringe patterns were calibrated by comparing regions remote from discontinuities to stresses computed by shell theory. The maximum peak stress reported by the experimentalists was 2 times the magnitude of the far-field stress developed in the spherical shell.

Figure 2-11 is a plot of the finite element results for the variation of the normal

and tangential components of stress at the mid-surface along a longitudinal cut through Submodel S6. The maximum peak stress to allowable stress ratio and far-field stress to allowable stress ratio calculated for nozzle S6 is 0.6 and 0.45, respectively. The maximum calculated peak stress is then  $(0.60 \div 0.45) = 1.3$  times higher than the far-field stress. Thus, the peak stress intensification determined using finite element analysis is 50% lower than the peak stress intensification of 2.0 reported in the experimental study. With the exception of the magnitude of the peak stress intensification, the trend of the stress variation from the finite element results compares well to that of the physical study.

The convergence of the finite element predicted far-field stresses for submodel S6 to the theoretical stresses for a spherical shell [9] are superimposed on the finite element results for submodel S6 in Figure 2-11. The theoretical far-field tangential stress is less than the theoretical far-field normal stress to account for the open area of the nozzle. This was necessary because no longitudinal piping loads were applied to the finite element models. Thus, this figure demonstrates that the finite element predictions for submodel S6 converge to the stresses calculated using shell theory.

### **2.6.5 Evaluating Finite Element Results**

The model of the burner vessel developed and presented herein can be used to solve many practical problems that may arise in the future. Generally, the allowable stresses used to compare against finite element results must consider a more complete scope than that considered in the analysis presented in this thesis. Weld quality, heat treatment,

material properties and shot peening are examples of what must be considered by designers when establishing allowable stresses for comparison to the finite element results.

The Fe/Pipe program is a finite element program that is specific to pressure vessels and pressure piping. This software uses the approach of increasing by default the reported stress intensity at nozzle-shell intersection by 35% to 50% of the stress intensity calculated by the finite element analysis. This is done based on the experience of the authors of the Fe/Pipe program in an attempt to account for uncertainties at such regions [12]. The comparison presented in Section 2.6.4 of this thesis comparing the burner vessel finite element results against experimental results from the literature would support such an increase.

In all cases, it is the responsibility of the pressure vessel designer to interpret finite element analysis results as predictive only and with consideration to the assumptions made in performing the analysis.

Although an effort has been made in this analysis to verify the results as much as possible, there is at present no measured experimental data on pressure vessels of the scale of the burner vessels with which to base a complete verification. Therefore, the results presented herein should be used with caution and by persons qualified in the methods and interpretation of finite element techniques and results.

The burner vessel analysis identifies a need for a set of finite element results for intersecting shells complete with experimental measurements for matching geometries. Comparisons of the finite element results and the physical measurements would be valuable in order to obtain further information regarding the accuracy of the finite element

method applied to intersecting shell problems.

## **2.7 DISCUSSION AND SUMMARY OF RESULTS**

The finite element analysis of the burner vessel using the model developed in this project produced a significant amount of information. The elastic stress/strain response of the vessel subjected to an internal pressure was obtained. Moreover, the deflected shape of the vessel wall near the nozzle openings was plotted. This deformed geometry would have been difficult or impossible to obtain by analytical methods.

The deflected shape and stress component plots provided insight into the consequences of reinforcing nozzle openings using heavy reinforcement pads instead of heavier nozzle walls. These consequences were shown to include relatively high stress levels and bending deformation in the vessel shell at the outside edge of the reinforcing pad.

The rationale put forward for heavy reinforcing pads is that in the case of failure it would be more desirable that the failure occurs in the nozzle neck portion of the opening than in the vessel shell. Thus, it would seem intuitively reasonable that increasing the thickness of the vessel shell near the opening by means of a reinforcing pad would have the effect of shifting the failure location from the shell to the nozzle neck.

However, in some cases, such as at opening S5, the use of a reinforcing pad has resulted in high stress levels throughout the portion of the shell covered by the reinforcing pad. This effect is evident in the stress contour plots for opening S5, Figures 2-8i and 2-

8j. For this configuration subjected to internal pressure, the use of a reinforcement pad effectively increased the chance for a failure in the vessel shell away from the nozzle/shell juncture towards the edge of the reinforcement pad because of the local bending stresses in the shell at the edge of the pad. Thus, the results of this analysis suggest that in order to minimize the region of high local stress intensity near an opening subjected to internal pressure it is desirable for the reinforcement material to be located within the nozzle neck and to not use local reinforcement pads welded to the vessel shell.

The convergence of stress for one of the submodels was performed which demonstrated that the mesh density used for the submodel was adequate. Finally, the trend of the stress variation along a cut through a nozzle-shell intersection was found to be in good agreement with results of a photoelastic study from the literature.

## **2.8 CONCLUSIONS**

An analysis tool was developed for the two coker burner vessels located at Syncrude Canada Limited's Mildred Lake Upgrading Plant was developed. These vessels are of an enormous scale, and each is pierced by several openings. The nature and complexity of the vessel geometry does not lend itself to either an analytical solution or the stress index method, and a single finite element model of the entire vessel is not currently practical because of the nature of the geometry.

The analysis tool reported here used the cut boundary displacement method to develop a finite element model and the appropriate submodels required to analyse the

entire burner vessels complete with all of their major openings. This analysis tool was used to predict the stress/strain response of the burner vessels subjected to internal pressure, and the results of this analysis were discussed.

The results of the finite element analysis performed leads to the following conclusions:

- I. The finite element model of the burner vessel 8-1C-2 was shown to predict the elastic stress/strain and displacement fields developed under a prescribed internal pressure.
- II. The results from this analysis were used to gain an insight into the behaviour of the vessel shell in the vicinity of an opening or attachment.
- III. The results from this analysis were used to demonstrate the convergence of far-field stress for an internal pressure simulation.
- IV. The peak stresses compared against the far-field stresses determined using the finite element results for the internal pressure simulation were found to be 50% less than a the peak stresses compared to the far-field stress reported from physical experiments.

**Table 2-1**

## Description of Nozzles and Manways

Mark No.	Size	Description
S1	53" I.D.	cold coke riser
S2	44" I.D.	hot coke riser
S3	14"	scouring coke standpipe
S5	53" I.D.	elutriator overhead return
S6	96" I.D.	flue gas outlet
S10	62" I.D.	primary air inlet
N4	10"	elutriator feed standpipe
N7	14"	coke addition inlet
N8	6"	coke withdrawal outlet
M1	112" I.D.	manway
M2	34" I.D.	manway
M3	34" I.D.	manway
M4	32" I.D.	manway
M5	24" I.D.	manway

**Table 2-2**

Details of Nozzles and Manways (un corroded condition)

Mark no.	D <sub>i</sub> (in.)	T (in.)	D <sub>i</sub> /T	d <sub>i</sub> (in.)	t (in.)	d <sub>i</sub> /t	d <sub>i</sub> /D <sub>i</sub>	t/T	s/S
S1	1174	2.3125	508	53	2	26.5	0.0451	0.865	0.104
S2	1174	2.0625	569	44	2	22.0	0.0375	0.970	0.077
S3	1174	2.5	470	14	0.5	28.0	0.0119	0.200	0.119
S5	652	2.375	275	53	0.5	106	0.0813	0.211	0.385
S6	652	0.75	869	96	1.875	51.2	0.1472	2.50	0.118
S10	1174	2	587	62	2	31.0	0.0528	1.00	0.106
N4	1174	3.3125	354	10	0.5	20.0	0.00852	0.151	0.113
N7	652	2	326	14	0.5	28.0	0.0214	.250	0.086
N8	1174	2	587	6	0.5	12.0	0.00511	.250	0.041
M1	652	2.375	275	112	2.5	44.8	0.1718	1.05	0.164
M2	652	0.75	869	34	1.3125	25.9	0.0521	1.75	0.060
M3	652	0.75	869	34	1.3125	25.9	0.0521	1.75	0.060
M4	652	0.75	869	32	1.3125	24.4	0.0491	1.75	0.056
M5	1140	1.25	912	24	(STUB)	-	0.0211	-	-



**Table 2-3**

## Design Temperatures and Pressures

Location	Temperature (°F)	Pressure
bottom head	650 max. -20 min.	54 psig
shell	600 max. -20 min.	48 psig at top T.L. and increase uniformly to 54 psig at bottom T.L.
top head	600 max. -20 min.	48 psig

**Table 2-4**

## Summary of Far-Field Comparison

	Cylindrical Shell	Spherical Shell
% Difference in $\sigma_H$	3	5
% Difference in $\sigma_L$	15	5

**Table 2-5**

## Details of Nozzle S6 and a Nozzle from the Literature

Mark no.	$D_i$ (in.)	T (in.)	$D_i/T$	$d_i$ (in.)	t (in.)	$d_i/t$	$d_i/D_i$	$t/T$	s/S
S6	652	0.75	869	96	1.875	51.2	0.147	2.50	0.118
Experiments [7]	14.3	0.585	24.2	1.845	0.158	11.7	0.129	0.270	0.994

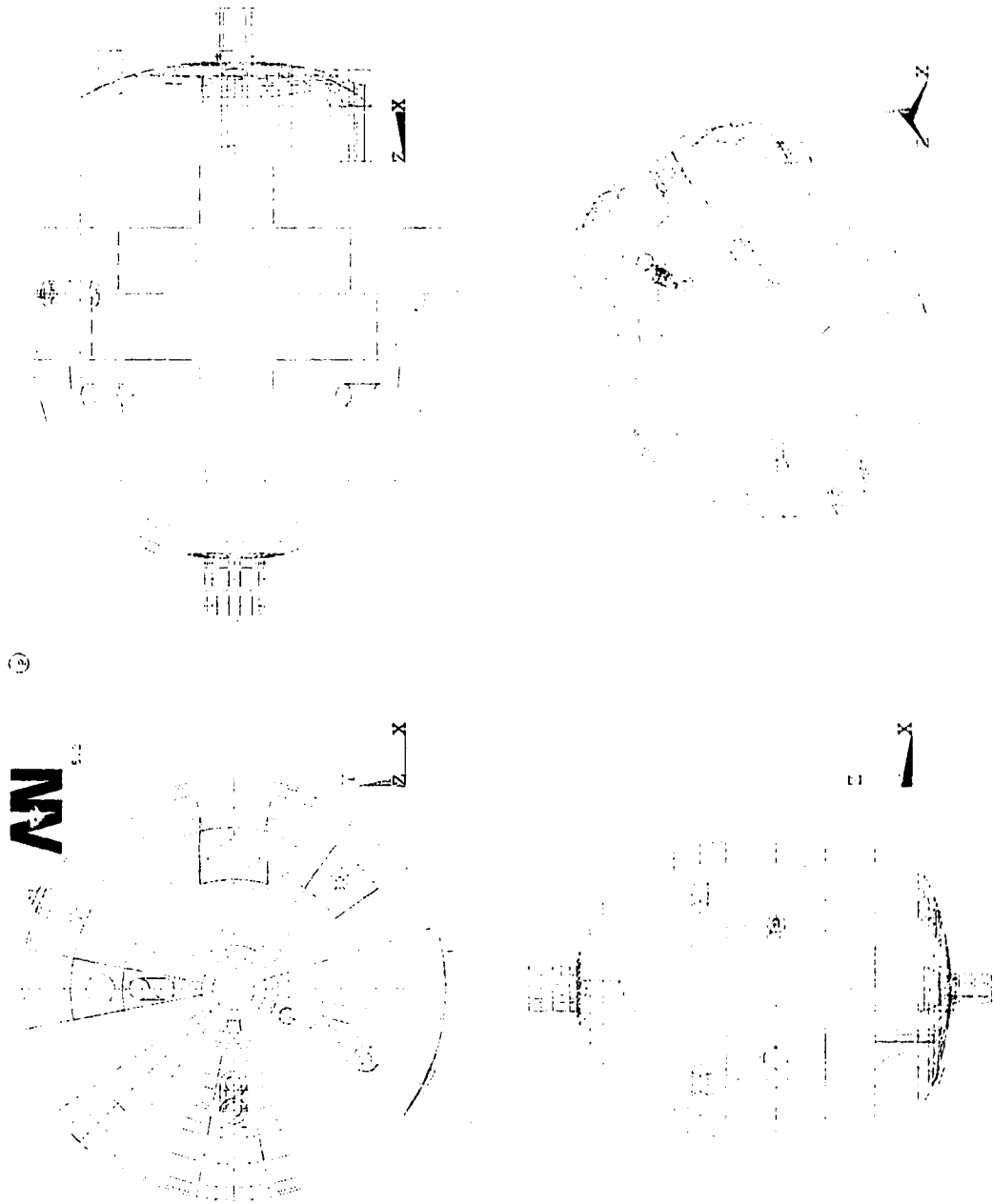


Figure 2-1 A plot of the lines of the global model.

JUN 29 1995  
19:59:07  
PLOT NO. 3  
ELEMENTS  
TYPE NUM

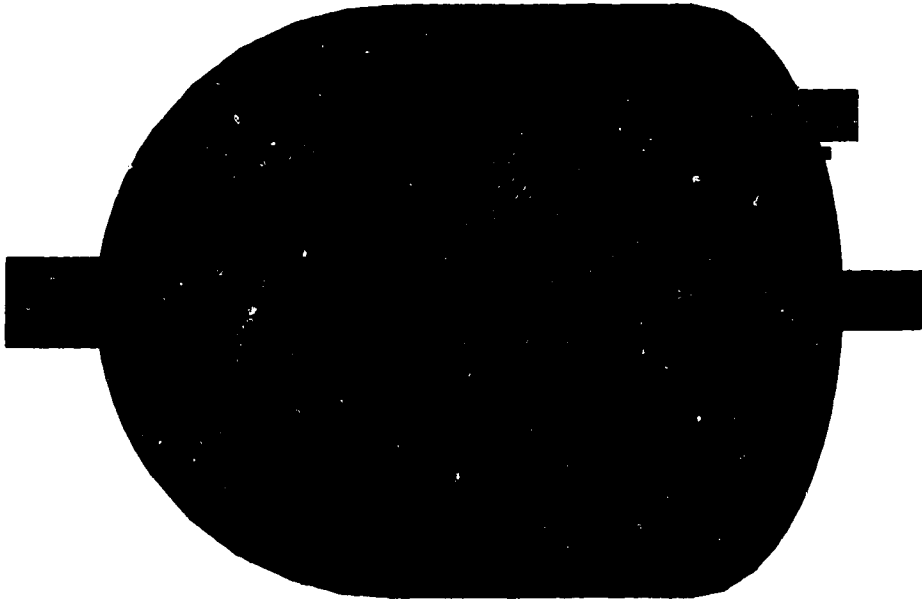


Figure 2-2 A plot of the element discretization of the global model.

JUN 29 1995  
20:00:35  
PLOT NO. 7  
ELEMENTS  
TYPE NUM



x

Figure 2-3 A plot of the element discretization of Submodel N7.

JUN 29 1995  
19:59:22  
PLOT NO. 4  
NODES  
TYPE NUM

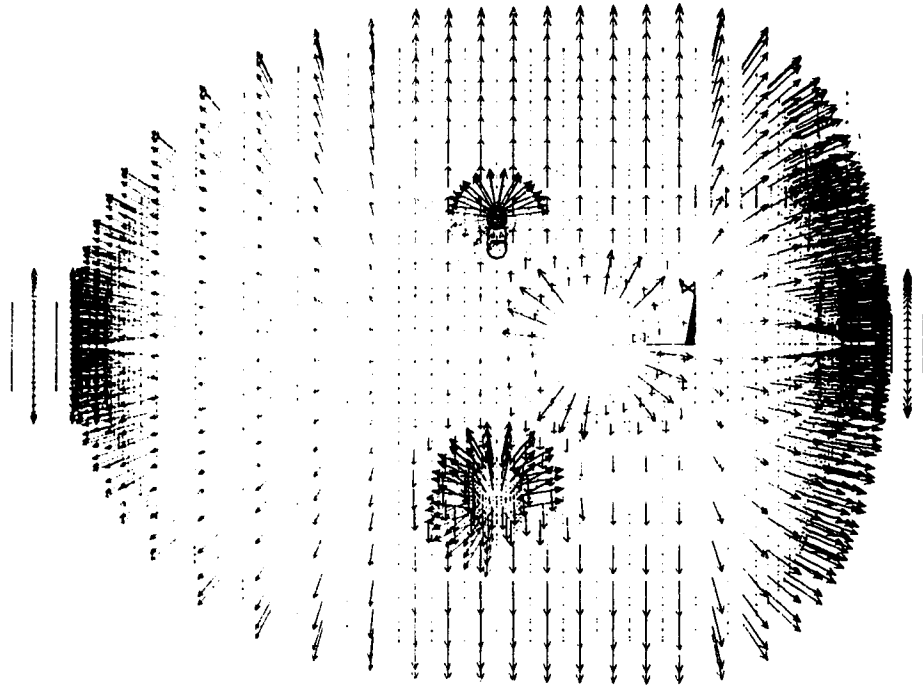


Figure 2-4 A plot of the global model nodes showing the internal pressure loading.

JUN 29 1995  
19:59:35  
PLOT NO. 5  
NODES  
TYPE NUM

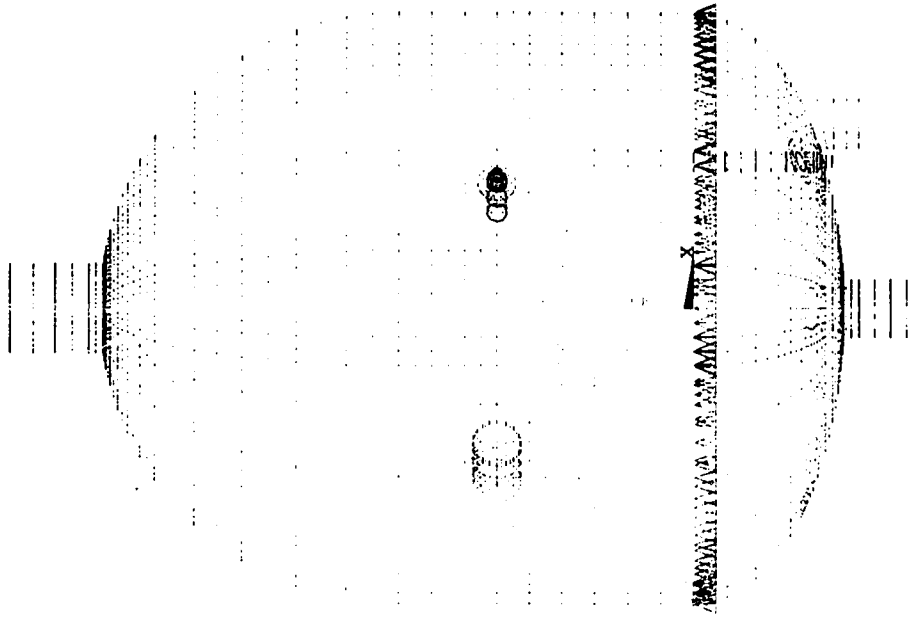


Figure 2-5 A plot of global model nodes showing the prescribed boundary conditions.

JUN 29 1995  
 20:00:12  
 PLOT NO. 6  
 1113  
 2174  
 3235  
 4296  
 5358  
 6419  
 7480  
 8541  
 9603  
 10664  
 (psi)

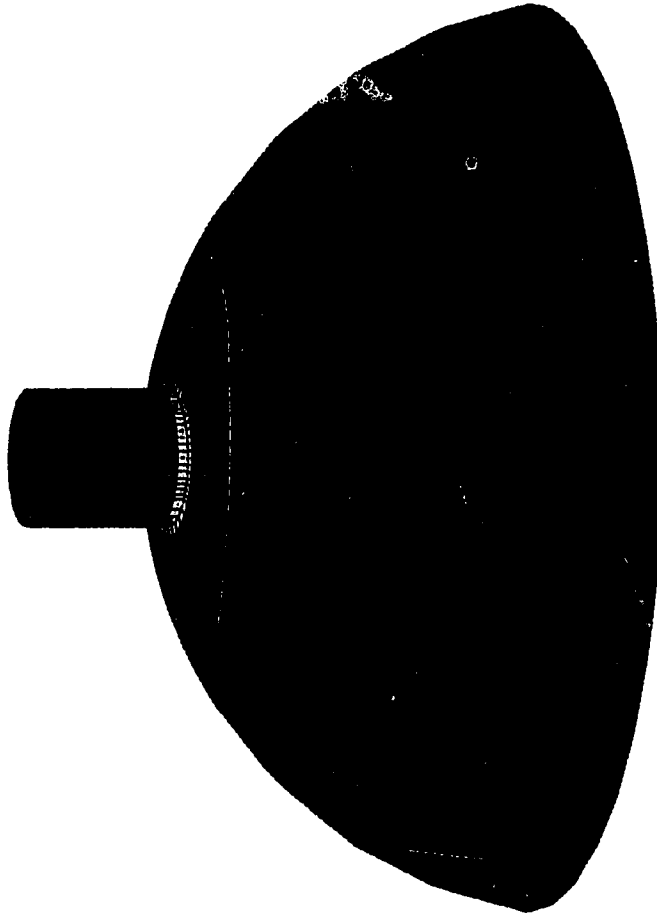


Figure 2-6 A plot of the numerically predicted circumferential stress developed in the top head near nozzle S6 under pure internal pressure loading.

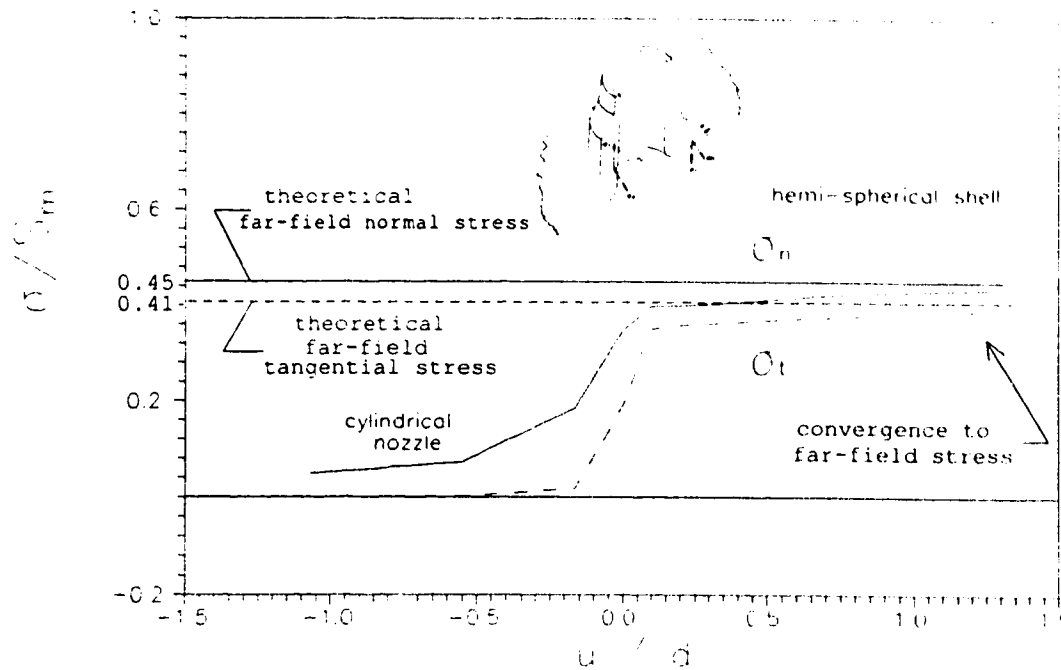


Figure 2-7 Variation in the circumferential and longitudinal stress components along a longitudinal cut through nozzle S6 with the distance from the nozzle-shell juncture, non-dimensionalized through dividing by the nozzle diameter. The far-field stress from shell theory [9] is superimposed on this plot.



JUN 29 1995  
20:00:45  
PLOT NO. 8  
-5828  
-2463  
903.228  
4269  
7635  
11000  
14366  
17732  
21098  
24463  
(psi)

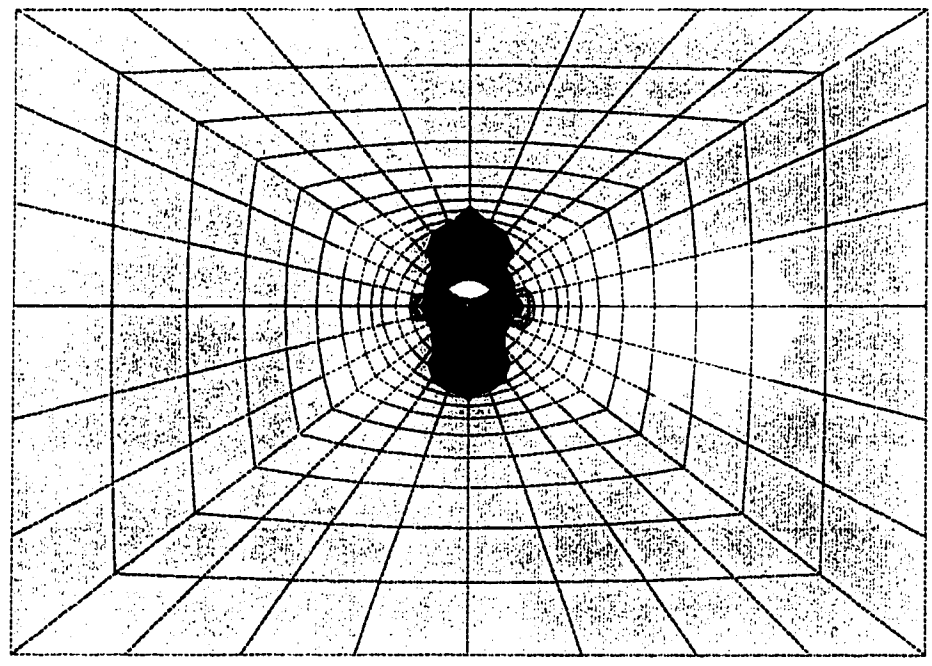


Figure 2-8a Submodel N7 - Circumferential Stress

JUN 29 1995  
 20:00:51  
 PLOT NO. 9  
 -2092  
 -870.017  
 352.319  
 1575  
 2797  
 4019  
 5242  
 6464  
 7686  
 8909  
 (psi)

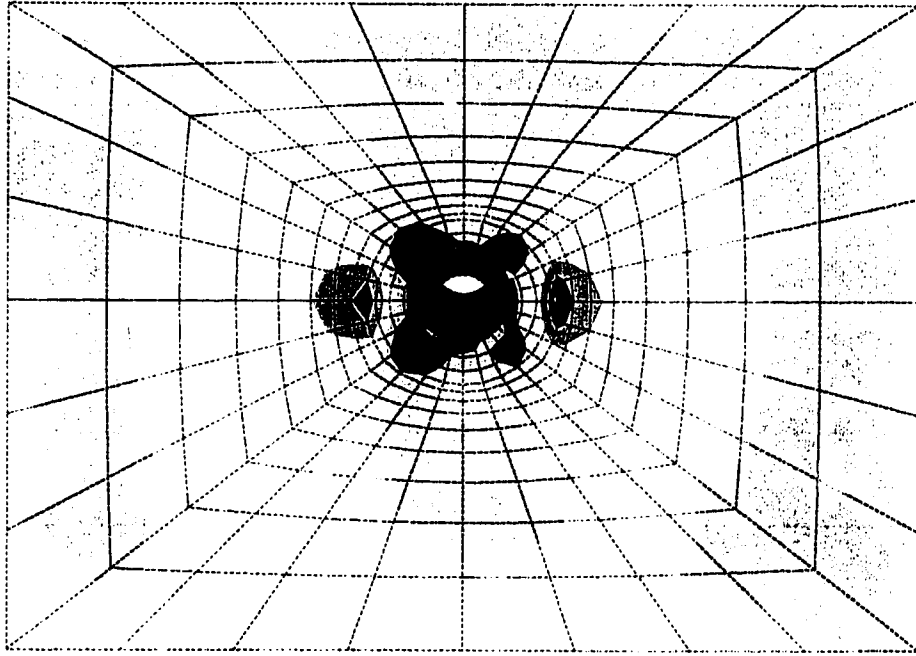


Figure 2-8b Submodel N7 - Longitudinal Stress

JUN 29 1995  
 20:01:58  
 PLOT NO. 10  
 -4585  
 -2352  
 -119.124  
 2114  
 4346  
 6579  
 8812  
 11045  
 13278  
 15510  
 (psi)

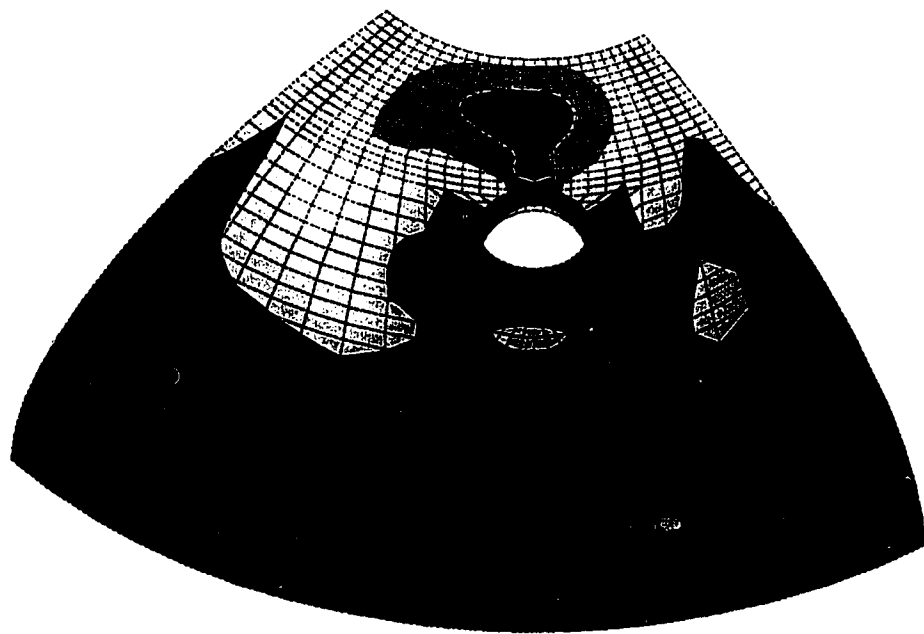


Figure 2-8c Submodel S1 - Circumferential Stress

29 1995  
 2:11  
 PLOT NO. 11  
 -3887  
 -1962  
 -37.051  
 1888  
 3813  
 5737  
 7662  
 9587  
 11512  
 13437  
 (psi)

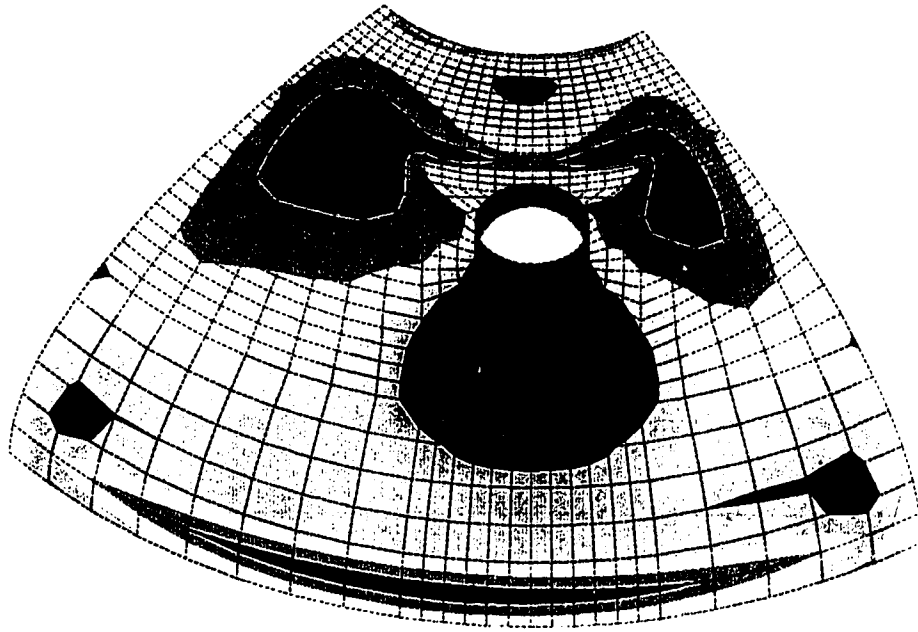


Figure 2-8d Submodel S1 - Longitudinal Stress

JUN 29 1995  
 20:02:46  
 PLOT NO. 12  
 -2390  
 -644.574  
 1101  
 2847  
 4593  
 6338  
 8084  
 9830  
 11575  
 13321  
 (psi)

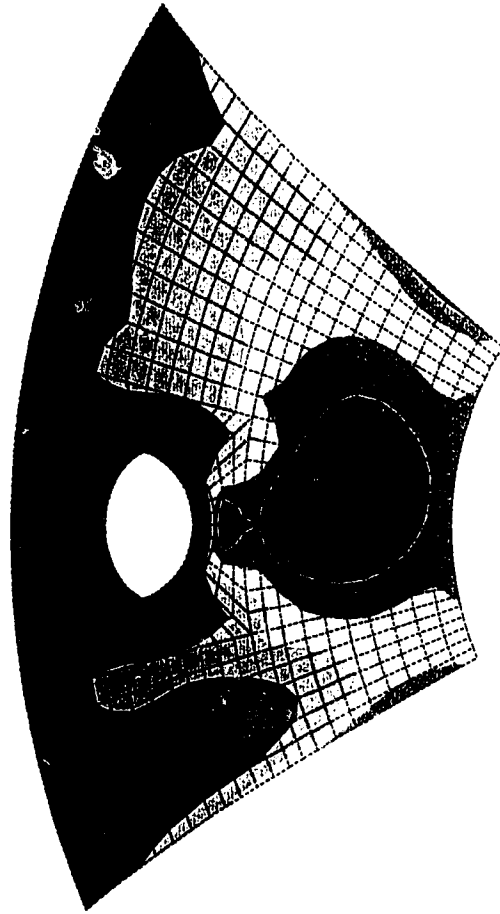


Figure 2-8e Submodel S2 - Circumferential Stress

JUN 29 1995  
 20:02:55  
 PLOT NO. 13  
 -2920  
 -1114  
 691.2  
 2497  
 4302  
 6107  
 7913  
 9718  
 11524  
 13329  
 (psi)

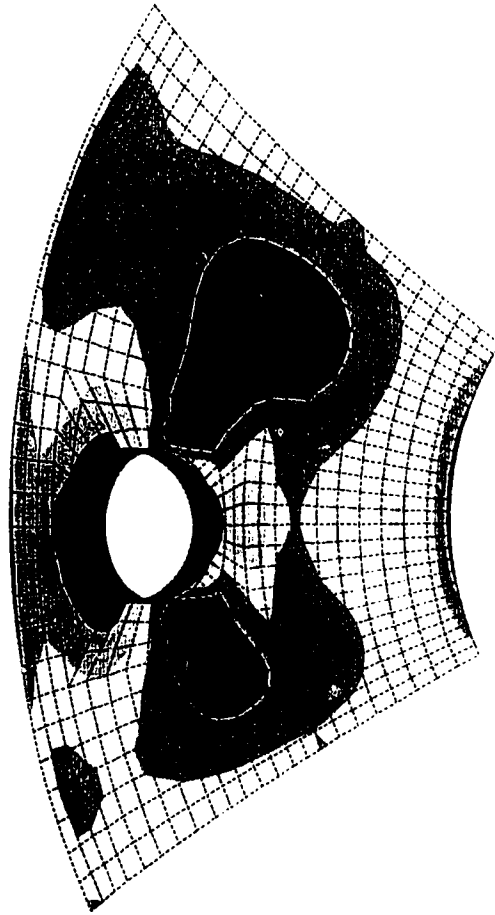


Figure 2-5f - Submodel S2 - Longitudinal Stress

JUN 29 1995  
20:03:33  
PLOT NO. 14  
-2917  
-1417  
819  
1561  
3081  
4580  
6079  
7579  
9078  
10578  
(psi)

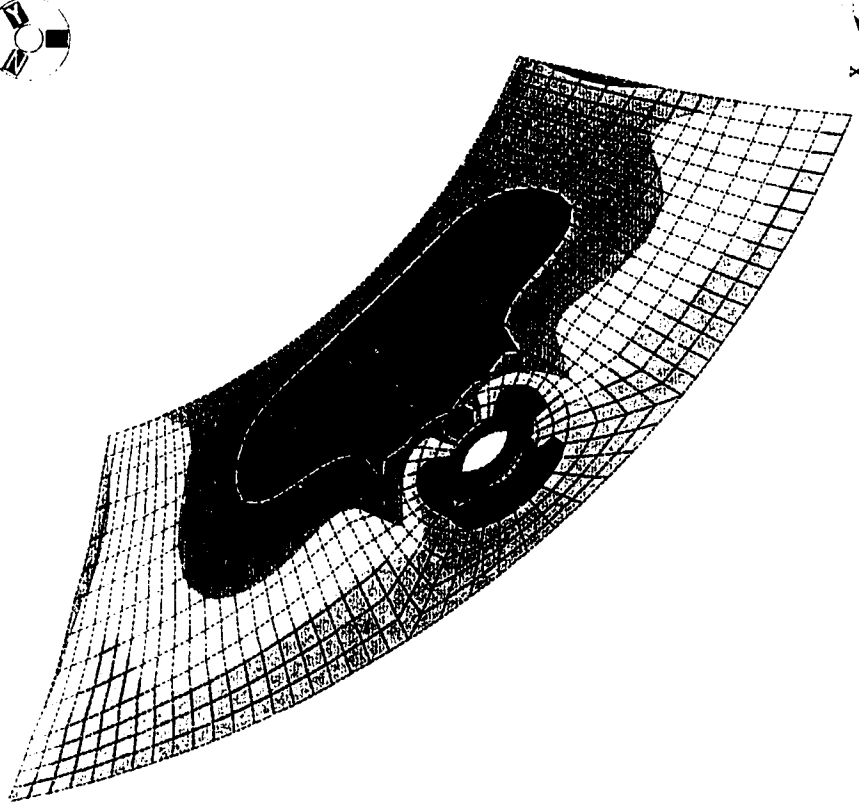


Figure 2-8g Submodel S3 - Circumferential Stress

JUN 29 1995  
20:03:45  
PLOT NO. 15  
-2301  
-676.131  
948.879  
2574  
4199  
5824  
7449  
9074  
10699  
12324  
(psi)

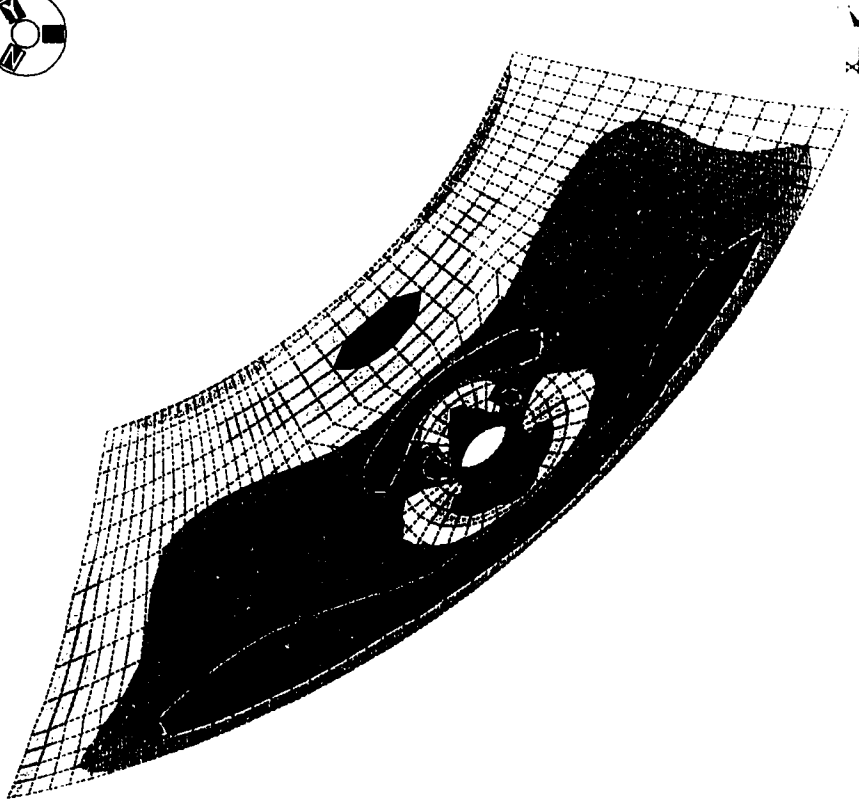


Figure 2-8b) Submodel S3 - Longitudinal Stress



JUN 29 1995  
 20:04:26  
 PLOT NO. 16  
 -7603  
 -4297  
 -992.038  
 2313  
 5619  
 8924  
 12229  
 15535  
 18840  
 22146  
 (psi)

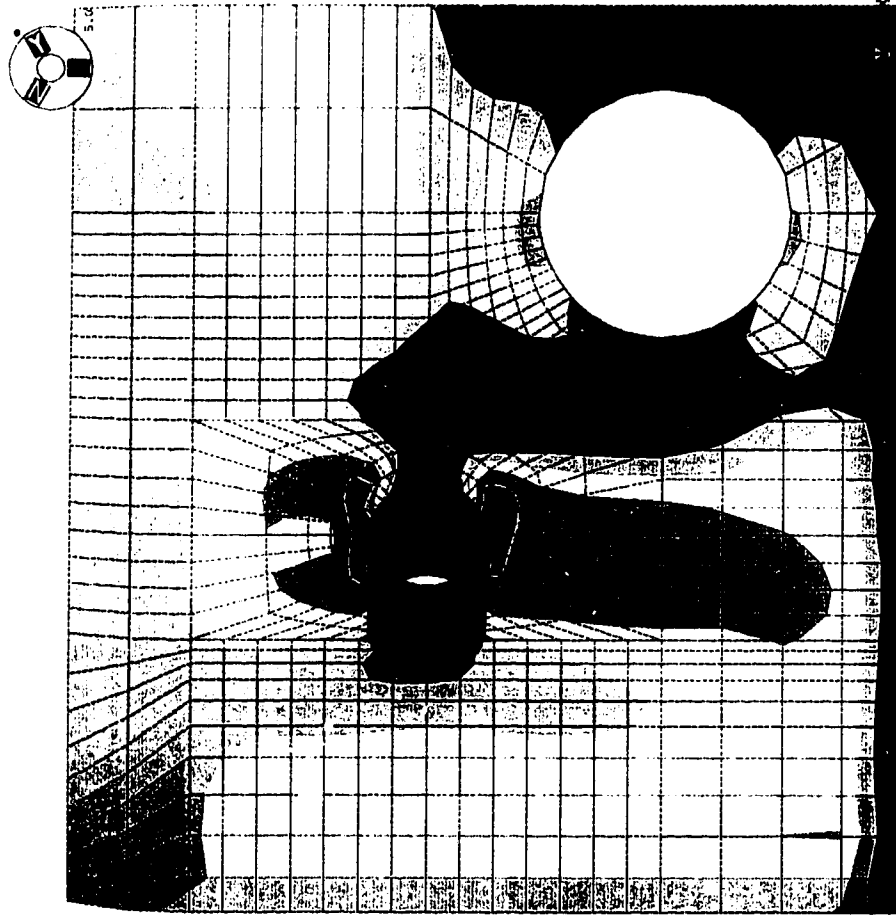


Figure 2-8i Submodel S5 - Circumferential Stress

JUN 29 1995  
 20:04:38  
 PLOT NO. 17  
 -4107  
 -2425  
 -741.73  
 941.093  
 2624  
 4307  
 5990  
 7672  
 9355  
 11038  
 (psi)

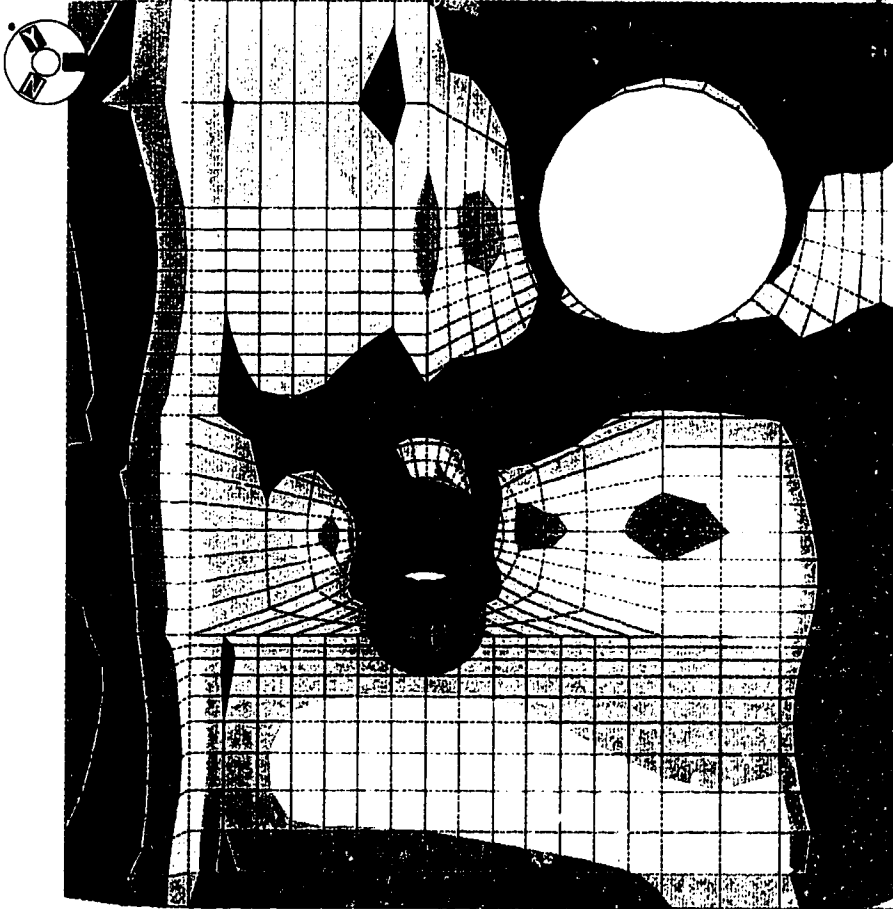


Figure 2-Sj Submodel S5 - Longitudinal Stress

JUN 29 1995  
 20:05:21  
 PLOT NO. 18  
 486.049  
 2049  
 3612  
 5175  
 6738  
 8301  
 9864  
 11427  
 12990  
 14553  
 (psi)

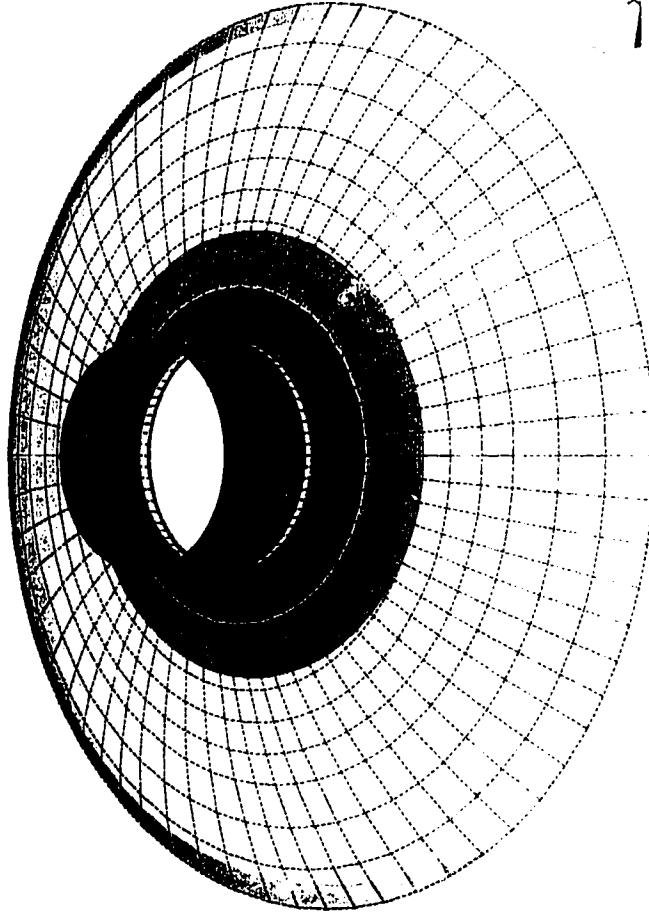


Figure 2-8k Submodel S6 - Circumferential Stress

JUN 29 1995  
20:05:32  
PLOT NO. 19  
-6.861  
1005  
2016  
3027  
4039  
5050  
6062  
7073  
8085  
9096

(psi)

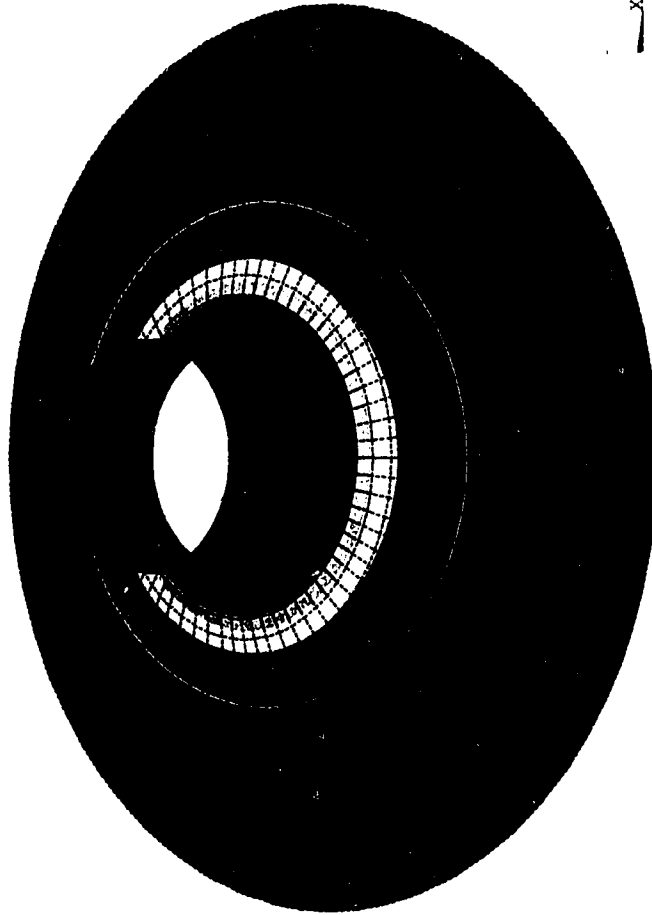
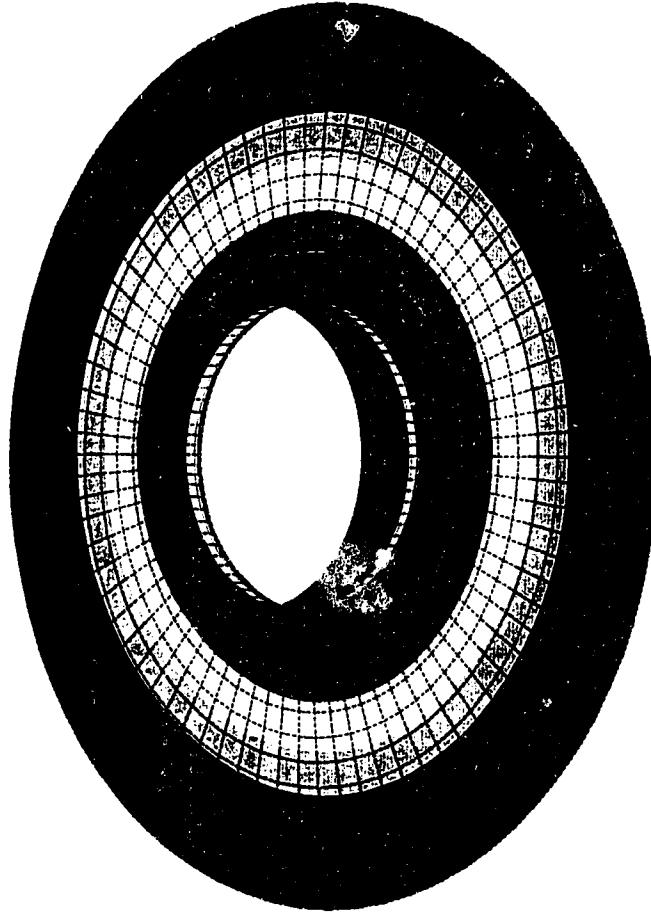


Figure 2-S1 Submodel S6 - Longitudinal Stress

JUN 29 1995  
20:06:15  
PLOT NO. 20  
2242  
4447  
6653  
8859  
11065  
13270  
15476  
17682  
19888  
22093

(psi)



x

Figure 2-8m Submodel S10 - Circumferential Stress

JUN 29 1495  
 20:06:28  
 PLOT NO. 21  
 -33.586  
 1217  
 2467  
 3718  
 4968  
 6219  
 7469  
 8720  
 9970  
 11220  
 (psi)

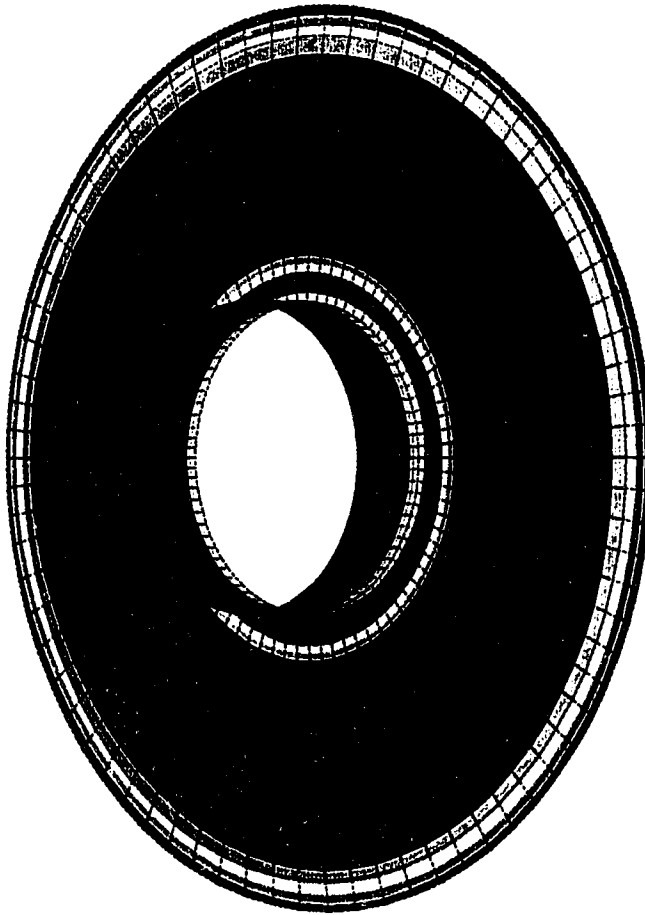


Figure 2-Sn Submodel S10 - Longitudinal Stress

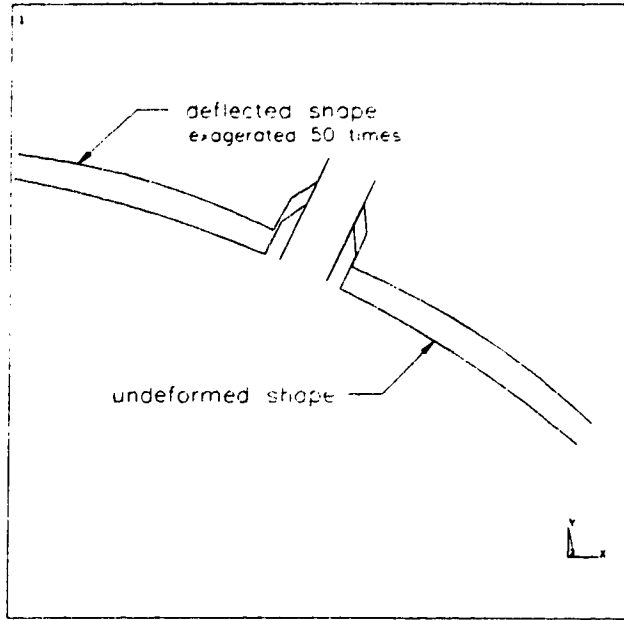


Figure 2-9a Submodel N7 - Circumferential Cut

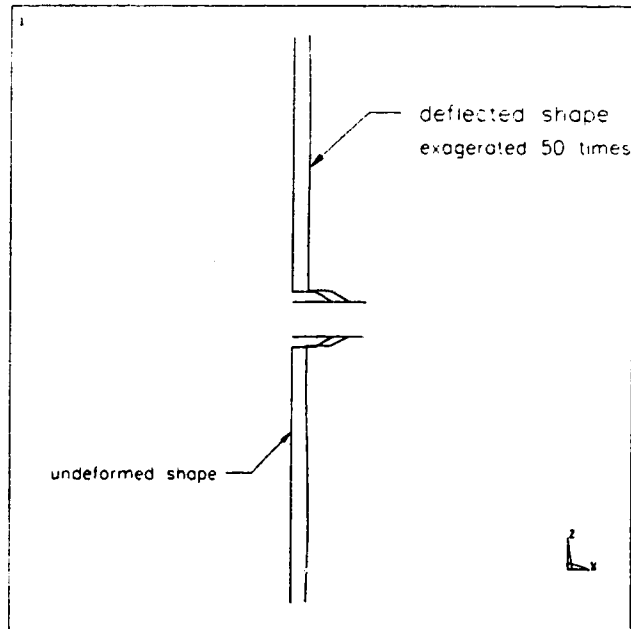


Figure 2-9b Submodel N7 - Longitudinal Cut

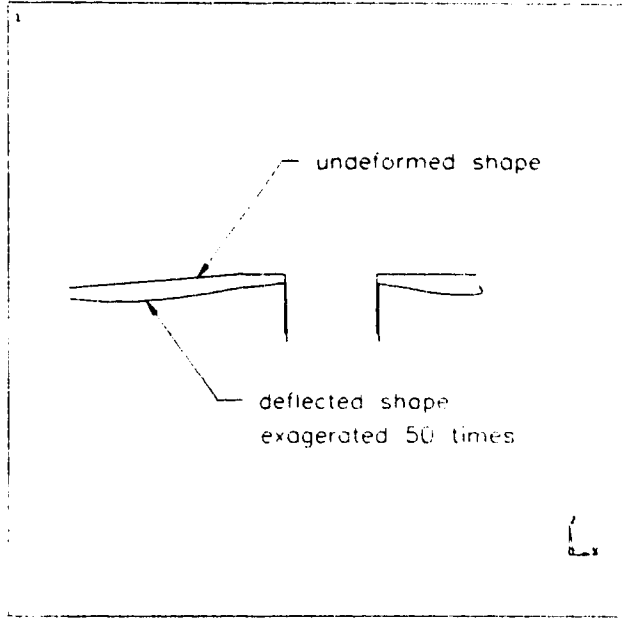


Figure 2-9c Submodel S1 - Circumferential Cut

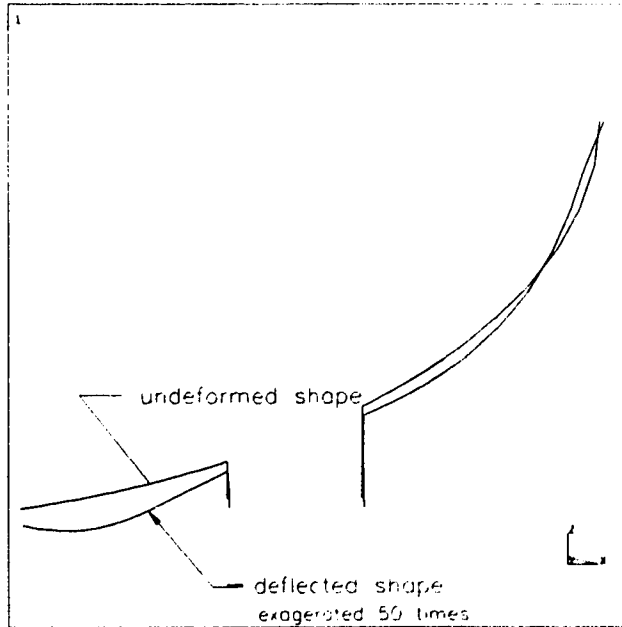


Figure 2-9d Submodel S1 - Longitudinal Cut



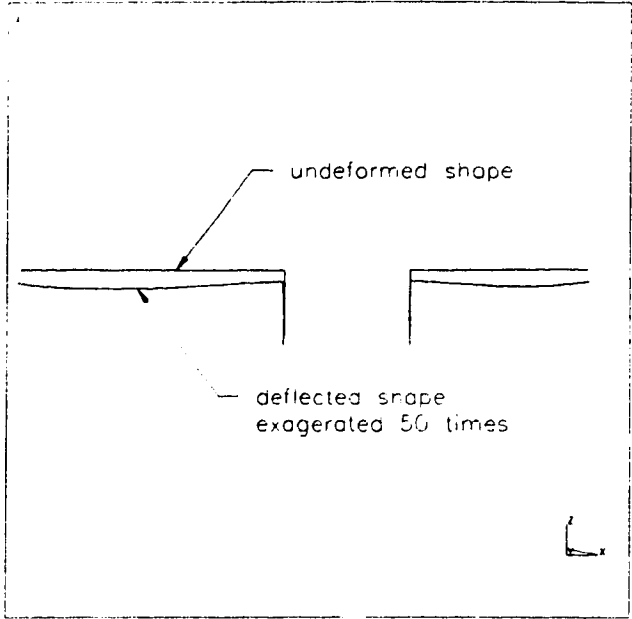


Figure 2-9e Submodel S2 - Circumferential Cut

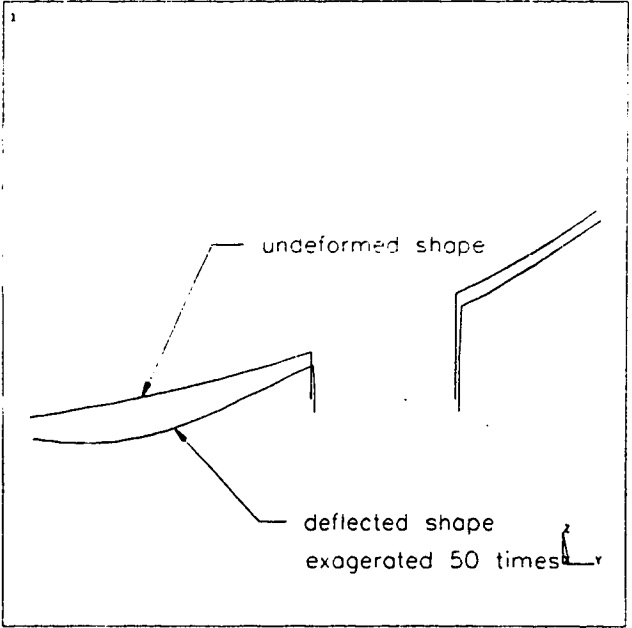


Figure 2-9f Submodel S2 - Longitudinal Cut

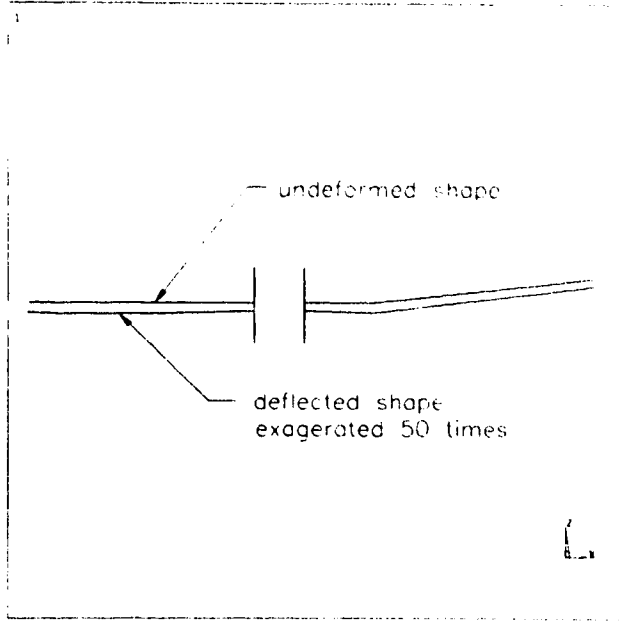


Figure 2-9g Submodel S3 - Circumferential Cut

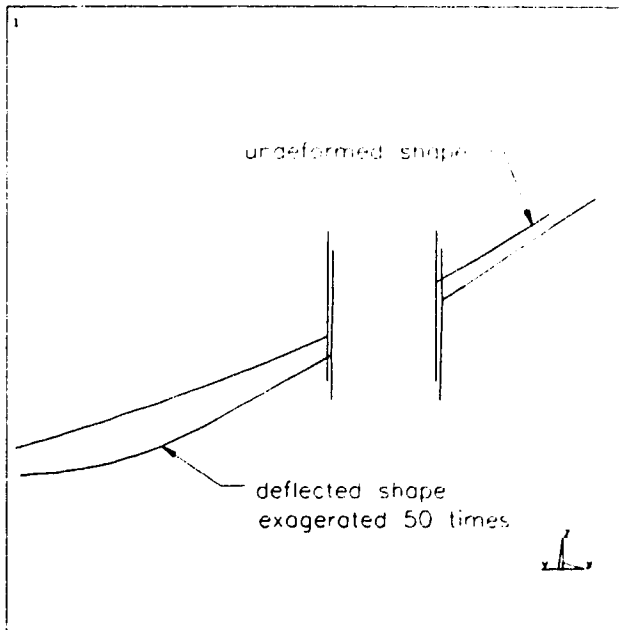


Figure 2-9h Submodel S3 - Longitudinal Cut

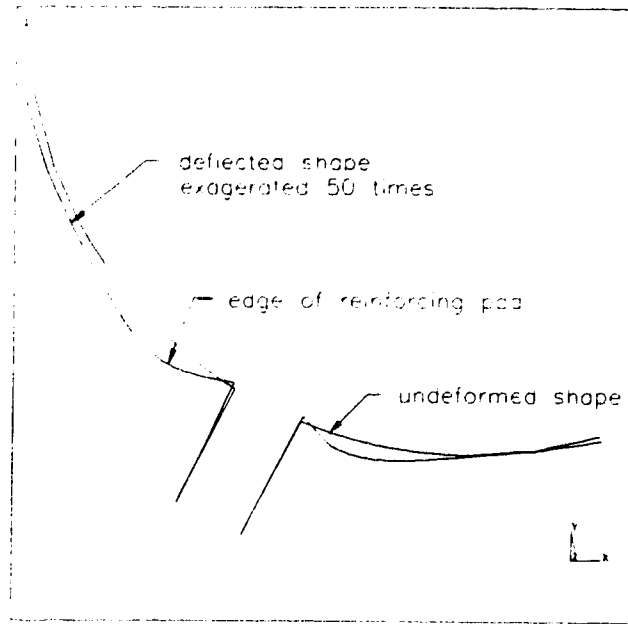


Figure 2-9i Submodel S5 - Circumferential Cut

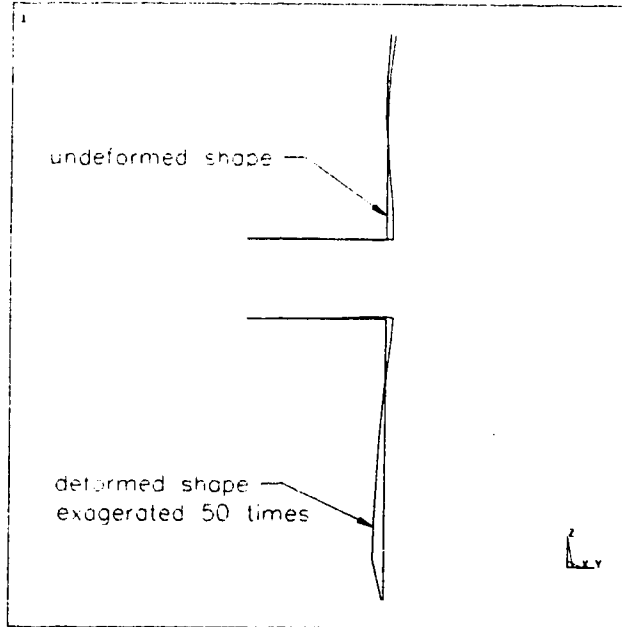


Figure 2-9j Submodel S5 - Longitudinal Cut

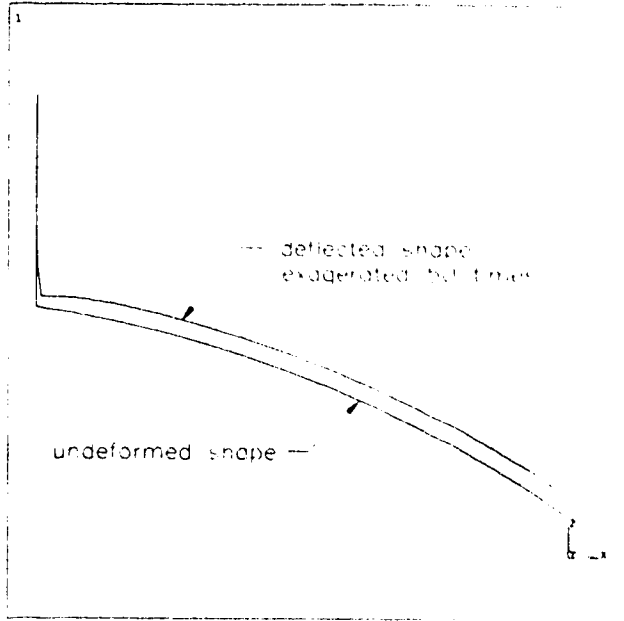


Figure 2-9k Submodel S6 - Longitudinal Cut

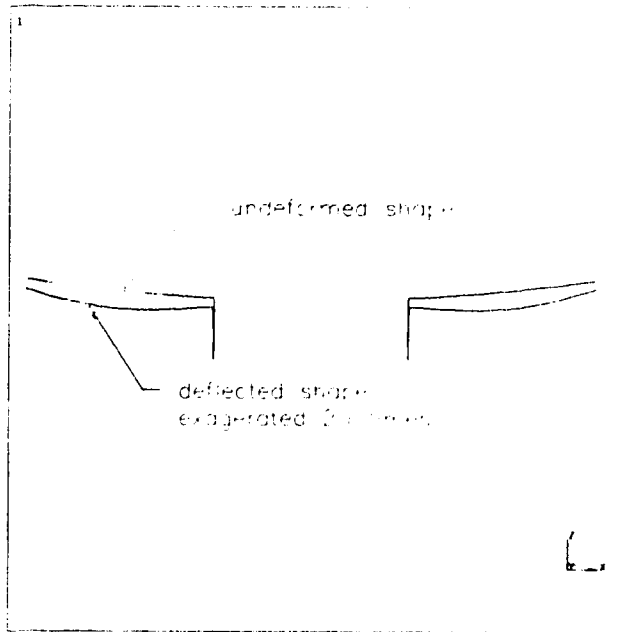


Figure 2-9l Submodel S10 - Longitudinal Cut

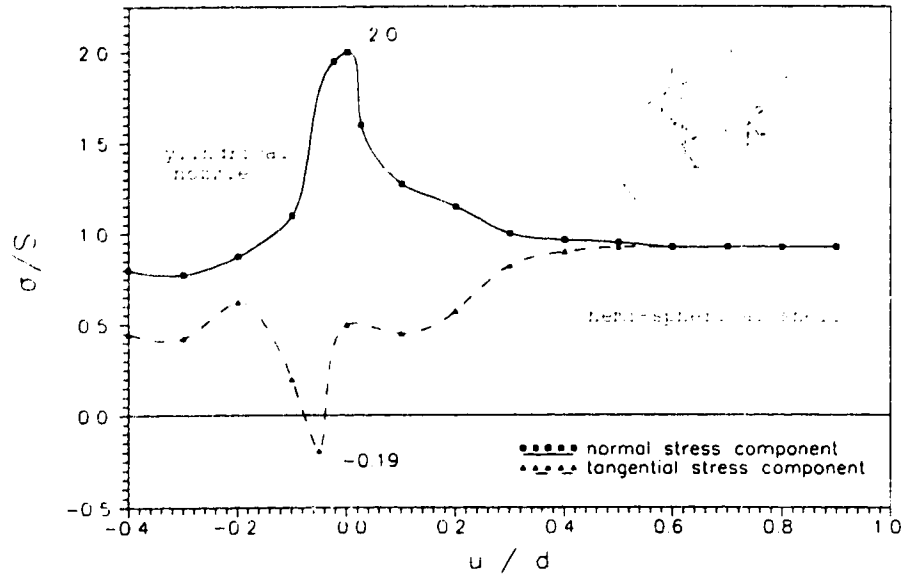


Figure 2-10 Results of a physical experiment showing the trend of the normal and circumferential stress components for a radial cylindrical nozzle in a spherical head [11].

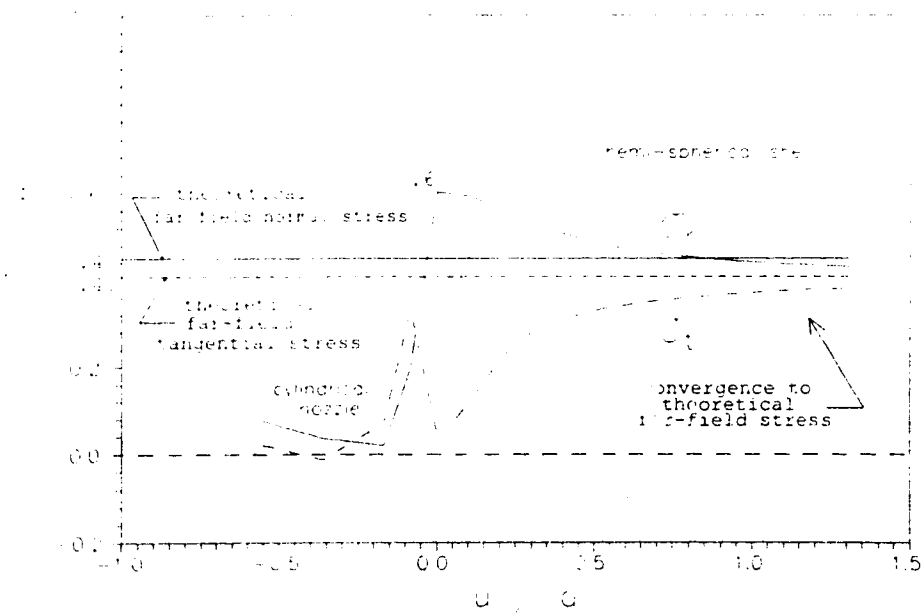


Figure 2-11 Variation of normal and tangential components of stress with distance from the juncture for Submodel S6 subjected to internal pressure. The far-field stress from shell theory [9] is superimposed on this plot.

## REFERENCES

- [1] Gottselig, K. (1991), "8-1C-51 Hot Coke Transfer Line Dynamic Strain Measurement", Materials and Equipment Research, Syncrude Canada Limited, p.1-7.
- [2] Mitchell, J.S. (1992), "8-1C-1, Hot Coke Transfer Line Nozzle, Metallurgical Investigation of 1991 Fracture", QAME Report No. 287-92, Syncrude Canada Limited, p. 1-5.
- [3] Emberley, D. (1993), "Plants 8-1 and 8-2 Hot Coke Transfer Line - Finite Element Analysis: Final Report", Syncrude Canada Limited, ESR No.08-C260, p. 1-38.
- [4] Diallo, B. and F. Ellyin (1983), "Optimization of Connecting Shell", *Journal of Engineering Mechanics*, Vol. 109, No. 1, p. 111-126.
- [5] Bednar, Henry H. (1991), Pressure Vessel Design Handbook, Krieger Publishing Company, Malabar, Florida, p. 32-33, 209.

- [6] *ASME Boiler and Pressure Vessel Code*, Section VIII, American Society of Mechanical Engineers, New York, N.Y., 1992 Edition, 1994 Addenda, p. 347-351.
- [7] DeSalvo, G. J., and R. W. Gorman (1989), ANSYS Engineering Analysis System User's Manual, Swanson Analysis Systems, Inc., Pennsylvania, USA, p. 4.93.1-4.93.5.
- [8] *ASME Boiler and Pressure Vessel Code*, Section II, American Society of Mechanical Engineers, New York, N.Y., 1992 Edition, 1994 Addenda, p.664.
- [9] Flügge, W. (1962), Stresses in Shells, Springer-Verlag, Berlin.
- [10] Harvey, John F. (1991), Theory and Design of Pressure Vessels, Van Nostrand Reinhold, New York, NY, p. 33-48.
- [11] Taylor, C. E. and N. C. Lind (1966), "Photoelastic Study of the Stresses Near Openings in Pressure Vessels", *Welding Research Council Bulletin*, No. 113, p. 1-24.
- [12] COADE Fe/Pipe User Guide, Version 2.7, COADE Research Services, Houston, Texas, p. 4.2.1 - 4.2.2.

## CHAPTER 3

# ELASTIC-PLASTIC ANALYSIS OF A LARGE STEEL PRESSURIZED VESSEL SUBJECTED TO NOZZLE EXTERNAL LOADS

### 3.1 INTRODUCTION

Several nozzle opening attachments on Syncrude Canada Limited's coker burner pressure vessels (hereafter referred to as the burner vessel) are subjected to combined internal pressure and static external loads. The design method used in the pressure vessel industry is to determine limits on such loadings, based on approximate formulas with large factors of safety built into them to account for the unknown or omitted items, such as the extent of yielding or the material behaviour [1]. This practice often results in grossly over-designed components and a waste of material and fabrication time. Chapter 3 of this thesis presents an elastic-plastic solution to this pressure vessel problem obtained by applying the finite element method.

There has been considerable work done, theoretically and experimentally, towards determining the plastic limit of unpierced cylindrical and spherical shells [2]. There is also extensive literature on plastic limit theory of axisymmetric intersecting shells [3, 4, 5, 6], as well as experimental investigations [7, 8, 9]. However, these investigations were limited to the axisymmetric case of a radial cylindrical nozzle intersecting a spherical shell, and only the limit pressure was determined. Much less work has been done on the determination of the limit pressure of intersecting cylinder/cylinder shells [10] or the



plastic limits for external loads on nozzles [11]. In determining the limit load, the material is assumed to be elastic-perfectly-plastic, and thus the limit load is associated with the gross (unconstrained) plastic flow.

The purpose of this investigation was to perform an elastic-plastic analysis of the two worst case burner vessel nozzle openings subjected to the following loads: combined internal pressure and in-plane (inplane) or out-of-plane (outplane) moments, and combined internal pressure and inplane or outplane shear forces. This was accomplished by developing a finite element model of the nozzle-shell intersection regions and performing an elastic-plastic analysis of the model using the ANSYS program. The results from this analysis were used to determine the plastic limit of the nozzle-shell intersection.

## **3.2 PHYSICAL CONDITIONS**

### **3.2.1 Nozzle Geometry**

Analyses of two nozzle openings into the burner vessel were performed for this investigation. The first was nozzle mark number S6, a 96" [2438 mm] I.D. nozzle which projects radially from the crown of the spherical top head. This nozzle was of particular interest because intermittent repairs on the piping line leading from the nozzle result in various static external piping loads on the nozzle-shell connection.

The second opening considered was nozzle mark number N7, a 22" [559 mm] I.D. opening reinforced with an insert plate and located on the cylindrical shell portion of the

burner vessel. The nozzle-shell juncture at this opening was determined to be the worst case nozzle in terms of stress by the elastic finite element analysis of the burner vessel detailed in Chapter 2.

### 3.2.2 Fabrication Material

The spherical and cylindrical shells and the cylindrical nozzle necks considered in this analysis were fabricated from ASTM A-516 Grade 70 low alloy steel. The burner vessel was fabricated in 1971 and has undergone several hundred loading cycles, such as shutdowns and startups. For this reason, it was assumed that the monotonic stress-strain behaviour for virgin ASTM A-516 Grade 70 material would no longer be representative of the vessel material. Instead, the cyclic curve for ASTM A-516 Grade 70 material was approximated using piecewise linear segments and incorporated into the finite element model as the monotonic stress-strain response of the material. The cyclic curve was found in the literature [12] and is given according to the following equation:

$$\epsilon = \frac{\sigma}{E} + \left(\frac{\sigma}{E_0}\right)^{1/n}$$

where

$$E = 28.7 \times 10^6 \text{ p.s.i.}$$

$$E_0 = 0.155 \times 10^6 \text{ p.s.i.}$$

$$n = 0.193$$

The cyclic curve and the piecewise linear approximation of it are plotted in Figure 3-1.

### **3.3 FINITE ELEMENT MODEL**

#### **3.3.1 FEA Software and Hardware**

All modelling and analyses were performed using the ANSYS program version 5.0 running on the IBM RISC System/6000 hardware located in the University of Alberta's Mechanical Engineering Building.

#### **3.3.2 Hardening Behaviour**

The finite element submodels of nozzles S6 and N7, developed to perform the elastic analysis of the burner vessel detailed in Chapter 2, were modified for use in this investigation. Specifically, the material behaviour of each submodel was changed from linear elastic to that of kinematic hardening elastic-plastic material. A kinematically hardening material model was considered adequate since the plastic limits for the external nozzle loads were obtained by simulating all loading in a quasi-static and monotonically

increasing manner.

The multi-linear kinematic hardening model available within the ANSYS program was used to accomplish this modification. The piecewise approximation of the cyclic curve plotted in Figure 3-1 was inputted as the monotonic stress-strain response of the modelled material.

### **3.4 LOADING AND BOUNDARY CONDITIONS**

#### **3.4.1 Direction Notation**

The intersection geometry of the nozzle-shell intersections is given by the axial, inplane, and outplane directions, which are defined as follows [13]:

- The axial direction is along the axis of the nozzle and positive out of the vessel.
- The inplane direction is perpendicular to both the axis of the nozzle and the axis of the vessel. The positive sense for this vector is arbitrary.
- The outplane direction is formed by crossing the inplane direction into the axial direction.

This direction notation is consistent with the right hand rule and is illustrated in Figure 3-

2. Thus, according to this notation an inplane moment produces deflection that is symmetric in the out-plane, while an inplane force produces a deflection that is symmetric in the in-plane. For example, moments and shear forces applied to the radially axisymmetric nozzle  $\text{E6}$  are referred to as outplane and inplane, respectively, because of

the deflections developed.

### **3.4.2 Boundary Conditions**

The boundary conditions applied to the submodels were those determined from the elastic analysis of the global model detailed in Chapter 2. As described in Chapter 2, the boundaries of the submodels were selected in such a way as to be outside the attenuation length of the local stresses developed near the nozzle openings.

The boundary conditions prescribed approximately represent the physical boundaries corresponding to the external load cases. That is, a much higher stiffness at the boundary than that which can physically be expected at the boundaries has been assumed. The result of this assumption is that a secondary stress field develops in the finite element model due to the prescribed boundary conditions. However, this secondary stress field was shown to be well within the elastic range of the material and, most importantly, to diminish very rapidly with distance from the boundary. The attenuation of the secondary stress field is evident in Figure 3-3. The short attenuation length of this secondary stress field suggests that the boundary conditions do not significantly influence the stress results in the region of interest, the nozzle/shell intersection, and that the prescribed boundary conditions are, therefore, adequate.

### **3.4.3 Applied Loads**

The external loading conditions considered in this investigation were inplane and outplane shearing forces and inplane and outplane moments. Each of these external loading conditions was applied to each submodel in combination with the internal design pressure of the burner vessel listed in Table 2-3.

Figures 3-4a to 3-4f show the simulated external loading on each submodel. For the sake of clarity, the vectors indicating the internal pressure are not shown in some cases. The length of the outside projection of the nozzles from the shell wall is illustrated in these figures. This projection was 53" and 23.4" for S6 and N7, respectively, giving a projection-to-diameter ratio of about 1:1 for both N7 and S6.

### **3.5 RESULTS**

The plastic limit was determined for Submodels S6 and N7 subjected to inplane or outplane moments combined with internal pressure and inplane or outplane shear forces combined with internal pressure.

#### **3.5.1 Plastic Limit Load**

In contrast to an elastic-perfectly-plastic material, a strain hardening material does not exhibit a distinct limit load. In the latter case, the plastic limit, or limit load, for each nozzle and loading configuration is defined by the load corresponding the intersection of the line of elastic response and the tangent of the plastic behaviour. In the case of

determining limit pressures, this method was reported in the literature to result in a limit pressure which compared reasonably closely with that determined using other reported methods, such as the 0.2% strain offset approach, and also to agree well with the experimentally observed limit pressure [10, 11]. Figure 3-5 illustrates the approach of determining the plastic limit by intersection of the elastic and tangent to the plastic response. Figures 3-6a to 3-6f are plots of the simulated inplane external moment, outplane external moment, inplane shear, and outplane shear force verses the deflection at the point of load application. The initial elastic behaviour is apparent, as is the gradual onset of plastic behaviour and hardening. The limit loads found using the tangent approach for each loading and nozzle considered are listed in Table 3-1 and shown in Figures 3-6a to 3-6f. The tangent lines used to determine these limit loads have been superimposed over Figures 3-6a to 3-6f and have been included in the appendix of this thesis as Figures A-1 to A-6.

Since the shear force to which the submodels were subjected was applied at the tip of the external projection of the nozzles, it was reasonable to assume that the shell would be subjected to an associated moment equal to the shear force times a moment arm equal in length to the external projection of the respective nozzles. Figure 3-7 is a plot of this associated moment verses the deflection at the point of load application. The curves for the applied external moments have been superimposed onto the plot for comparison.

It is evident from Figures 3-7a and 3-7b that there is no significant difference in the limit load for an outplane moment and an inplane shear, or an inplane moment and an outplane shear. This suggests that the moment developed because of the offset of the shear

force from the vessel shell, and not the shear force itself, governs the onset of plasticity.

The stiffness of each nozzle shell intersection for each loading condition is reported in Table 3-1. These stiffness values represent the slope of the tangent to the elastic response and were calculated according to the following equation for external shear loads:

$$stiffness = \frac{force}{displacement}$$

and by

$$stiffness = \frac{moment}{rotation}$$

for external moments.

It can be seen from Figures 3-7a and 3-7b, as well as by comparing the Submodel N7 stiffness values listed in Table 3-1, that the vessel cylindrical shell is 30% stiffer in the inplane direction than in the outplane direction. Further, comparison of the Submodel N7 limit loads listed Table 3-1 demonstrates that the limit load associated with the outplane moment is 4% lower than the limit load associated with the inplane moment for this geometry. Thus, this data suggests that the outplane moment is the critical case of the external loads considered. For the case of the spherical shell, outplane external loads give results that are identical to those of inplane external loads.

Figure 3-8 is a plot of inplane moment and outplane moment verses deflection from



physical experiments found in the literature [11]. The curves in this figure represent the deflection near the point of load application, similar to the curves plotted in Figure 3-6. Comparing the tangent to the elastic response for the inplane and outplane moment curves plotted in Figure 3-8 gives the stiffness to be 35% lower for the outplane moment case than for the inplane moment case. This is in agreement with the trend shown in Figures 3-7a and 3-7b.

The equivalent plastic strain distributions at the plastic limit for Submodels S6 and N7 subjected to external loadings are shown in Figure 3-9a to 3-9f. This figure illustrates the locations at which the onset of plastic flow begins.

Comparing Figures 3-9e and 3-9f demonstrates that the plastic strain intensity developed at the limit load in Figure 3-9f, the outplane moment case, is 35% greater than that shown in Figure 3-9e, the inplane moment case. This result is consistent with the trend shown by Figures 3-7a and 3-7b.

Figure 3-10 is a plot of the equivalent stress at the plastic limit for each case. Figures 3-9 and 3-10 are useful in that they provide insight into locations on the physical vessel where the strain should be monitored should high external loadings be anticipated.

### **3.5.2 Allowable Load**

The ASME Boiler and Pressure Vessel Code [14] requires that the allowable loading be limited to 2/3 of the load at the plastic limit corresponding to a factor of safety of 1.5. This is consistent with the factor of safety recommended by the same code as the

limit of the developed stress intensity relative to the yield stress intensity of the material. Figure 3-5 illustrates the allowable load relative to the plastic limit of a given load-deflection response of a system. That the ASME Code provides for an approach based on design by limit loads is of practical importance since nearly all pressure vessel designs, including that of the burner vessel, must be in accordance with this code.

### 3.5.3 Effect of Substep Size

An accurate solution to the finite element problem could not be expected if the full loads were applied to the submodels in a single step since the material response over the entire range of applied loading was non-linear. For this reason, the external loading and the internal pressure were applied to the submodels using incremental loading, or substeps, equal to 5% of the final load to be applied. The solution was obtained for each substep consecutively, and the material response was updated at each substep to account for the change in radius with the increasing load.

The substep size used was adequate to ensure that the analyses performed with a 10% substep size. This was verified by re-solving Submodels S6 and N7 increment, the worst case external loading, using a substep size equal to 10% of the final applied loads and comparing the results from this analysis to those found using a 5% substep size.

Figure 3-11a and 3-11b are plots of the load-deflection curves found using the 10% substep size superimposed over the curves found using the 5% substep size for each

submodel. These curves agree well, demonstrating that the 5% substep size was adequate.

#### **3.5.4 Effect of Element Size**

The effect of the element size was tested by comparing the load-deflection plots, and thus the plastic limits, predicted using two different mesh densities. The first prediction was made by solving Submodel S6 meshed using 960 elements. This was the same as the mesh used to determine the limit loads already reported. The second prediction was obtained solving a model similar to Submodel S6 meshed using 2340 elements.

The resulting load-deflection curves predicted using the two different mesh densities are plotted in Figure 3-12. This figure demonstrates that the solution has converged with the mesh density used for Submodel S6 since more than doubling this number of elements produces no significant change in the load-deflection response of the submodel. That is, the element size was sufficiently small to ensure that the results were insensitive to the element size.

### **3.6 DISCUSSION OF RESULTS**

The inplane stiffness and the outplane stiffness of each nozzle was determined by this analysis. This data is valuable in designing the piping that connects to the nozzle openings of the burner vessels.

Conventional piping design does not provide a practical means for determining the stiffness of a pressure vessel shell near a nozzle opening. Therefore, the extremely conservative assumption of an infinitely stiff shell is usually made by piping designers. The result of this assumption is that the ability of the shell material to deflect when subjected to external loads from the attached piping is not used to advantage in the design of the piping. Thus, piping is typically and unnecessarily over-designed in order to limit the external loads transferred by the piping to pressure vessel nozzles.

In comparing the individual load cases, the one of outplane moment appears to be the most critical. The plastic limit for this case is 4% lower than for the inplane moment case. Further, the stiffness of the outplane moment case is 35% less than for the inplane case. Therefore, although the allowable design limit for both of these cases would be very close, for a comparable applied load the deformation for the outplane case would be significantly larger than that for the inplane case.

This investigation was concerned with determining the plastic limit, or limit load, of the burner vessels' nozzle openings S6 and N7. This plastic limit has been determined as being a specific number and is listed for each load case in Table 3-1. The physical meaning of what this plastic limit represents is a yield point followed by deformations that become large and which is specific to the problem under consideration.

For load cases and geometries observed, restricting occasional operating loads using the plastic limit as a yield point would be conservative since there was significant load carrying capacity after the plastic limit was exceeded.

### **3.7 SUMMARY OF RESULTS**

Finite element submodels of nozzle S6, a radial cylindrical nozzle opening into a spherical shell, and N7, a radial nozzle opening into a cylindrical shell were developed. Inplane or outplane moments combined with internal pressure or inplane or outplane shear forces combined with internal pressure were each simulated. An elastic-plastic analysis was then performed using the program ANSYS in order to determine the plastic limit, or limit load of each loading combination.

One of the submodels was checked to ensure that the element size was sufficient such that the solution obtained was not influenced by the element size used. Both submodels were checked to ensure that the substep size was sufficiently small so as to not influence the results. The substep size used and the mesh density used were shown to be adequate.

The outplane moment combined with internal pressure was found to be the critical case of the loading conditions considered. This result is in good agreement with results of an experimental study from the literature.

### 3.8 CONCLUSIONS

Opening S6, a radial cylindrical nozzle intersecting the spherical shell portion of each of the coker burner pressure vessels, and opening N7, a radial cylindrical nozzle intersecting the cylindrical shell portion of each of the coker burner pressure vessels, were analysed in order to determine the plastic limits for several load cases. The load cases considered were combined internal pressure and inplane or outplane moment and combined internal pressure and inplane or outplane shear. This was accomplished by developing a model for each opening using the finite element method and by performing a nonlinear stress/strain analysis of these models using the program ANSYS. The finite element results were compared qualitatively against the results from physical experiments found in the literature.

The results of the finite element analysis performed lead to the following conclusions:

- I. The results from the finite element submodels of the burner vessel nozzle-shell intersection regions were used to predict the plastic limit of the nozzles subjected to combined external loading and internal pressure.
- II. These results were used to gain an insight into the elastic-plastic response of the vessel shell in the vicinity of openings.
- III. It was demonstrated that the finite element results converged for varying element sizes and substep sizes when subjected to combined external loads and internal pressure.

- IV. The results from the finite element analysis were used to calculate the stiffness of the nozzle-shell intersection regions of the burner pressure vessels.
- IV. The stiffness of the burner vessel shell was predicted for each of the following external load cases combined with internal pressure: inplane moment, outplane moment, inplane shear, and outplane shear.
- V. The outplane moment combined with internal pressure was found to be the critical case of the loading conditions considered. This conclusion demonstrated good agreement with physical experiments from the literature.

**Table 3-1**

Calculated Limit Loads for Nozzles S6 and N7

Nozzle Mark Number	Applied External Load	Limit Load (x 10 <sup>6</sup> )	Stiffness (x 10 <sup>6</sup> )
S6	Outplane Moment	53 lb-in. [6.0 N-m]	3400 lb-in/rad. [1500 N-m/rad.]
	Inplane Shear	0.90 lb. [4.0 N]	0.67 lb/in. [117 N/m]
N7	Inplane Shear	0.28 lb. [1.2 N]	0.18 lb/in. [32 N/m]
	Outplane Shear	0.29 lb. [1.3 N]	0.24 lb/in. [42 N/m]
	Inplane Moment	5.7 lb-in. [0.64 N-m]	80 lb-in/rad. [350 N-m/rad.]
	Outplane Moment	5.5 lb-in. [0.62 N-m]	56 lb-in/rad. [238 N-m/rad.]



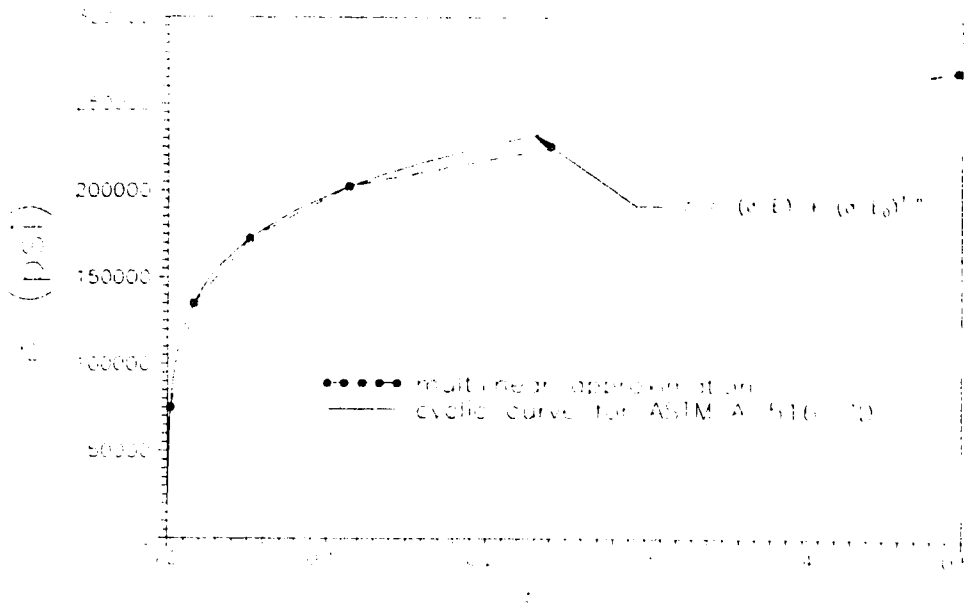


Figure 3-1 A plot of the cyclic curve for ASTM A-516 Grade 70 mild steel [12] and the piecewise linear approximation of the cyclic curve.

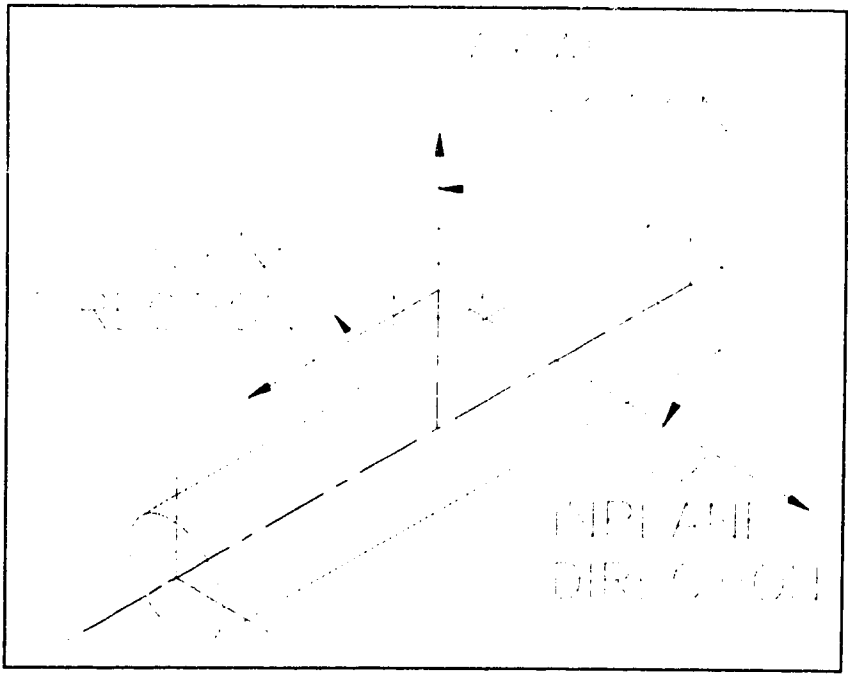


Figure 3-2 Definition of inplane and outplane directions.

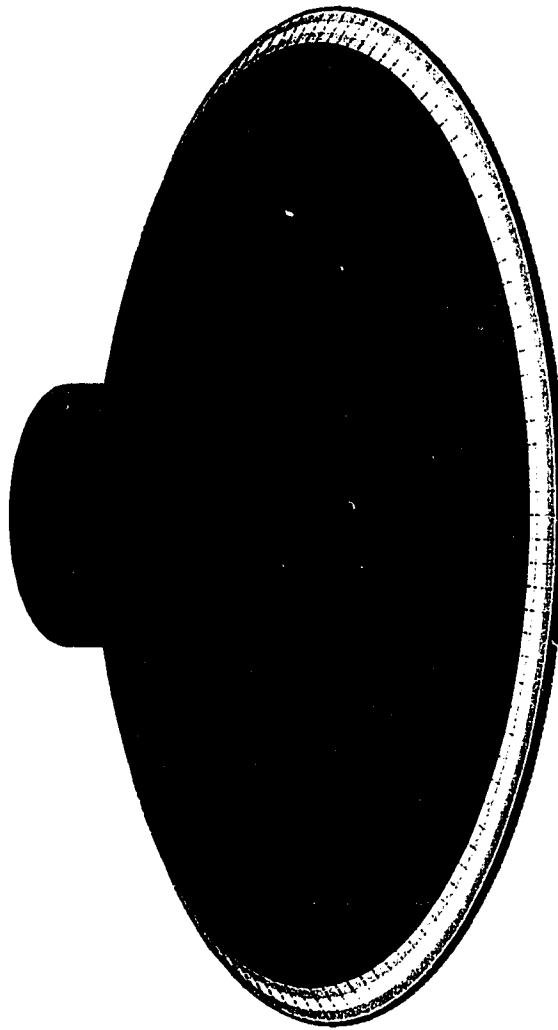
**AN**

FEB 13 1996  
19:34:38  
PLOT NO. 1



(psi)

27.698  
1042  
2056  
3070  
4084  
5098  
6112  
7126  
8140  
9154



X

Figure 3-3 Equivalent stress due to the boundary conditions.

JUN 30 1995  
12:35:37  
PLOT NO. 1  
ELEMENTS  
TYPE NUM

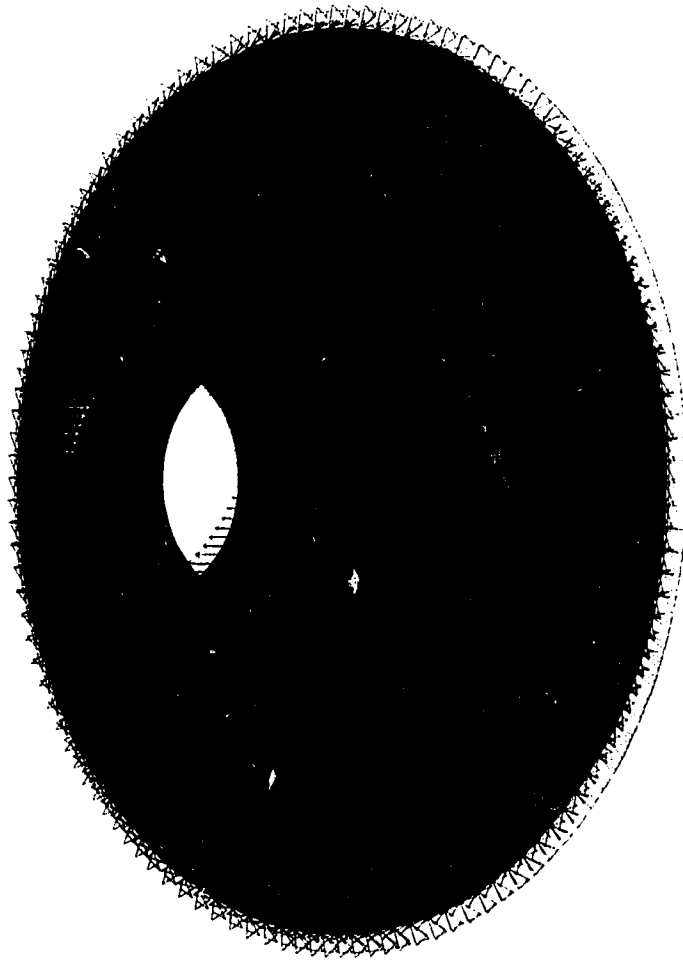


Figure 3-4a Submodel S6 subjected to a simulated outplane moment.

JUN 30 1995  
12:08:22  
PLOT NO. :  
ELEMENTS  
TYPE NUM

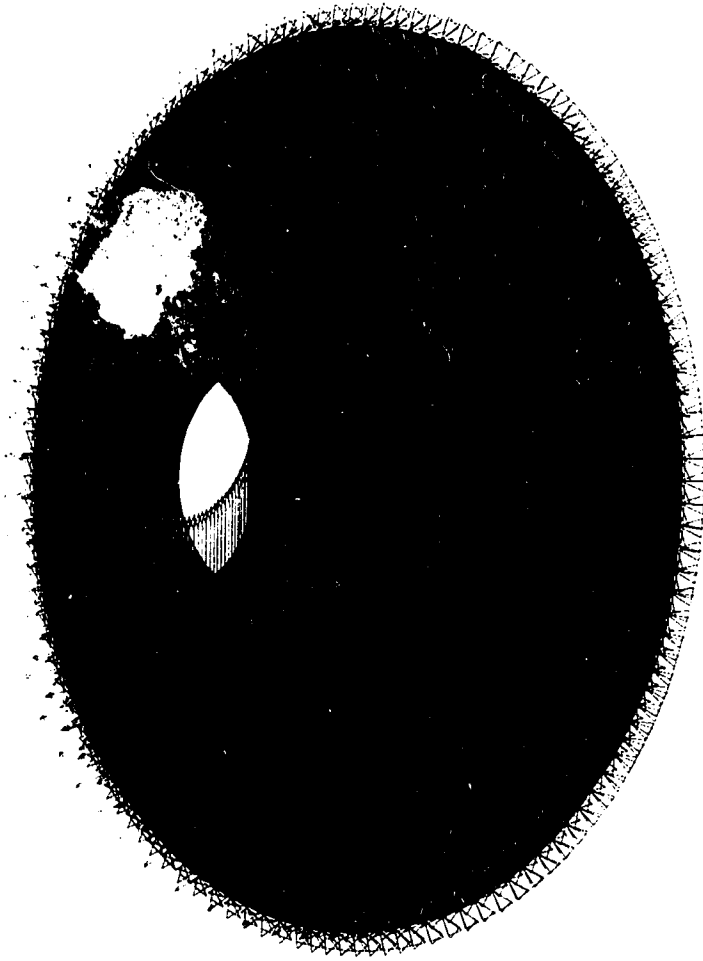


Figure 3--4b Submodel S6 subjected to a simulated inplane shear force.

JUN 30 1995  
12:48:44  
PLOT NO. 1  
ELEMENTS  
TYPE NUM

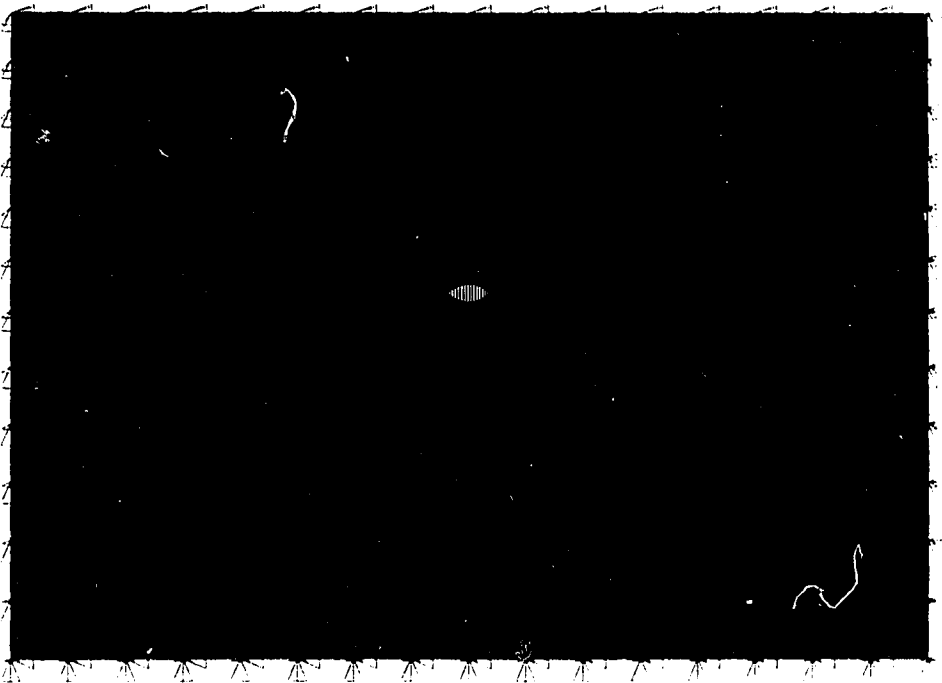


Figure 3-4c Submodel N7 subjected to a simulated inplane shear force

JUN 30 1995  
12:49:11  
PLOT NO  
ELEMENTS  
TYPE NUM

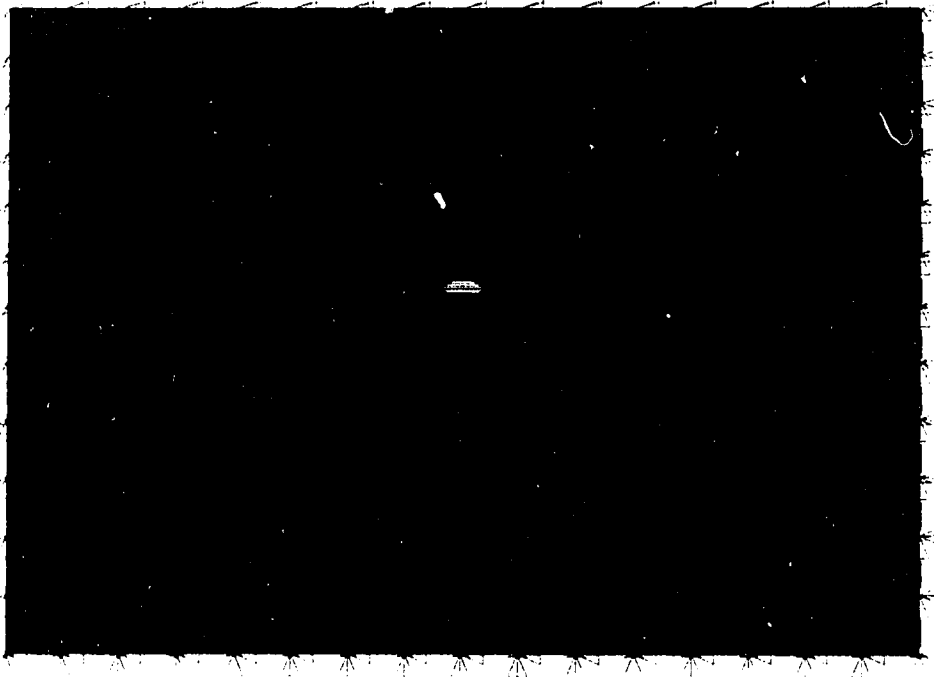


Figure 3-4d Submodel N7 subjected to a simulated outplane shear force.

JUN 30 1995  
12:39:04  
PLOT NO. 1  
ELEMENTS  
TYPE NUM

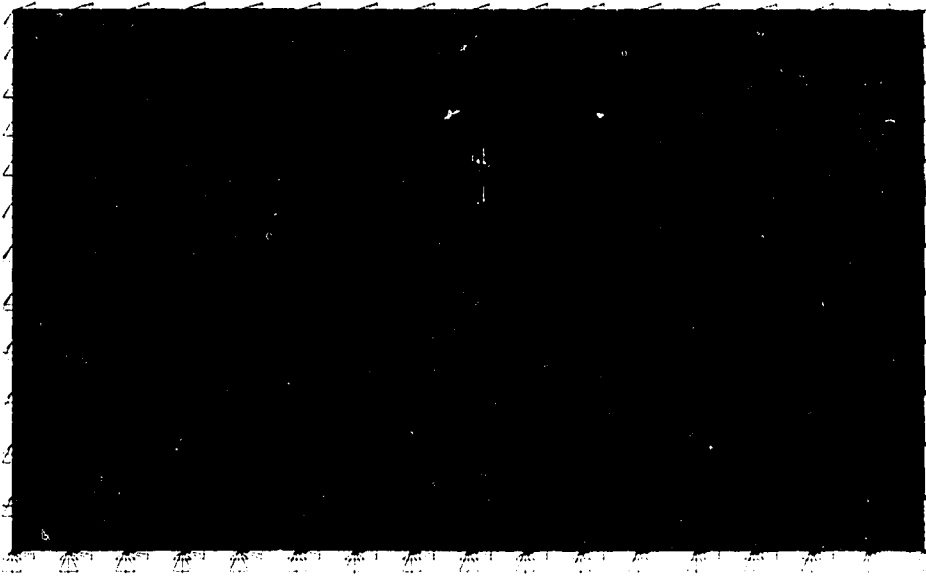


Figure 3-4e Submodel N7 subjected to a simulated inplane moment





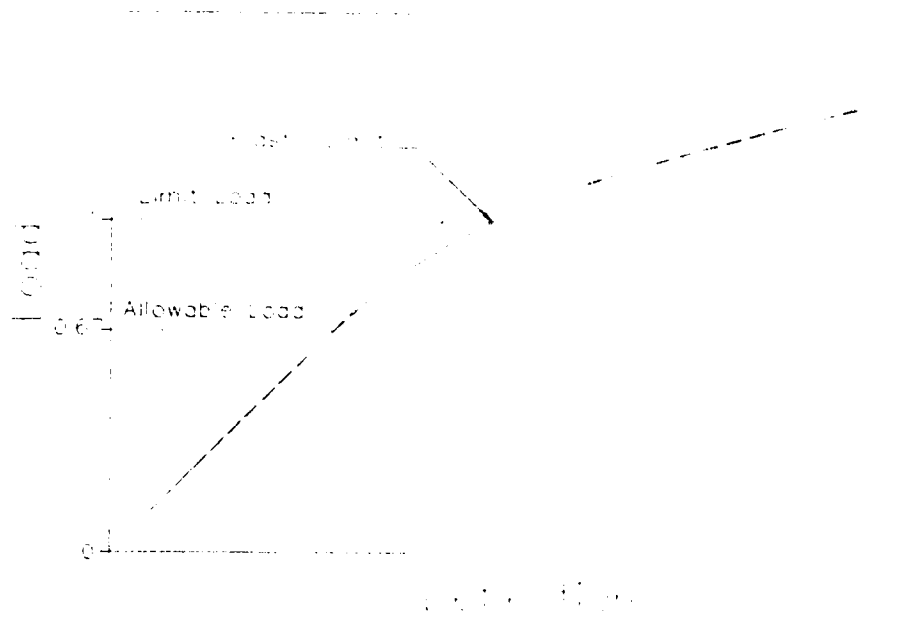


Figure 3-5 Definition of plastic limit, or limit load, and allowable load.

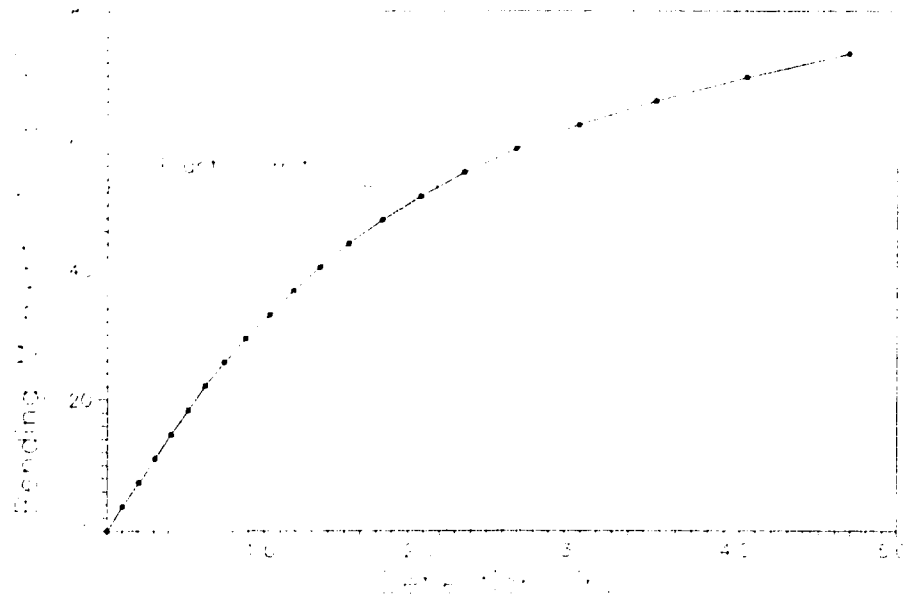


Figure 3-6a Bending moment verses displacement for Submodel S6 subjected to an outplane bending moment.

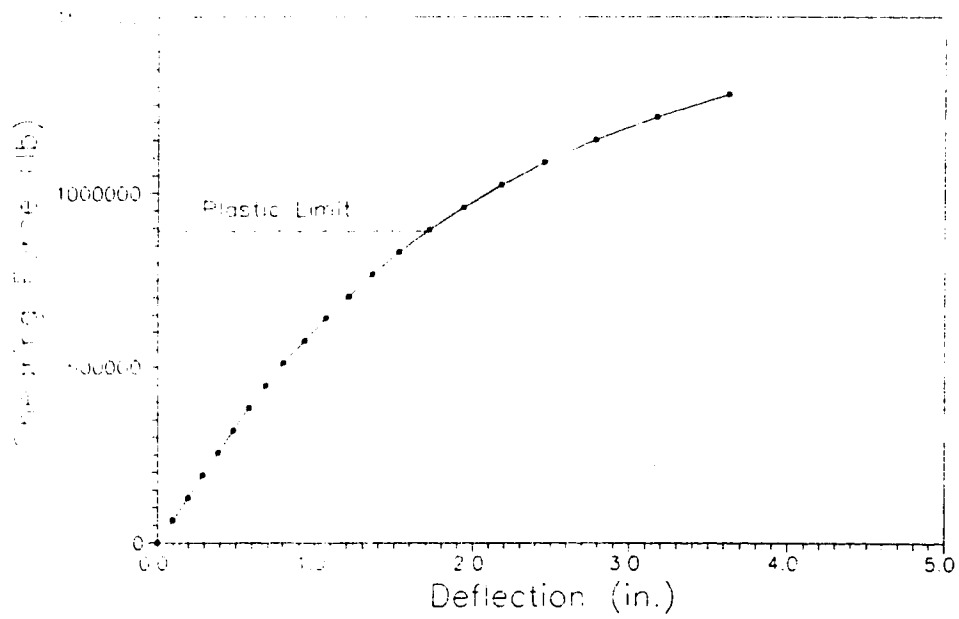


Figure 3-6b Shearing load verses displacement for Submodel S6 subjected to an inplane shear force.

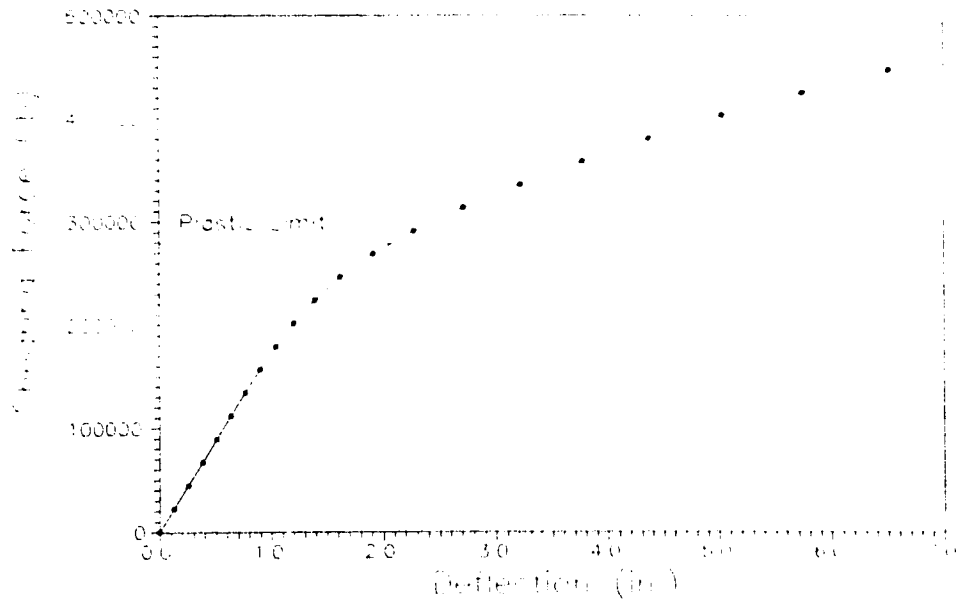


Figure 3-6c Shearing load versus displacement for Submodel N7 subjected to an inplane shear force.

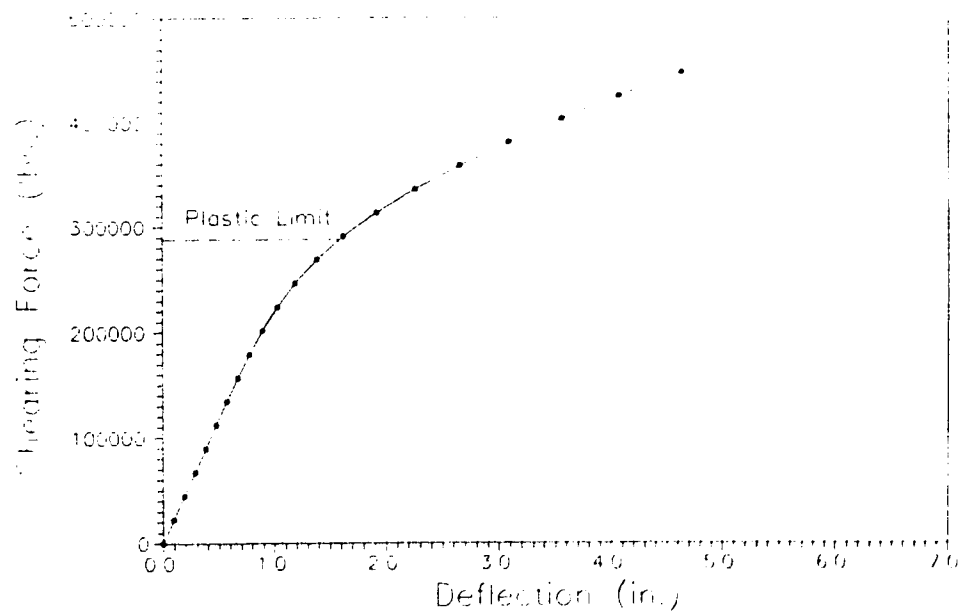


Figure 3-6d Shearing load versus displacement for Submodel N7 subjected to an outplane shear force.

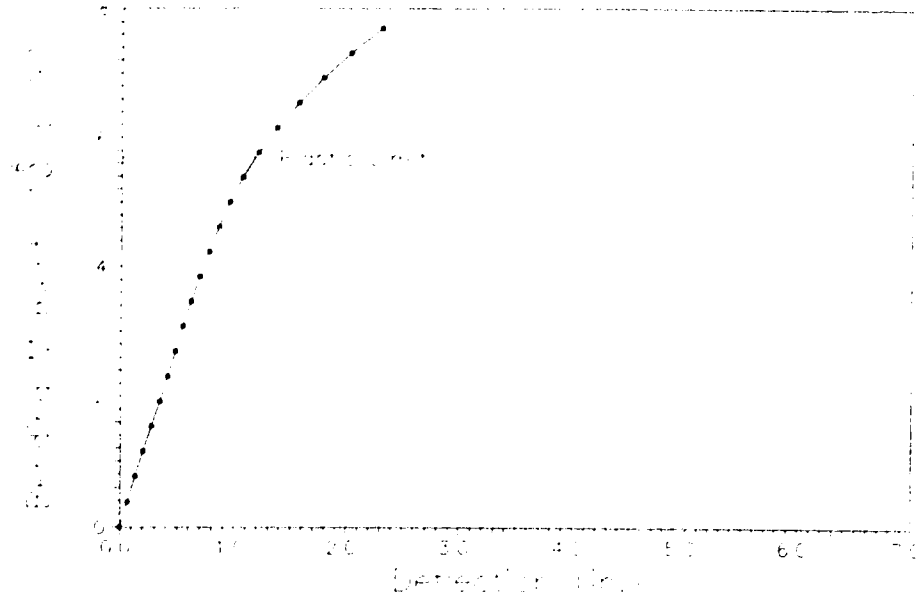


Figure 3-6e Bending moment displacement for Submodel N7 subjected to an inplane moment.

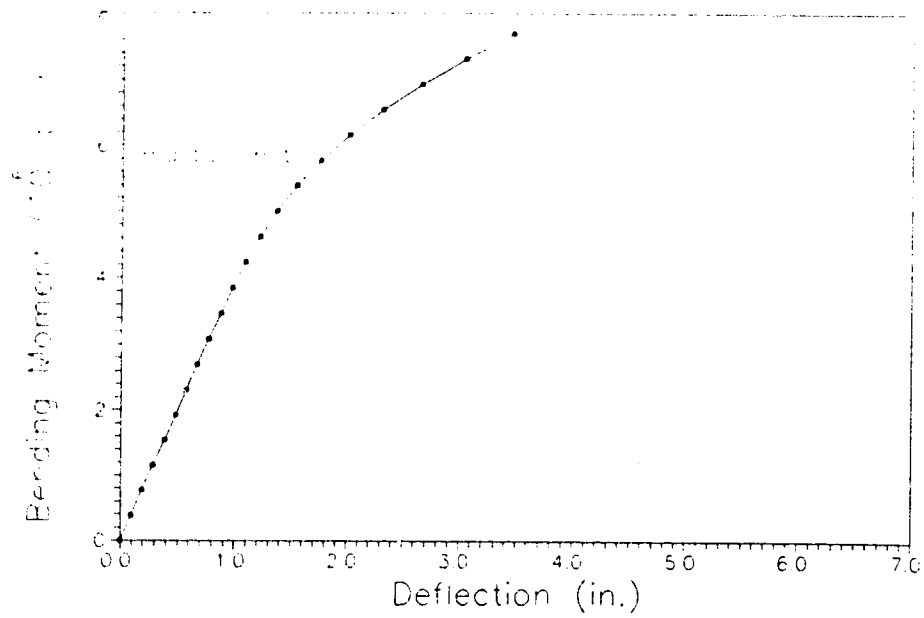


Figure 3-6f Bending moment verses displacement for Submodel N7 subjected to an outplane moment.

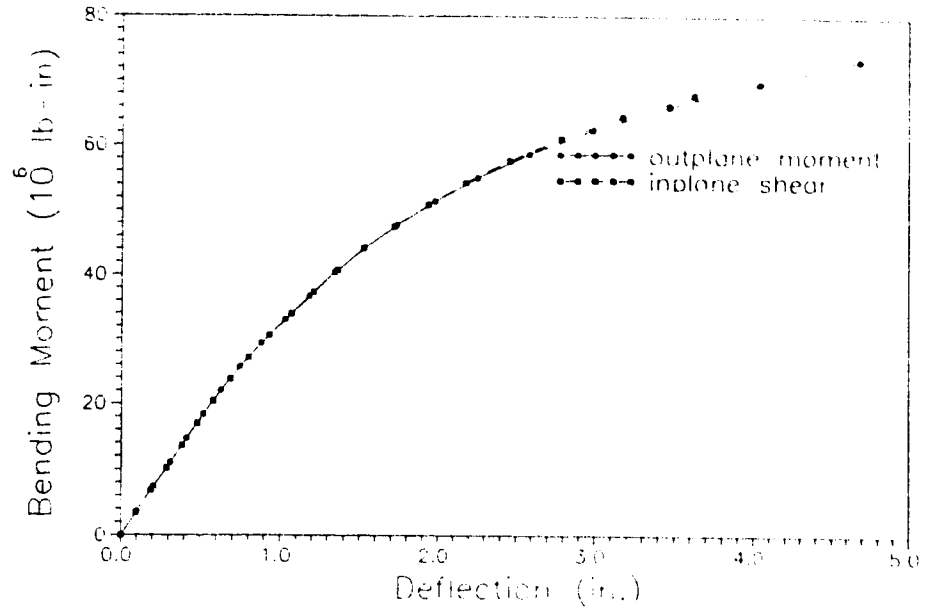


Figure 3-7a Moment verses displacement for Submodel S6.

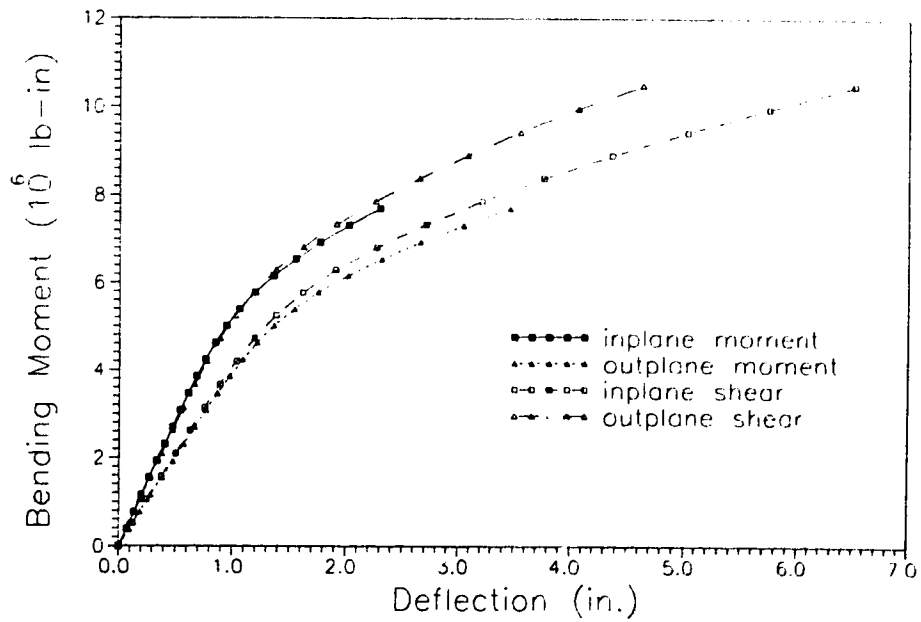


Figure 3-7b Moment verses displacement for Submodel N7.

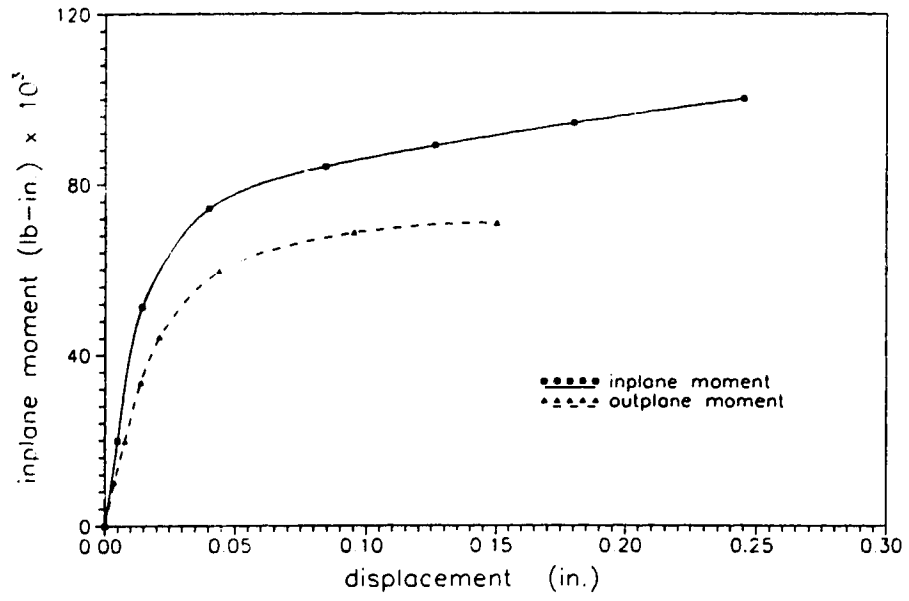


Figure 3-8 Inplane and outplane moments verses displacement indicated by dial gauges [11].

JUN 30 1995  
 12:37:07  
 PLOT NO. 3  
 0  
 .684E-03  
 .001367  
 .002051  
 .002734  
 .003418  
 .004101  
 .004785  
 .005468  
 .006152

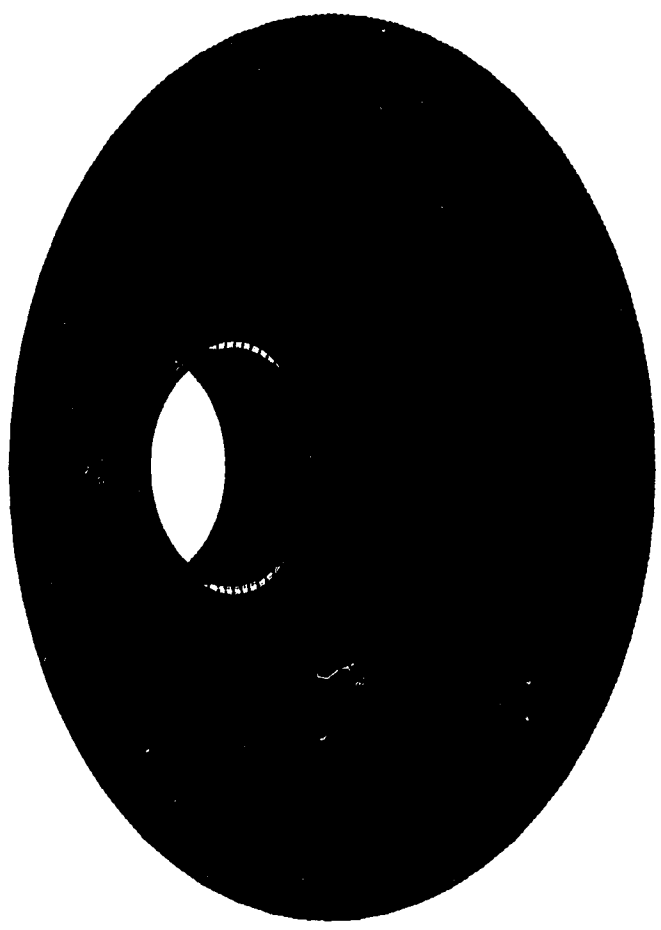


Figure 3-9a Equivalent plastic strain distribution at the plastic limit for Submodel S6 subjected to an out-plane moment.

JUN 30 1995  
12:06:56  
PLOT NO. 1



0  
.491E+03  
.982E+03  
.001473  
.001965  
.002456  
.002947  
.003438  
.003929  
.00442

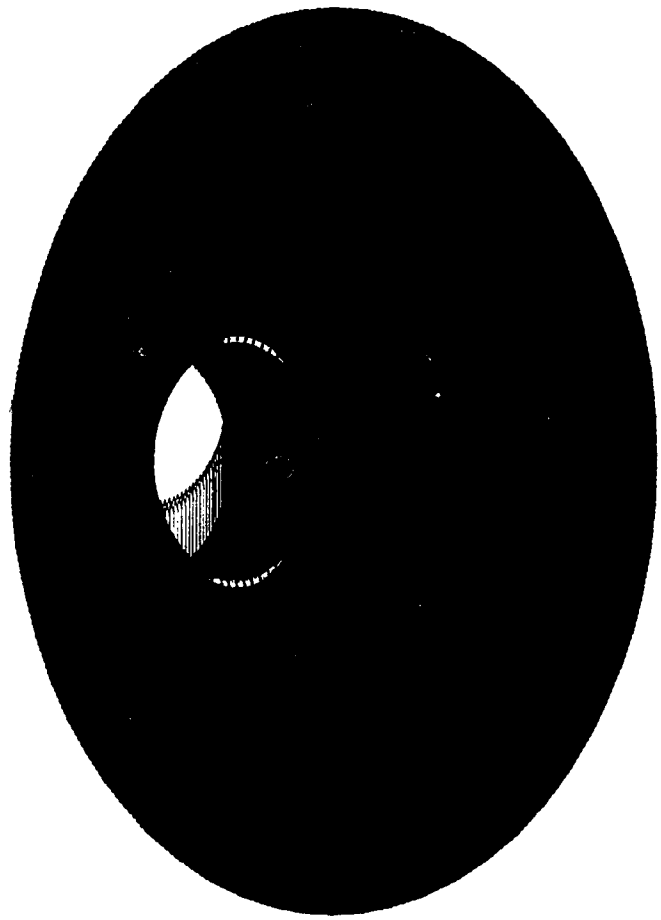


Figure 3-9b Equivalent plastic strain distribution at the plastic limit for Submodel S6 subjected to an inplane shear.



JUN 30 1995  
12:49:15  
PLOT NO. 3



0  
.613E-03  
.001225  
.001838  
.002451  
.003063  
.003676  
.004289  
.004901  
.005514

Figure 3-9c Equivalent plastic strain distribution at the plastic limit for Submodel N7 subjected to an inplane shear.

JUN 30 1995  
12:24:46  
PLOT NO. 3



0  
.567E-02  
.001134  
.001702  
.002269  
.002836  
.003403  
.00397  
.004538  
.005105

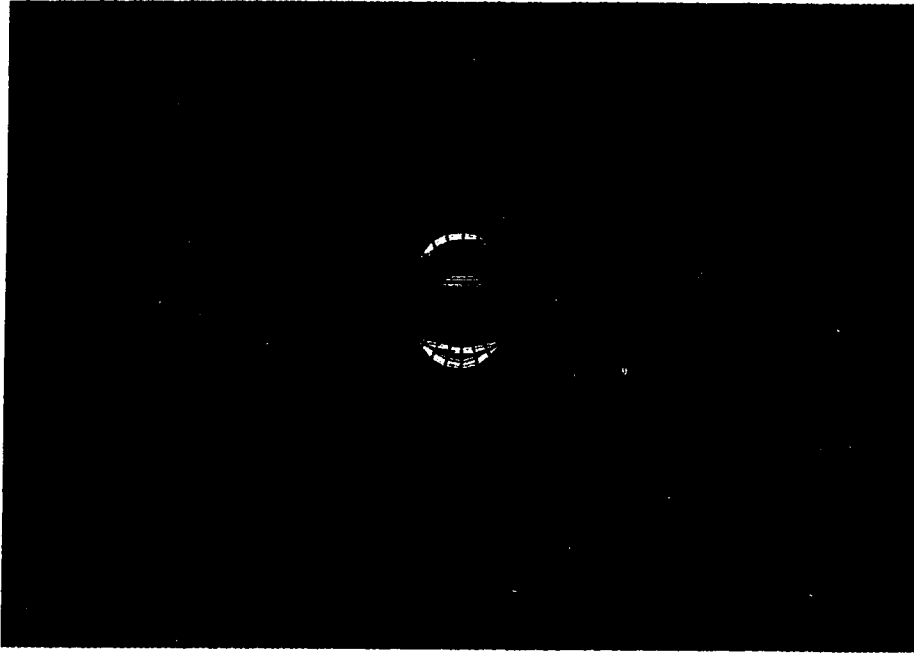


Figure 3-9d Equivalent plastic strain distribution at the plastic limit for Submodel N7 subjected to an outplane shear.

JUN 30 1995  
12:39:21  
PLOT NO. 3



0  
.310E-03  
.620E-03  
.930E-03  
.00124  
.00155  
.001861  
.002171  
.002481  
.002791

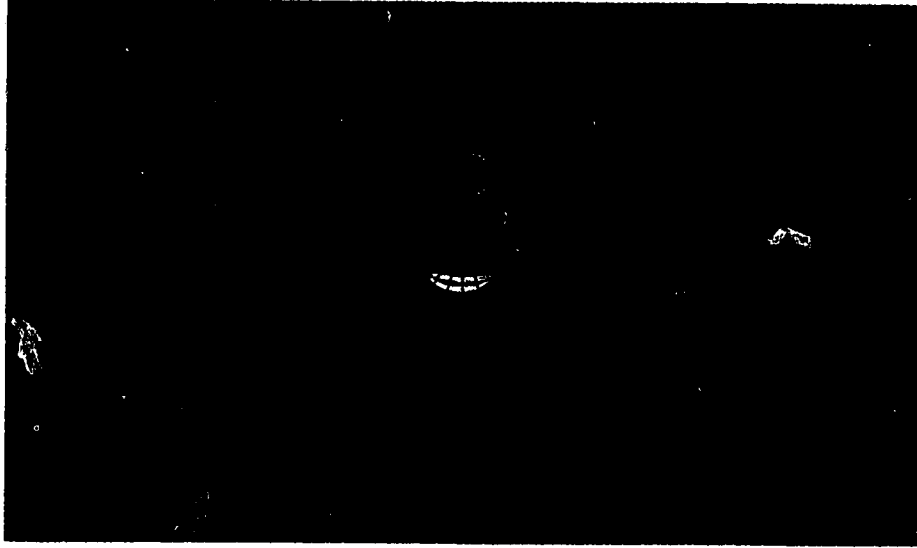


Figure 3-9e Equivalent plastic strain distribution at the plastic limit for Submodel N7 subjected to an inplane moment.

JUN 30 1995  
12:31:35  
PLOT NO. 3



0  
.489E-03  
.937E-03  
.001406  
.001874  
.002343  
.002812  
.00328  
.003749  
.004217

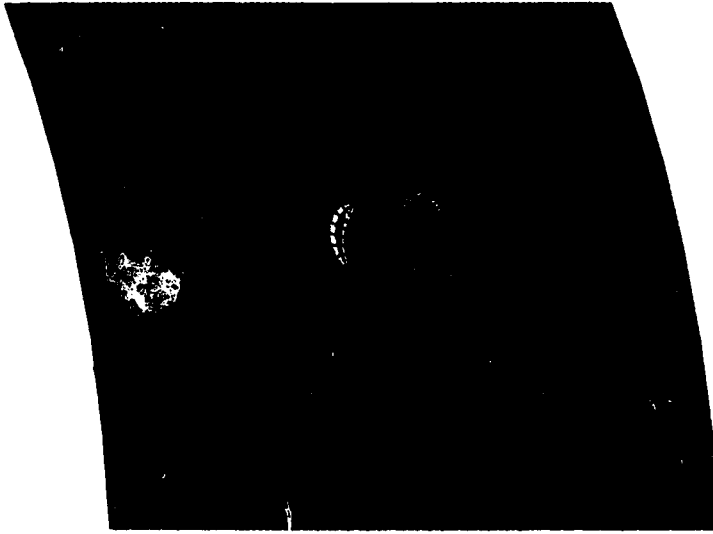


Figure 3-9f Equivalent plastic strain distribution at the plastic limit for Submodel N7 subjected to an outplane moment.

JUN 30 1995  
 12:36:33  
 PLOT NO. 2  
 687.759  
 10026  
 19363  
 28701  
 38039  
 47377  
 56715  
 66052  
 75390  
 84728  
 (psi)

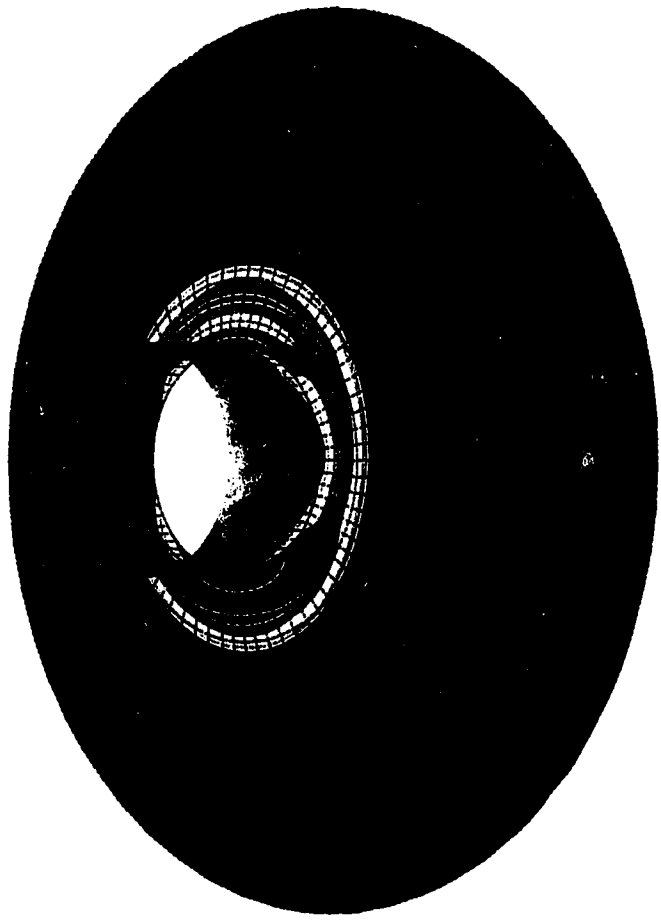


Figure 3-10a Equivalent stress distribution at the plastic limit for Submodel S6 subjected to an outplane moment.

JUN 30 1995  
12:08:40  
PLOT NO. 2

4271
12579
20866
29193
37500
45807
54114
62421
70728
79035

(psi)

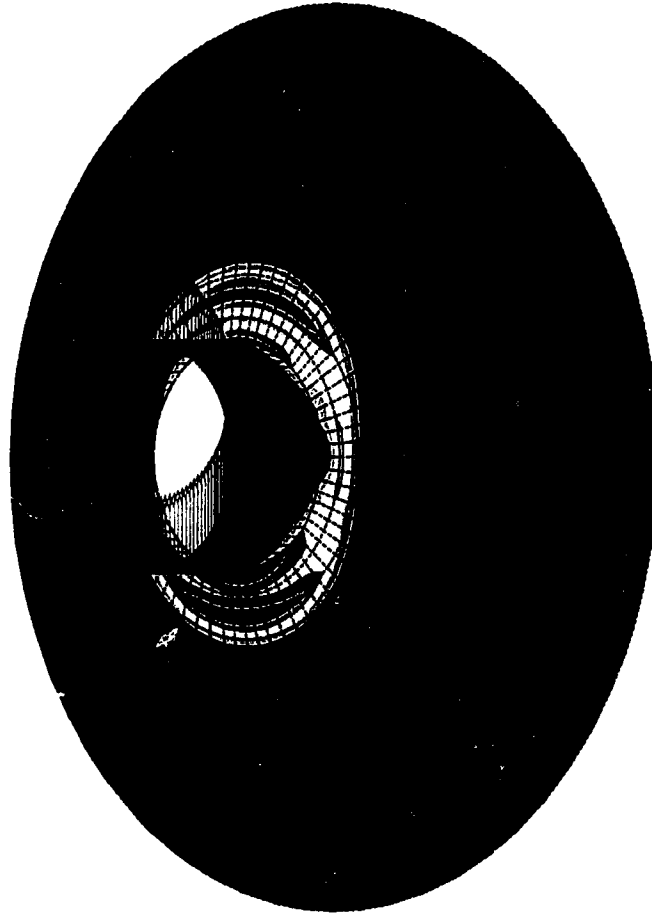


Figure 3-10b Equivalent stress distribution at the plastic limit for Submodel S6 subjected to an inplane shear force.

JUN 30 1995  
12:48:57  
PLOT NO. 2



1861  
11859  
21857  
31855  
41853  
51852  
61850  
71848  
81846  
91844

(psi)

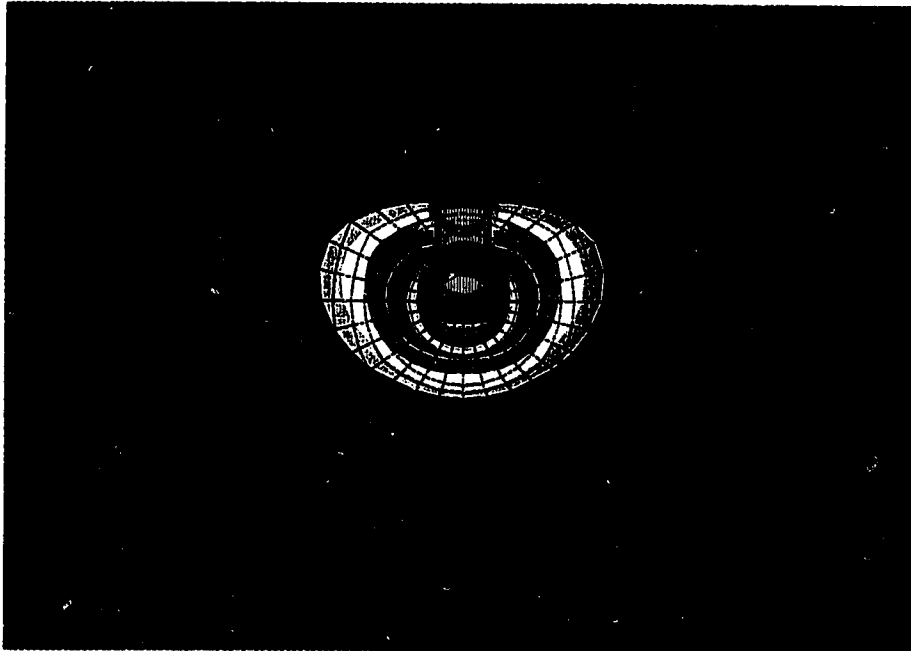


Figure 3-10c Equivalent stress distribution at the plastic limit for Submodel N7 subjected to an inplane shear force.

JUN 30 1995  
 12:24:38  
 PLOT NO. 2

1416  
 11321  
 21225  
 31130  
 41034  
 50939  
 60844  
 70746  
 80653  
 90557

(psi)

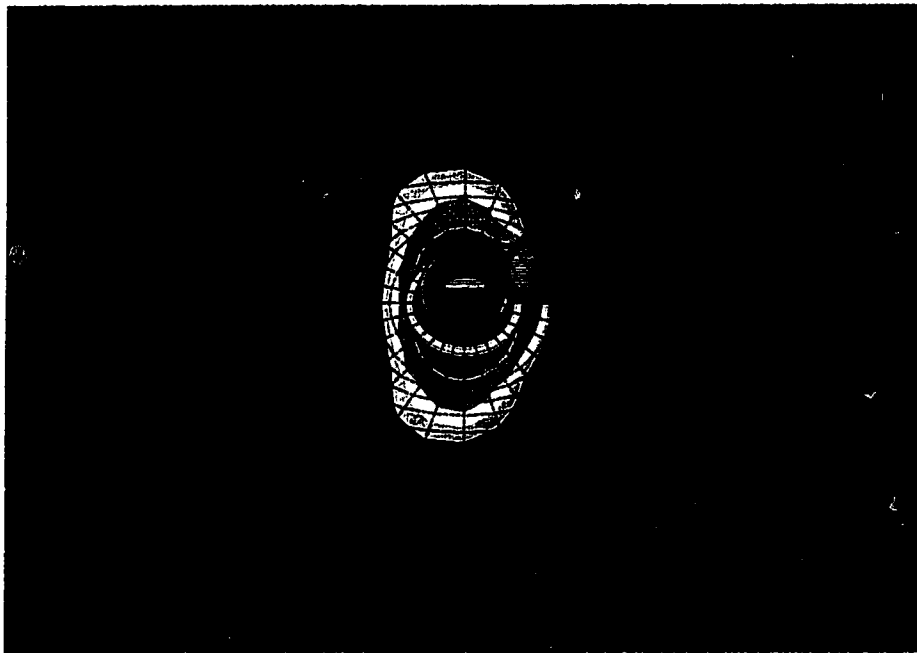


Figure 3-10d Equivalent stress distribution at the plastic limit for Submodel N7 subjected to an outplane shear force.



JUN 30 1995  
 12:39:11  
 PLOT NO. 2  
 1120  
 10238  
 19355  
 28473  
 37591  
 46708  
 55826  
 64943  
 74061  
 83178  
 (psi)

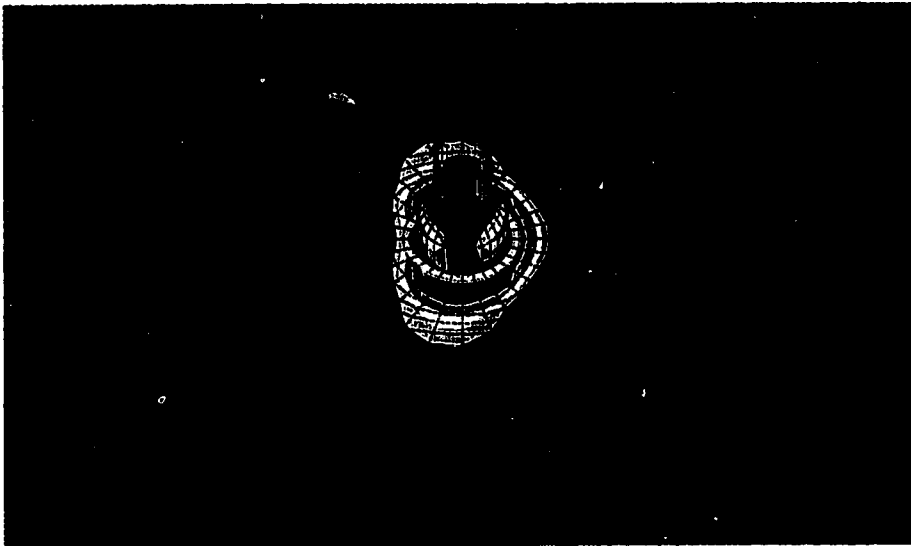


Figure 3-10e Equivalent stress distribution at the plastic limit for Submodel N7 subjected to an inplane moment.

JUN 30 1995  
 12:31:25  
 PLOT NO. 2  
 1702  
 11256  
 20810  
 30364  
 39918  
 49472  
 59026  
 68580  
 78134  
 87688  
 (psi)

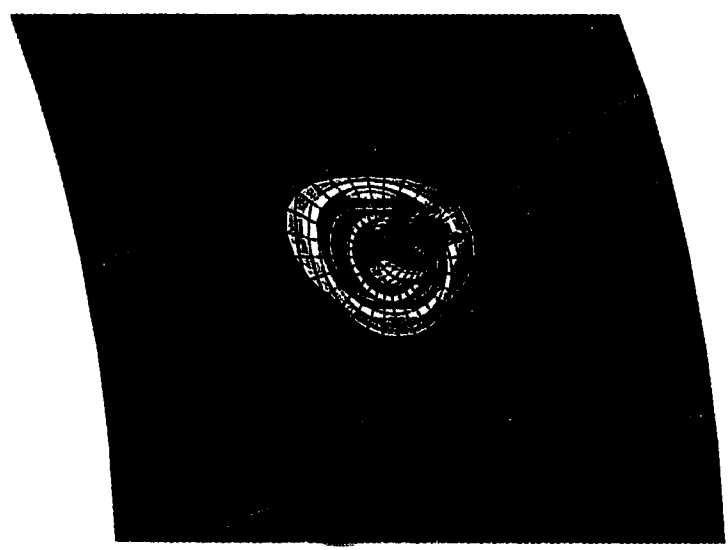


Figure 3-10f Equivalent stress distribution at the plastic limit for Submodel N7 subjected to an outplane moment.

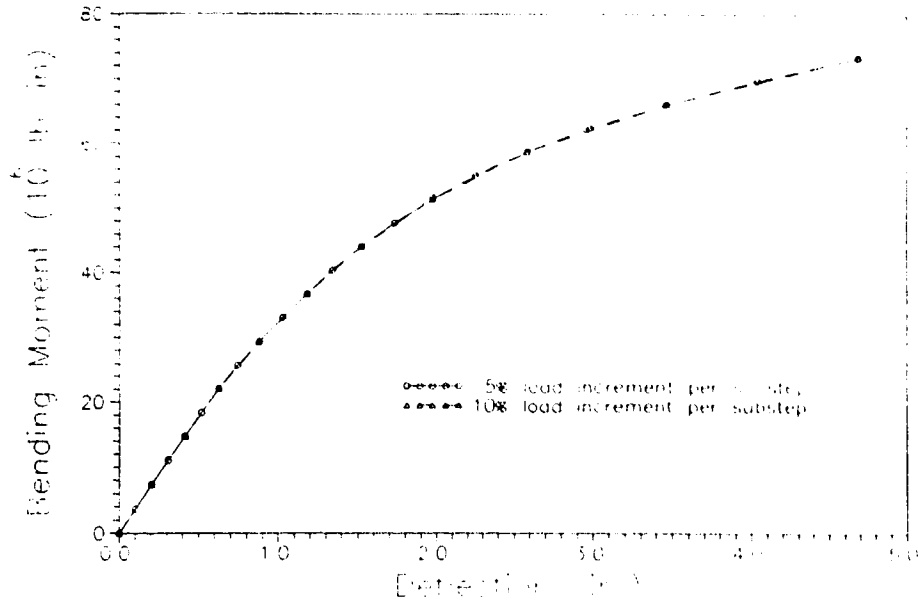


Figure 3-11a Moment versus displacement for Submodel S6 subjected to an outplane moment.

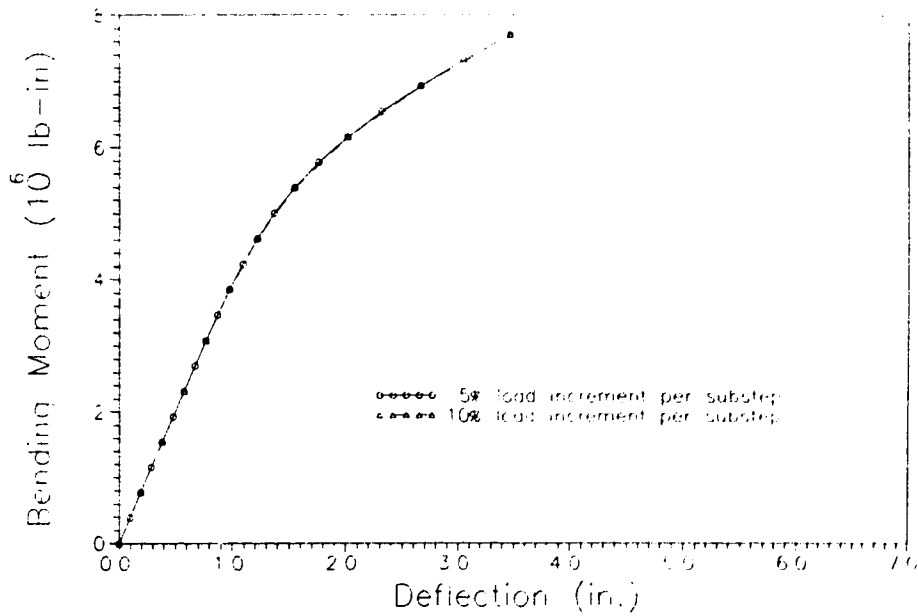


Figure 3-11b Moment versus displacement for Submodel N7 subjected to an outplane moment.

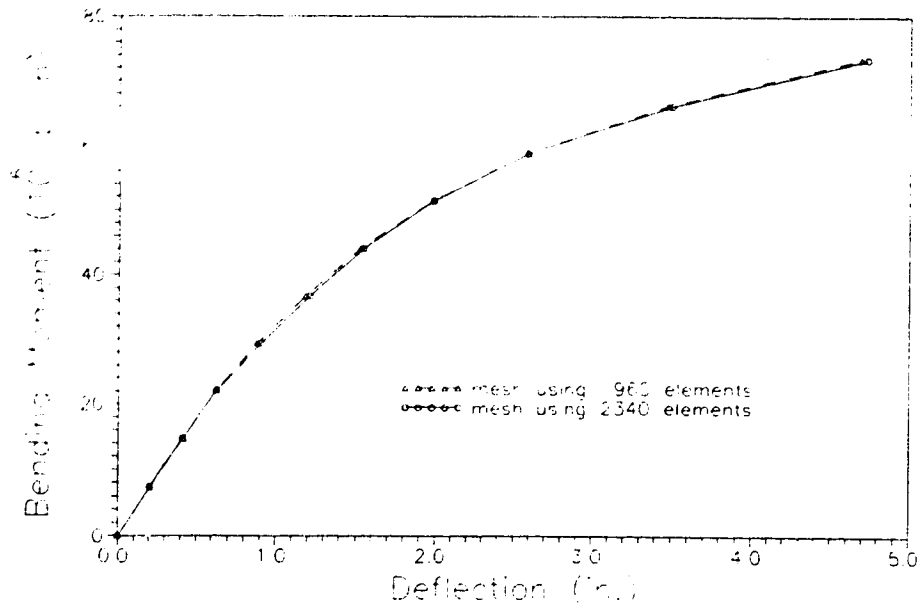


Figure 3-12 Moment versus displacement for Submodel S6 subjected to an outplane moment.

## REFERENCES

- [1] Wichman, K. K., A. G. Hopper, and J. L. Mershon (1979), "Local Stresses in Spherical and Cylindrical Shells due to External Loads", *Welding Research Council Bulletin*, No. 107, December 1968, Revised 1972, Revised 1979.
  
- [2] Hodge, P. G. (1959), Plastic Analysis of Structures, McGraw-Hill Book Company, Inc., NY, p. 270-310.
  
- [3] Gill, S. S. (1964). "The Limit Pressure for a Flush Cylindrical Nozzle in a Spherical Pressure Vessel", *International Journal of Mechanical Sciences*, Vol. 6, p. 105-115.
  
- [4] Dinno, K. S. and S. S. Gill (1965), "The Limit Analysis of a Pressure Vessel Consisting of the Junction of a Cylindrical and Spherical Shell", *International Journal of Mechanical Sciences*, Vol.7, p. 21-42.
  
- [5] Ellyin, F. and A. N. Sherbourne (1965), "Limit Analysis of Axisymmetric Intersecting Shells of Revolution", *Nuclear Structural Engineering*, Vol. 2, p. 86-91.

- [6] Ellyin, F. (1969). "The Effect of Yield Surface on the Limit Pressure of Intersecting Shells", *International Journal of Solids and Structures*, Vol.5, p. 713-725.
- [7] Cloud, R. L. (1965), "The Limit Pressure of Radial Nozzles in Spherical Vessels", *Nuclear Structural Engineering*, Vol. 1, p. 403-413.
- [8] Dinno, K. S. and S. S. Gill (1965), "An Experimental Investigation into the Plastic Behaviour of Flush Nozzles in Spherical Pressure Vessels", *International Journal of Mechanical Sciences*, Vol.7, p. 817-839.
- [9] Ellyin, F. (1969), "Elastic-Plastic Behaviour of Intersecting Shells", *Journal of the Engineering Mechanics Division*, ASCE, Vol. 95, No. EM1, Proc. Paper 6387, p. 69-94.
- [10] Maxwell, R. L., and R. W. Holland (1977), "Collapse Test of a Thin-Walled Cylindrical Pressure Vessel with Radially Attached Nozzle", *Welding Research Council Bulletin*, No. 230, p. 28-38.
- [11] Ellyin, F. (1977), "An Experimental Study of Elasto-Plastic Response of Branch-Pipe Tee Connections Subjected to Internal Pressure, External Couples and Combined Loadings", *Welding Research Council Bulletin*, No. 230, p. 2-27.

- [12] Lefebvre, D. and F. Ellyin (1984), "Cyclic Response and Inelastic Strain Energy in Low Cycle Fatigue", *International Journal of Fatigue*, Vol.6, No. 1, p. 9-15.
- [13] *ASME Code for Pressure Piping, B31, Chemical Plant and Petroleum Refinery Piping*, ASME B31.3-1990 Edition, Paragraph 319.4.4(b), The American Society of Mechanical Engineers, New York, NY, p. 38-39.
- [14] *ASME Boiler and Pressure Vessel Code, Section VIII*, American Society of Mechanical Engineers, New York, N.Y., 1992 Edition, 1994 Addenda.

## **ANALYSIS OF PRESSURIZED LAMINATED CYLINDRICAL SHELLS**

Pressurized laminated cylindrical shells represent internal pressure problems that cannot currently be solved using analytical methods. Chapters 4 and 5 of this thesis present solutions for two pressurized cylindrical shell problems obtained by applying the finite element method.

### **CHAPTER 4**

#### **ANALYSIS OF PRESSURIZED $\pm\theta$ LAMINATED CYLINDRICAL SHELLS**

##### **4.1 INTRODUCTION**

Laminated fibre reinforced plastics (FRP) cylindrical shells offer excellent corrosion resistance and mechanical properties that make them a competitive alternative to conventional materials currently used such areas as piping, downhole tubes, sporting goods, and military applications. The mechanical properties of FRP cylindrical shells are highly dependant on the orientation angles of the individual plies composing the laminate [1], and, therefore, these ply orientation angles must be designed for the specific end application load ratios in order to maximize the economic and structural competitiveness of the laminated shell products. This is difficult, however, since there is not currently available an analytical approach to help designers of composite shells quantitatively determine the ply stacking sequences that would best suit a given set of design conditions.



It was the objective of this investigation to study the effect of lay-up sequence on diametral strain for laminated cylindrical shells subjected to combined internal pressure and axial loading. This was accomplished using the finite element method to model and analyse an axisymmetric cylindrical shell with a general lamina lay-up of  $[+\theta, -\theta, +\theta, +\theta, -\theta, +\theta]$  subjected to internal pressure and axial loading. The strain response of the laminates was then compared to determine the lay-up sequence that produced the smallest radial displacement and to determine the accuracy of the finite element predictions using experimental results as a basis. The stress distribution across the wall thickness of the laminates was also studied for the various laminates.

## 4.2 GEOMETRY

The geometry of the laminated cylindrical shells considered is represented in Figure 4-1. The ratio of the mean radius to the thickness for the shells is 6.6. Thus, the shells can be described as thick cylinders.

The open-end cylindrical shape is formed using wound filaments with the following general angle lay-up:

$$[+\theta, -\theta, +\theta, +\theta, -\theta, +\theta]$$

where  $30^\circ \leq \theta \leq 90^\circ$ . In addition, two other lay-up cases were studied:

$$\cdot [+70^\circ, -70^\circ, 0^\circ, 0^\circ, -70^\circ, +70^\circ]$$

$$\cdot [+90^\circ, -90^\circ, 0^\circ, 0^\circ, -90^\circ, +90^\circ]$$

The material properties used for the analysis are those for E-glass fibres imbedded

in epoxy resin and are as follows [2]:

$$E_1 = 5.66 \times 10^6 \text{ psi} \quad (\text{parallel to fibre direction})$$

$$E_2 = 1.45 \times 10^6 \text{ psi} \quad (\text{transverse to fibre direction})$$

$$\nu_{12} = 0.275$$

$$G_{12} = 580 \times 10^3 \text{ psi}$$

### 4.3 FINITE ELEMENT ANALYSIS

Symmetry was taken advantage of in order to simplify the finite element model required to perform the analysis. Specifically, the axisymmetric geometry and loading required the model to have only one element in the hoop direction with symmetry boundary conditions. Further simplification was possible by assuming that the length of the tube was much greater than its transverse dimensions. This assumption permitted the modelling of a very thin section of the tube. Subsequently, the model made use of only one element in the axial direction with the appropriate plane strain boundary conditions.

Due to the high stress gradients through the thick wall of the cylinder, the model was discretized into 100 elements in the radial direction.

The finite element analysis was performed using the commercial program ANSYS version 5.0. The tube section was modelled using the eight node, three degree of freedom 3-D structural solid element SOLID46 [3]. The SOLID46 element is detailed in Appendix D of this thesis. In making use of this element, it was assumed that the bonding of the ply layers was perfect and that the individual ply layers were homogeneous and anisotropic.

Similar to many metals, the composite tube material is not homogeneous on a microscopic scale. Therefore, this analysis is limited to a macroscopic scale in the discussion of the results. This analysis further assumed that the material response was linearly elastic. The assumption of perfect bonding is acceptable since failure mechanisms such as delamination, matrix cracking, and fibre failure are not being investigated in this thesis. This analysis further assumed that the material response was linear elastic.

The input code to the ANSYS program was written as generally as was practical by defining several initial parameters. Subsequently, modifications to the radius to thickness ratio, ply orientation angles, number of elements, and loading ratio may be easily facilitated if required.

#### **4.4 BIAXIAL LOAD RATIOS**

For the purpose of this investigation, the biaxial load ratio was defined as the ratio of the average hoop stress to the average axial stress.

The stress variation through the thickness and the radial displacement for pure internal pressure loading, biaxial load ratio 1H:0A, and for pure axial loading, biaxial load ratio 0H:1A, were found by solving the finite element model subjected to the respective pressures and axial loads. These results were then appropriately scaled and superimposed to determine the through thickness stress variations and displacements for the additional biaxial load ratios listed in Table 4-1.

## 4.5 RESULTS

The results of this investigation represent a solution for the values of the six independent stress components for a thick-walled pressure vessel, as well as a solution for the radial displacement, for the general  $[+\theta, -\theta, +\theta, +\theta, -\theta, +\theta]$  ply stacking sequence.

Figures 4-2a to 4-2i are plots for each load ratio listed in Table 4-1, respectively, of the radial displacement at the inside radius of the shell, normalized by the inside radius, as a function of the ply stacking sequence. The lay-up sequence angle  $\theta$  which gives the minimum radial displacement for each of the biaxial load ratios considered was determined from these figures and is plotted in Figure 4-3 against the respective biaxial load ratio. Figure 4-3 summarizes the ply stacking angle  $\theta$  for the  $[+\theta, -\theta, +\theta, +\theta, -\theta, +\theta]$  lay-up which minimizes the radial displacement response of the composite shells considered.

Figures 4-4a to 4-4d are plots of the variation of the hoop, axial, radial, and in-plane shear stresses, respectively, for the various laminates subjected to a 2:1 biaxial load ratio. This biaxial load ratio is of particular interest since it is consistent with that developed in pressure vessels. The two remaining independent stress components are the transverse shear components  $\sigma_{r\theta}$  and  $\sigma_{rz}$ . The results for both of these components are identically zero over the entire  $r$ -domain.

#### **4.6 EFFECT OF ELEMENT SIZE**

Since the input code was written in a general manner, the effect of the size of the elements was easily checked. To accomplish this, the number of elements specified in the input code to be used for the analysis was increased by an order of magnitude, to 1000 elements. Increasing the mesh density by an order of magnitude produced no noticeable change in the stress distribution. Thus, the mesh density achieved using 100 elements was considered adequate for this analysis.

#### **4.7 COMPARISON TO PHYSICAL EXPERIMENTS**

The finite element results from the  $[+\theta, -\theta, +\theta, +\theta, -\theta, +\theta]$  were compared against the results of physical experiments found in the literature. This was performed in order to test the accuracy of the finite element results.

Displacement results from physical experiments found in the literature [4] performed using commercially manufactured shells with a mean radius to thickness ratio of 6.6 and a filament winding angle of  $\pm 55^\circ$  are superimposed on the finite element results from this analysis for the biaxial load ratios 0H:1A, 1H:1A, 2H:1A, and 1H:0A in Figures 4-2a, 4-2d, 4-2f, and 4-2i, respectively. The load-displacement response of the shells tested in the literature was nonlinear for some ratios of biaxial loading. Since the finite element analysis performed assumes a linear elastic response, the tangent to the elastic response reported in the literature was used to perform the comparison presented

herein.

The material used in the physical experiments was glass fibre reinforced epoxy, which matches the description of the material used in the finite element model. However, the literature does not report the material properties of the individual lamina layers of the tested shells nor the material properties of the glass fibres or the epoxy used to manufacture the shells. Therefore, the material properties used in the finite element analysis cannot be compared directly to the material properties used in the physical experiments. However, the finite element results for the  $\pm 55^\circ$  winding angle compare well to the results from the physical experiment. The accuracy achieved for each load case is listed in Table 4-2.

#### 4.8 DISCUSSION

The ply stacking angle  $\theta$  for the general lamina stacking sequence  $[+\theta, -\theta, +\theta, +\theta, -\theta, +\theta]$  that yields the smallest radial displacement was determined. This data is useful in several applications. One such application is the design of composite tubing and piping that is joined using threaded connection. In this type of connection, radial displacement due to internal pressure can compromise the seal at joints. Biaxial load ratios in this type of application range from 1H:0A, such as for a long horizontal pipe, to 0H:1A, such as in a tall vertical standing pipe. A second such application is barrel design for projectiles, such as composite rifle barrels and rocket tubes. In such an application as this, it is critical that the radial displacement of the barrel be as small as

possible in order to prevent the firing gases from leaking past the projectile before the projectile has cleared the muzzle of the barrel. It is evident from Figure 4-3 that for a lamina sequence such as  $[+\theta, -\theta, +\theta, +\theta, -\theta, +\theta]$ , the ply stacking angle  $\theta$  must be selected for the particular load ratio biaxiality anticipated in a products end use.

Commercially manufactured composite cylindrical shells are often produced using a continuous method such as filament winding. In continuous methods such as filament winding it is difficult to achieve high winding angles, such as  $90^\circ$ . Figures 4-2e to 4-2h demonstrate the trend that for hoop stress dominant biaxial load ratios, no significant reduction in radial displacement is achieved by increasing the winding angle  $\theta$  above  $70^\circ$ . Winding angles of  $70^\circ$  can be produced continuously using a filament winding technique.

The hoop and axial stress variation are plotted in Figures 4-4a and 4-4b, respectively, for the two lay-up sequences that included simulated zero degree layers, as well as for the  $[+\theta, -\theta, +\theta, +\theta, -\theta, +\theta]$  lay-up sequence for the 2H:1A biaxial load ratio. Since these two components of stress are of significantly greater magnitude than the radial and shear components, plotted in Figures 4-4c and 4-4d, they are more likely to influence tube strength. The variation of hoop and axial stress variation for the  $[+\theta, -\theta, +\theta, +\theta, -\theta, +\theta]$  lay-up is very similar to that which would be expected for an isotropic material. That is, these two components of stress vary in a smooth manner along the radial direction, even across the layer boundaries.

In the two cases that included the simulated zero degree layers, however, the stress variation significantly step changes at the boundary of the zero degree layer. This trend suggests that describing the hoop or axial stress components of a laminate with zero degree

layers using the calculated average hoop stress or calculated average axial stress, as is conventional in the case of isotropic materials, does not give a good indication of the stress through the section. That is, the maximum stress is significantly higher than the average stress.

Average stress is a good indicator of the stress condition for the  $[+\theta, -\theta, +\theta, +\theta, -\theta, +\theta]$  lay-up sequence since the maximum stress developed is very close to the calculated average stress.

#### 4.9 CONCLUSIONS

It was the goal of this study to determine the lamina lay-up sequence effect on the diametral strain of thick laminated cylindrical shells subjected to combined axial loading and internal pressure. Axisymmetric shells with a lamina lay of  $[+70^\circ, -70^\circ, 0^\circ, 0^\circ, -70^\circ, +70^\circ]$ ,  $[+90^\circ, -90^\circ, 0^\circ, 0^\circ, -90^\circ, +90^\circ]$ , and a general lamina lay-up of  $[+\theta, -\theta, +\theta, +\theta, -\theta, +\theta]$  subjected to internal pressure and axial loading were modelled using the finite element method, and a stress/strain analysis of these models was performed using the ANSYS program. The results from this analysis were compared to experimental results found in the literature.

The results of the finite element analysis performed lead to the following conclusions:

- I. It was demonstrated that the finite element models developed for the laminated cylindrical shells can be used to predict stress/strain response of



such tubes subjected to combined internal pressure and axial loading.

- II. It was shown that the lamina lay-up sequence for the least radial displacement varies with the biaxial ratio of internal pressure to axial loading.
- III. No significant reduction in radial displacement is achieved by increasing the ply stacking angle  $\theta$  above  $70^\circ$  for the lay-up  $[+\theta, -\theta, +\theta, +\theta, -\theta, +\theta]$  and biaxial load ratios with an average hoop stress greater than the average axial stress.
- IV. The finite element predictions for radial displacement were compared to results from physical experiments and found to agree to within 25%.

**Table 4-1**

**Biaxial Load Ratios Considered**

Hoop Stress : Axial Stress
1:0
4:1
3:1
2:1
3:2
1:1
1:2
1:3
0:1

**Table 4-2**

**Accuracy of  $\pm 55^\circ$  Finite Element Results Based on Physical Experiments [4].**

Biaxial Load Ratio Hoop : Axial	Finite Element Prediction (u/a)	Physically Measured Response <sup>1</sup> (u/a)	Accuracy <sup>2</sup> (%)
0:1	-0.000901	-0.00091	-1
1:1	0.000440	0.00040	10
2:1	0.00175	0.0014	25
1:0	0.00265	0.0024	10

---

<sup>1</sup> In the case of nonlinear load-displacement response, the reported tangent to the elastic response displacement is listed here.

<sup>2</sup> Accuracy =  $\frac{\text{finite element response} - \text{experimental response}}{\text{experimental response}} \times 100\%$

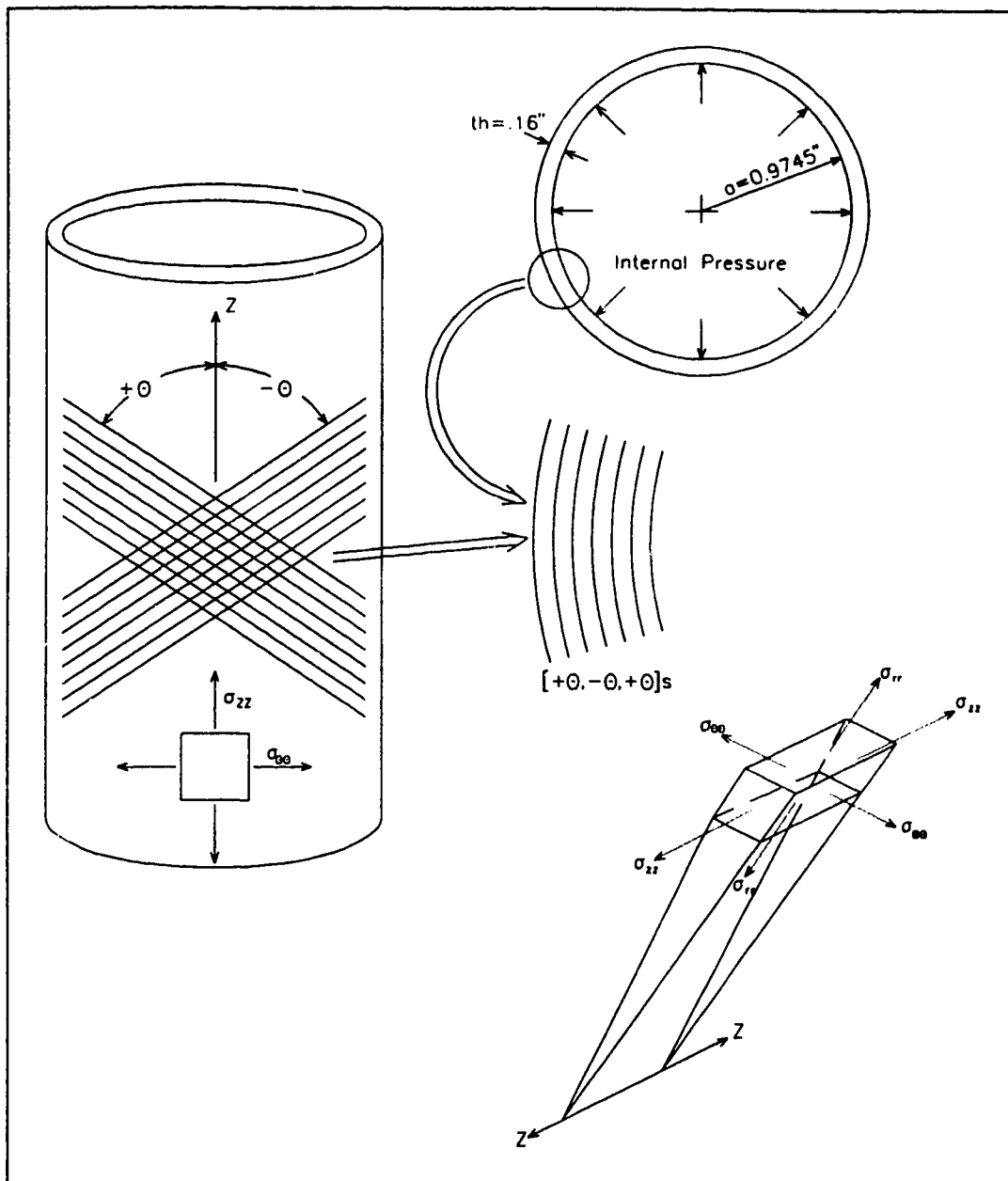


Figure 4-1 Geometry of the Finite Element Analysis Model

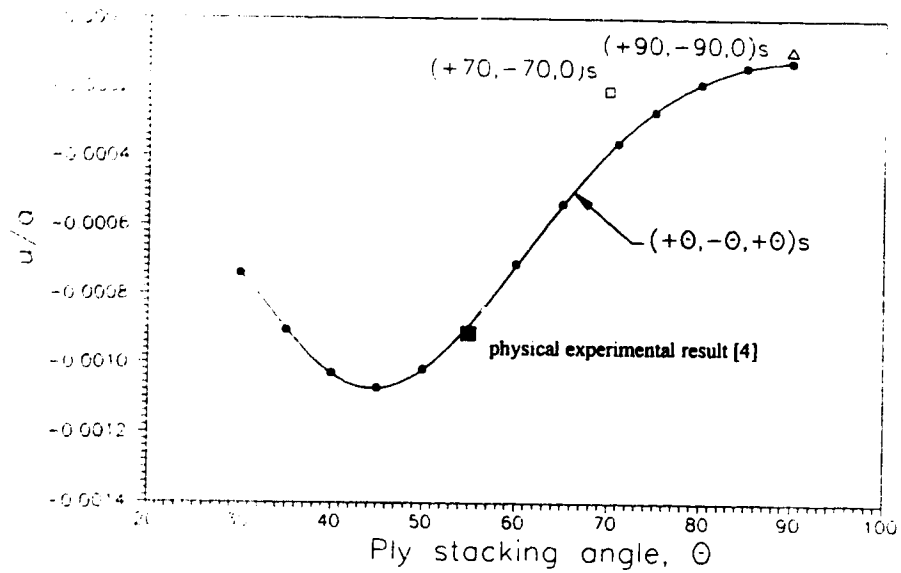


Figure 4-2a Radial displacement response versus stacking angle  $\theta$  for a biaxial load ratio of 0H:1A. The radial displacements for  $(+70^\circ, -70^\circ, 0)$ , and  $(+90^\circ, -90^\circ, 0)$ , are also shown, as well as an experimental result for  $\pm 55^\circ$ .

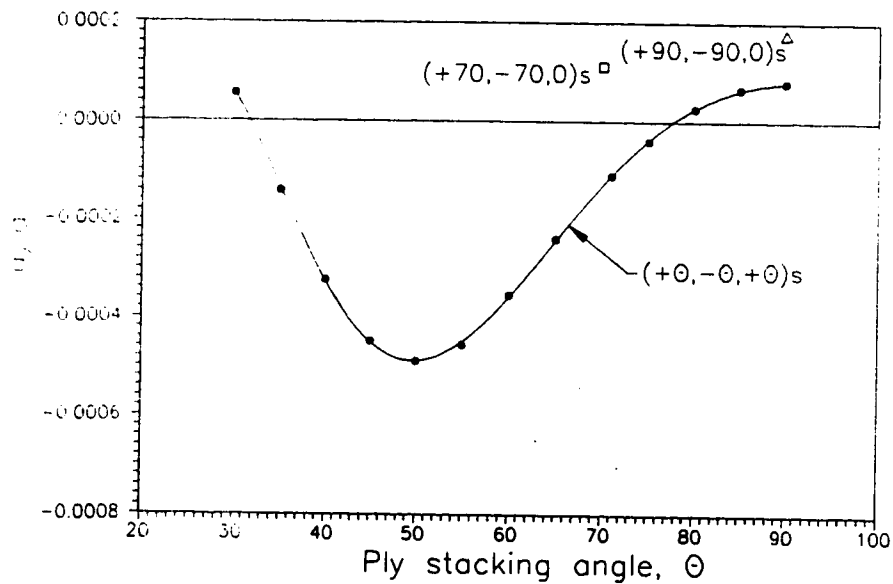


Figure 4-2b Radial displacement response versus stacking angle  $\theta$  for a biaxial load ratio of 1H:3A. The radial displacements for  $(+70^\circ, -70^\circ, 0)$ , and  $(+90^\circ, -90^\circ, 0)$ , are also shown.

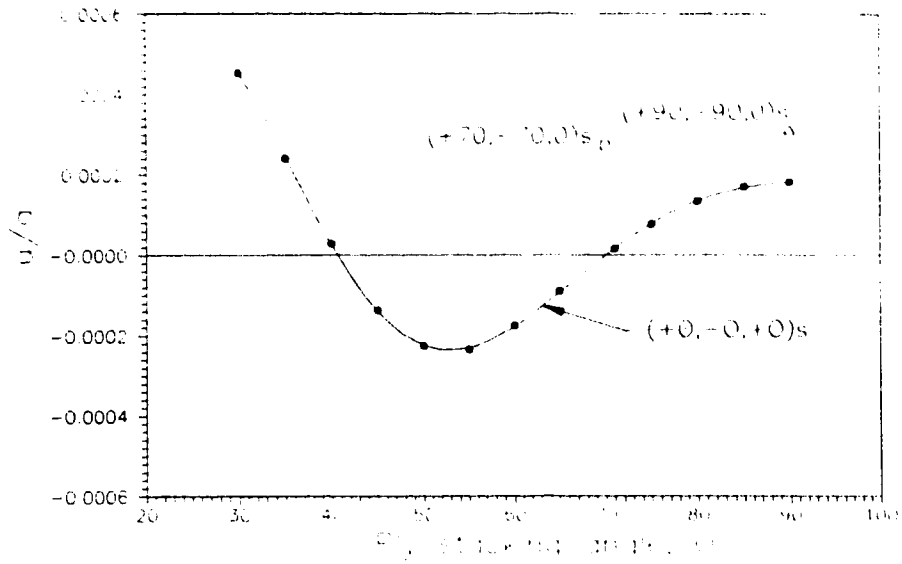


Figure 4-2c Radial displacement response versus stacking angle  $\theta$  for a biaxial load ratio of 1H:2A. The radial displacements for  $(+70^\circ, -70^\circ, 0)$ , and  $(+90^\circ, -90^\circ, 0)$ , are also shown.

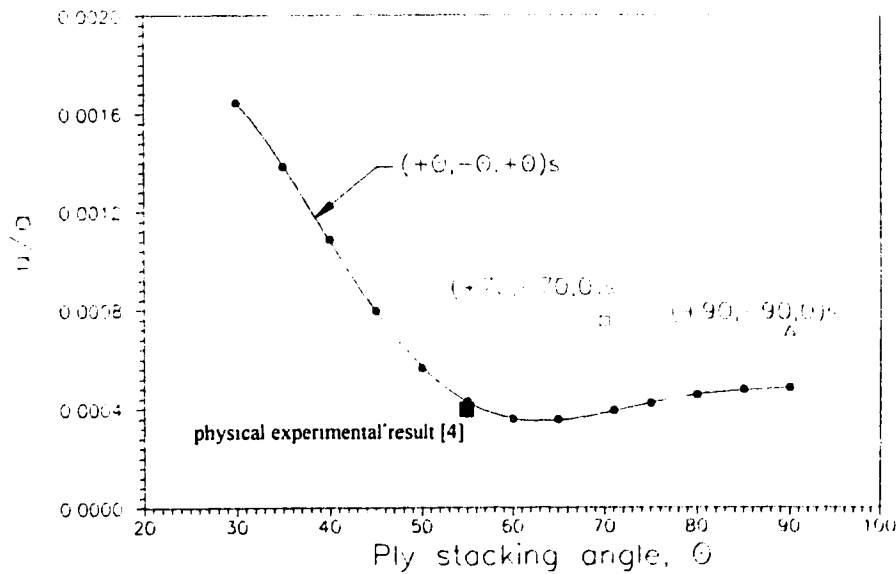


Figure 4-2d Radial displacement response versus stacking angle  $\theta$  for a biaxial load ratio of 1H:1A. The radial displacements for  $(+70^\circ, -70^\circ, 0)$ , and  $(+90^\circ, -90^\circ, 0)$ , are also shown, as well as an experimental result for  $\pm 55^\circ$ .

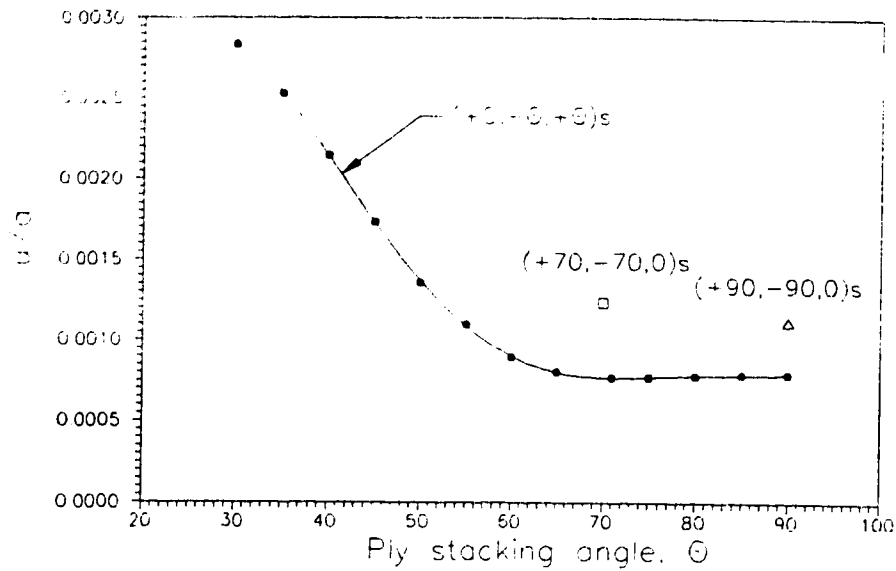


Figure 4-2e Radial displacement response versus stacking angle  $\theta$  for a biaxial load ratio of 3H:2A. The radial displacements for  $(+70^\circ, -70^\circ, 0)_s$  and  $(+90^\circ, -90^\circ, 0)_s$  are also shown.

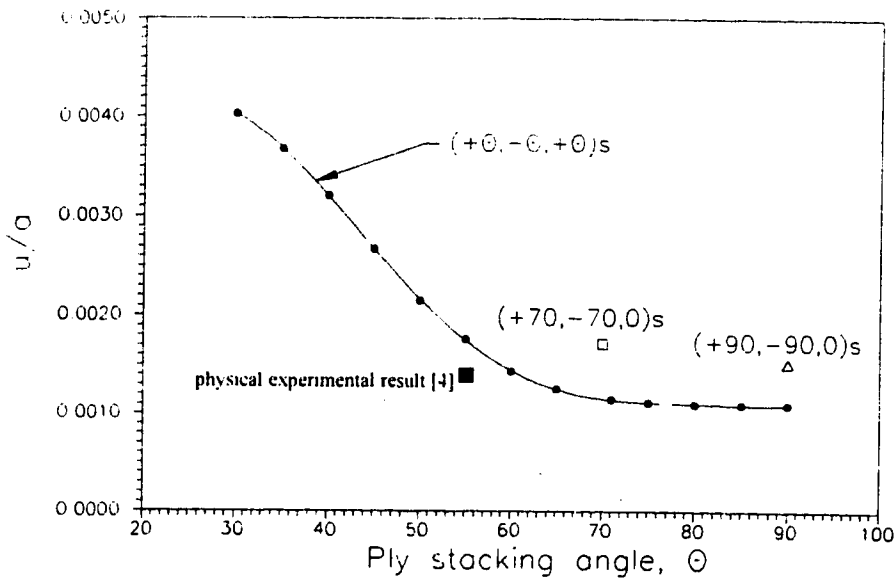


Figure 4-2f Radial displacement response versus stacking angle  $\theta$  for a biaxial load ratio of 2H:1A. The radial displacements for  $(+70^\circ, -70^\circ, 0)_s$  and  $(+90^\circ, -90^\circ, 0)_s$  are also shown, as well as an experimental result for  $\pm 55^\circ$ .

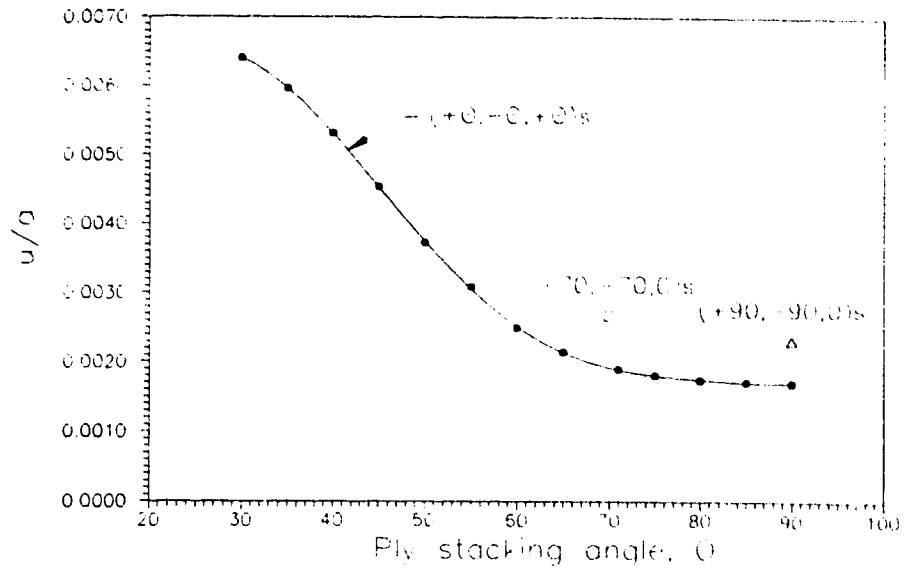


Figure 4-2g Radial displacement response versus stacking angle  $\theta$  for a biaxial load ratio of 3H:1A. The radial displacements for  $(+70^\circ, -70^\circ, 0)_s$  and  $(+90^\circ, -90^\circ, 0)_s$  are also shown.

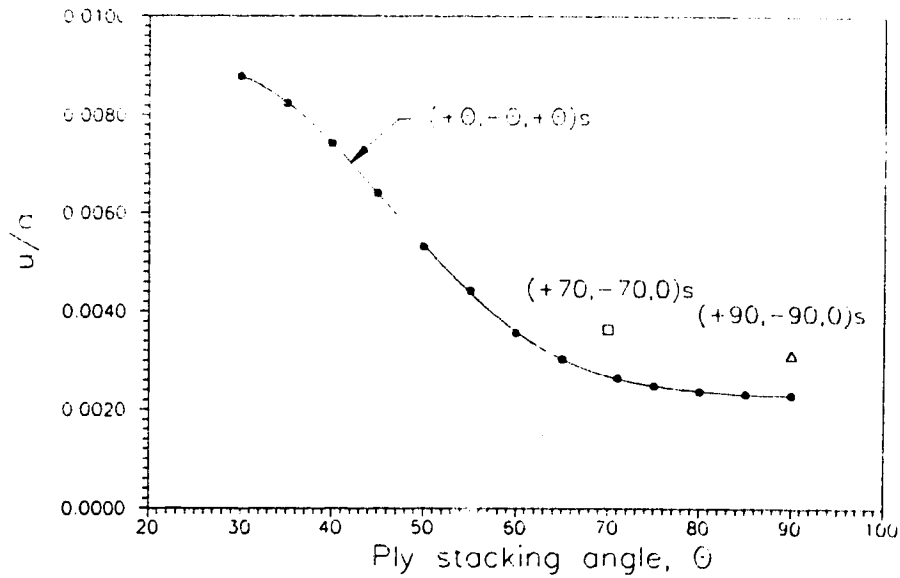


Figure 4-2h Radial displacement response versus stacking angle  $\theta$  for a biaxial load ratio of 4H:1A. The radial displacements for  $(+70^\circ, -70^\circ, 0)_s$  and  $(+90^\circ, -90^\circ, 0)_s$  are also shown.

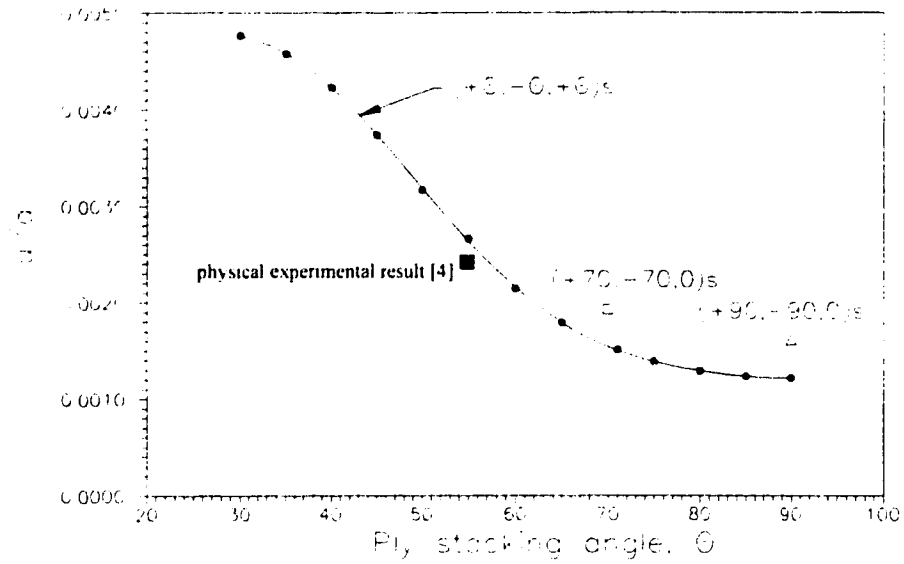


Figure 4-2i Radial displacement response versus stacking angle  $\theta$  for a biaxial load ratio of 1H:0A. The radial displacements for  $(+70^\circ, -70^\circ, 0)_s$  and  $(+90^\circ, -90^\circ, 0)_s$  are also shown, as well as an experimental result for  $\pm 55^\circ$ .

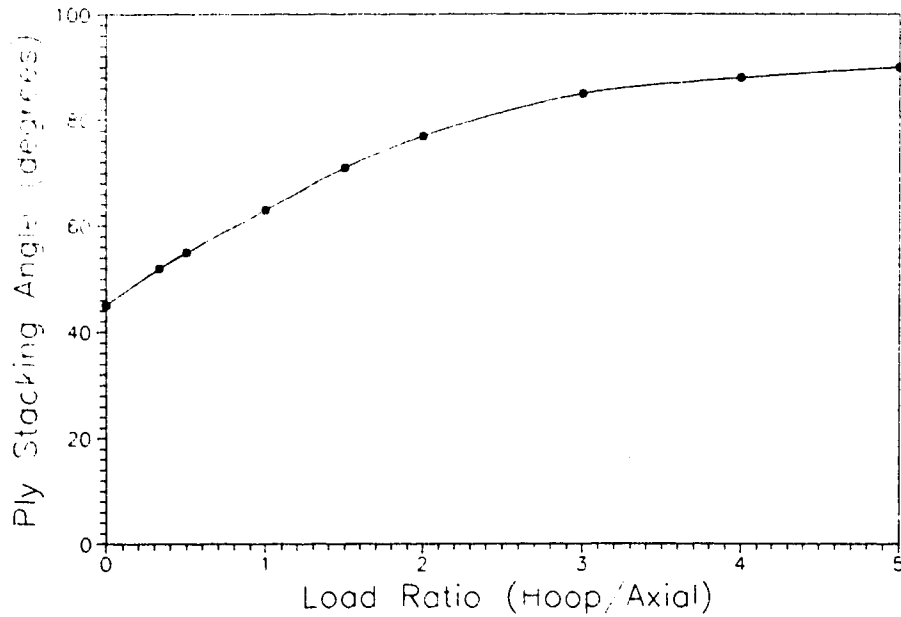


Figure 4-3 Stacking angle for minimum radial displacement versus biaxial load ratio.



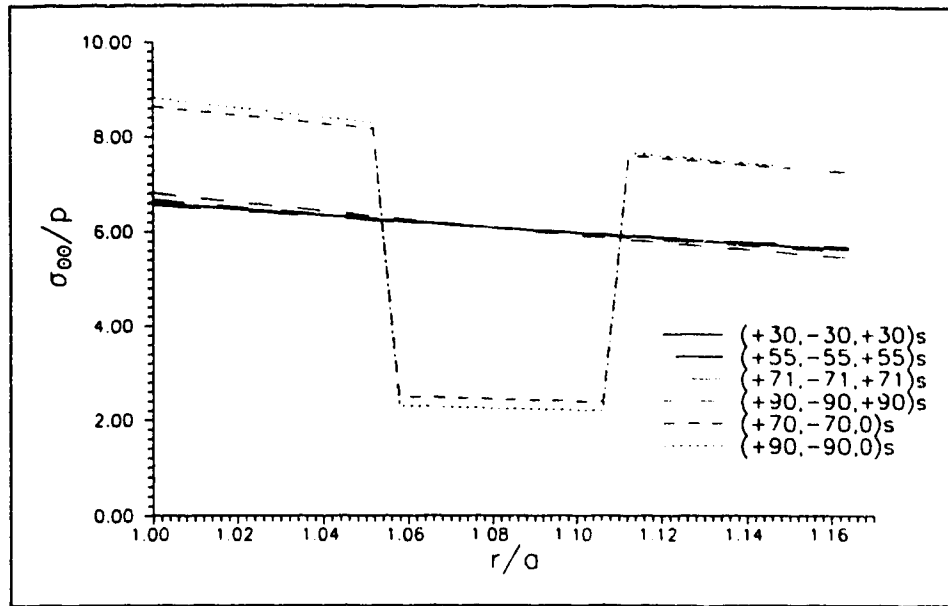


Figure 4-4a Variation of hoop stress through the thickness for a biaxial load ratio of 2H:1A.

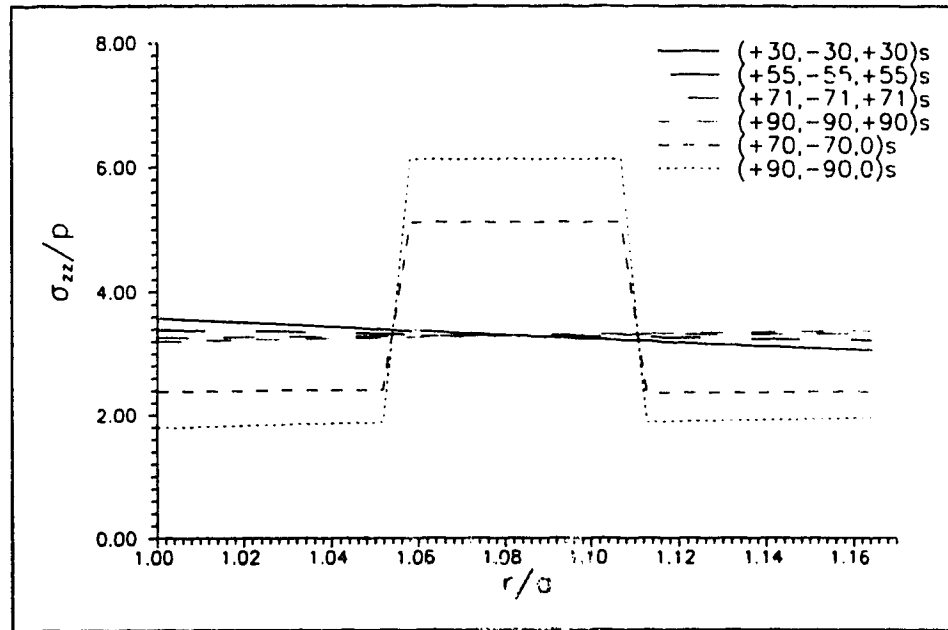


Figure 4-4b Variation of axial stress through the thickness for a biaxial load ratio of 2H:1A.

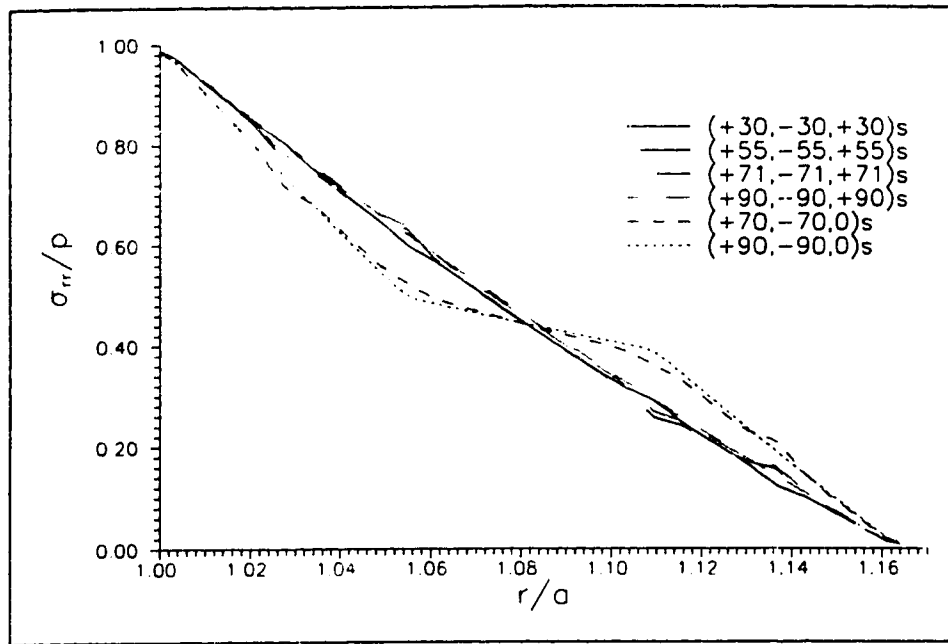


Figure 4-4c Variation of radial stress through the thickness for a biaxial load ratio of 2H:1A.

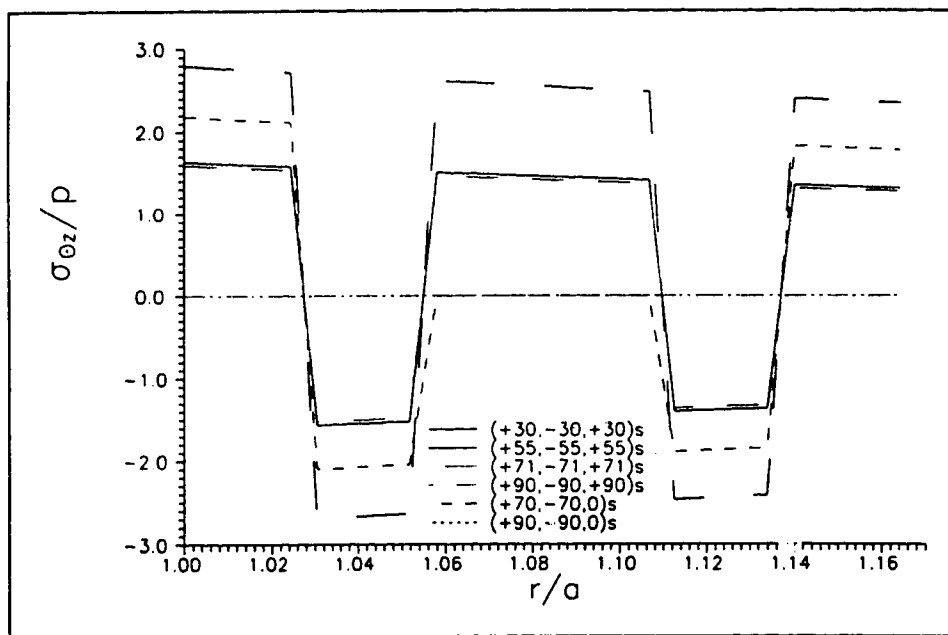


Figure 4-4d Variation of in-plane shear stress through the thickness for a biaxial load ratio of 2H:1A.

## REFERENCES

- [1] Carroll, M., F. Ellyin, and D. Kujawski (1995), "Stacking Sequence Effect on Tensile and Fatigue Strength of Symmetric Laminates", *Polymers and Polymer Composites*, Vol. 3, No. 1, p. 1-10.
  
- [2] Engineered Materials Handbook. v.1 Composites. ASM INTERNATIONAL. May 1988. p.144.
  
- [3] DeSalvo, G. J., and R. W. Gorman (1989), ANSYS Engineering Analysis System User's Manual, Swanson Analysis Systems, Inc., Pennsylvania, USA, p. 4.46.1-4.46.8.
  
- [4] Carroll, M., F. Ellyin, D. Kujawski, and A.S. Chiu (1995), "The Rate-Dependent Behaviour of  $\pm 55^\circ$  Filament-Wound Glass-Fibre/Epoxy Tubes Under Biaxial Loading", *Composite Science and Technology*, No. 55, p. 391-403.

**CHAPTER 5**  
**ANALYSIS OF PRESSURIZED MULTI-DIRECTIONAL**  
**LAMINATED CYLINDRICAL SHELLS**

**5.1 INTRODUCTION**

Due to the complex behaviour of multi-directional composite cylindrical shells, there is not currently available a complete analytical solution of the stress/strain response of such shells subjected to combined internal pressure and axial loading. The purpose of this investigation was to provide the thick cylinder stress/strain distribution for multi-directional fibre reinforced plastics cylindrical shells subjected to various ratios of biaxial loading.

This was accomplished using the finite element method to model and analyse an axisymmetric cylindrical shell with a lamina lay-up of [ $\pm 70^\circ, \pm 45^\circ, \pm 45^\circ, -70^\circ, 0^\circ, -45^\circ, \pm 45^\circ, \pm 45^\circ, \pm 45^\circ, \pm 45^\circ$ ] subjected to internal pressure and axial loading. The resulting stress and strain variations through the wall thickness were then plotted. The strain response of the shells predicted was shown to compare well with the results from physical experiments.

## 5.2 GEOMETRY

The geometry of the shells considered is represented in Figure 5-1. The open-end cylindrical shape is formed using wound filaments with the following angle lay-up:

$$[\pm 70^\circ, \pm 45^\circ, \pm 45^\circ, -70^\circ, 0^\circ, -45^\circ, \pm 45^\circ, \pm 45^\circ, \pm 45^\circ, \pm 45^\circ]$$

The  $70^\circ$  layer and the  $45^\circ$  layer are at the outer diameter and the inner diameter, respectively. This stacking sequence was selected as it is consistent with a commercially manufactured multi-directional laminated pipe.

The material properties used for the analysis are those for E-glass fibres imbedded in epoxy resin and are as follows [1]:

$$E_1 = 5.66 \times 10^6 \text{ psi} \quad (\text{parallel to fibre direction})$$

$$E_2 = 1.45 \times 10^6 \text{ psi} \quad (\text{transverse to fibre direction})$$

$$\nu_{12} = 0.275$$

$$G_{12} = 580 \times 10^3 \text{ psi}$$

These material properties are the same as those used in the analysis presented in Chapter 4.

## 5.3 FINITE ELEMENT MODEL

The input code to the ANSYS program written to perform the analysis presented in Chapter 4 was written in such a way that the number of layers, the number of elements, the ply orientation angles, the diameter, and the thickness are defined as variable

parameters. For this investigation the variable parameters were defined in accordance with the geometry shown in Figure 5-1.

Boundary conditions appropriate for plain strain in the longitudinal direction were prescribed to the model, and axisymmetric boundary conditions were prescribed in the circumferential direction.

The ply orientation angles were modelled by orientating the elastic modulus  $E_1$  parallel to the orientation angle of the ply.

#### **5.4 BIAxIAL LOAD RATIOS**

For the purpose of this investigation, the biaxial load ratio was defined as the ratio of the average hoop stress to the average axial stress. For example, the biaxial load ratio consistent with that found in pressure vessels would be 2 Hoop to 1 Axial, or 2H:1A.

The stress and strain variation through the thickness for pure internal pressure loading, load ratio 1H:0A, and for pure axial loading, load ratio 0H:1A, were found by solving the finite element model subjected to only internal pressure or axial load, respectively. These results were then appropriately scaled and superimposed to determine the through thickness stress and strain variation for the additional biaxial load ratios of 2H:1A and 1H:1A.

The biaxial loads ratios considered in this investigation are summarized in Table 5-1.

## 5.5 RESULTS

The results of this investigation represent a solution for the six independent stress and strain components for a thick-walled pressure vessel. Further, these resulting components were used to calculate the equivalent stresses and strains for each of the biaxial load ratios considered.

A 'Von Mises' type equivalent stress,  $\sigma_{eq}$ , was calculated for each biaxial load ratio according to the following equation with  $\sigma_{r\theta}$  and  $\sigma_{zr}$  assumed to be equal to zero:

$$\sigma_{eqv} = 1/\sqrt{2} [(\sigma_{rr} - \sigma_{\theta\theta})^2 + (\sigma_{\theta\theta} - \sigma_{zz})^2 + (\sigma_{zz} - \sigma_{rr})^2 + 6\sigma_{t\theta}^2]^{1/2}$$

The equivalent stress,  $\sigma_{eqv}$ , represents the proximity of the material to yield, and the assumption that  $\sigma_{r\theta}$  and  $\sigma_{zr}$  are equal to zero is consistent with the axisymmetric geometry and axisymmetric loading. Details regarding the Von Mises type equivalent stress can be found in any strength of materials text [2].

Figures 5-2a to 5-2d are plots of the variation of the hoop, axial, radial, and in-plane shear stresses for the multi-directional shells subjected to each of the biaxial load ratios listed in Table 5-1, respectively. The two transverse shear components  $\sigma_{r\theta}$  and  $\sigma_{zr}$  are not plotted in Figures 5-2a to 5-2d because the solution for both of these components was found to be zero through the entire wall thickness.

Figures 5-3a to 5-3d are plots of the variation of the hoop, axial, radial, and in-plane shear strains for the multi-directional shells subjected to each of the biaxial load ratios listed in Table 5-1, respectively. The transverse shear strain components  $\epsilon_{r\theta}$  and

$\epsilon_r$  are not plotted in Figures 5-3a to 5-3d because they were found to be equal to zero throughout the thickness.

Several observations can be made upon comparison of the stress and strain distributions for each load ratio. As can be seen in Figure 5-3a to 5-3d, the strain variation through the wall thickness is nearly constant and very smooth. The stress variations plotted in Figures 5-2a to 5-2d, however, are strongly dependent on the orientation of the individual plies. The reason for this result is that the stiffness of each individual ply along the axial and circumferential directions of the shell is dependent on the ply orientation angle, and since the strain is constant in the axial direction and nearly constant in the circumferential directions of the cylinder, the stress varies with the ply orientation angle.

In Figures 5-2a to 5-2d this effect is particularly evident at the inside and outside boundaries of the  $0^\circ$  layer with non-zero axial load, biaxial load ratios 1H:1A and 0H:1A. It is also evident to a lesser extent at the boundaries of the  $70^\circ$  layers for the 1H:0A load ratio, or pure internal pressure.

The combination of the  $0^\circ$  layer and the  $70^\circ$  layers suggests that the multi-directional composite cylindrical shell would be effective at carrying internal pressure and axial loads, both in combination and individually.



## **5.6 COMPARISON TO PHYSICAL EXPERIMENTS**

The results of this analysis were compared to results from physical experiments found in the literature in order to determine the accuracy of the finite element predictions presented herein.

The circumferential and axial strains measured in physical experiments [3] are superimposed over the strains predicted by this analysis in Figures 5-3a to 5-3d. These experiments were performed using multi-directional glass fibre reinforced epoxy shells with similar geometry to that used in this analysis. The material properties of the physical shells cannot be compared to those used in this analysis because these properties are not reported in the literature and were not determined by the experimentalist. However, the predictions of the finite element analysis compare well against the experimentally measured strains.

## **5.7 DISCUSSION**

In the case of cylindrical shells composed of isotropic materials, the stiffness is constant through the thickness. Thus, for such shells subjected to a plane strain condition and biaxial loads, the axial stress is constant through the thickness, and the circumferential stress is nearly constant through the thickness. The average values of these stress components, therefore, represent a good description of the stress state developed in the shell.

When analysing cylindrical shells, piping, and pressure vessels constructed using isotropic materials, designers conventionally compare the average values of the axial and circumferential components of stress against known yield points or ultimate failure points of the material used in order to determine a factor of safety. Since these average stress values represent a good description of the stress state developed, the calculated factor of safety also represents a good indication of the proximity to yield or ultimate failure of the component when loaded.

The stress variation through the thickness of the multi-directional composite shell, plotted in Figures 5-2a to 5-2d, is not constant or nearly constant. This effect is particularly evident in Figure 5-2d, which is a plot of the variation of stress through the thickness for purely axial loading. This figure shows that the axial stress developed in the zero degree layer is nearly 3 times greater than the stress developed in the other layers in the shell. A similar observation can be made for the biaxial load ratios 1H:1A and 1H:0A, shown in Figures 5-2c and 5-2a, respectively. Thus, the values of the average axial stress and average circumferential stress do not represent a good indication of the stress state developed in the multi-directional shells subjected to combined internal pressure and axial loading.

The strain variation through the thickness of the multi-directional composite shell, plotted in Figures 5-3a to 5-3d, is constant or nearly constant. That is, there are no regions where the average strain across the section differs significantly from the developed strain. Therefore, the average strain across the section does represent a good indication of the strain developed in the multi-directional shells subjected to combined internal

pressure and axial loading.

Based on the stress/strain response predicted by this analysis, average stress does not correspond well to the stress state developed in multi-directional cylindrical shells subjected to biaxial loading conditions. However, average strain does correspond well to the strain developed in multi-directional cylindrical shells subjected to biaxial loading conditions. Thus, if a criterion were to be developed in order to compare the stress or strain state of multi-directional composite cylindrical shells against a yield point or an ultimate failure point, the results of this analysis would suggest that this criterion should be based in terms of strain rather than in the stress.

## 5.8 CONCLUSIONS

It was the goal of this study to determine stress/strain response of multi-directional fibre reinforced composite cylindrical shells subjected to various ratios of combined axial load and internal pressure. A multi-directional cylindrical shell with the ply stacking sequence [ $\pm 70^\circ, \pm 45^\circ, \pm 45^\circ, -70^\circ, 0^\circ, -45^\circ, \pm 45^\circ, \pm 45^\circ, \pm 45^\circ, \pm 45^\circ$ ] was modelled using the finite element method, and combined internal pressure and axial loading conditions were simulated. A stress/strain analysis of the developed model was performed using the program ANSYS. The finite element predictions were compared against experimental results found in the literature.

The results of the finite element analysis performed can lead to the following conclusions:

- I. The finite element results were used to show that the stress developed in each layer of the multi-directional cylindrical shells is dependent on the ply stacking angle of the particular layer.
- II. It was demonstrated that the stress/strain response trends of multi-directional composite cylindrical shells subjected to combined internal pressure and axial load can be predicted using the finite element method.
- III. The average value of the stress across a section through the thickness of multi-directional composite cylindrical shells does not represent a good indication of the stress developed in the section.
- IV. The average value of the strain across a section through the thickness for multi-directional composite cylindrical shells does represent a good indication of the strain developed in the section.
- V. The multi-directional composite cylindrical shells studied would be effective in carrying both axial loads and internal pressure, applied individually or in combination.
- VI. The strain response predicted by the numerical analysis was found to compare well with the measured results from physical experiments.

**Table 5-1**

**Biaxial Load Ratios Considered**

Hoop Stress : Axial Stress	
1:0	(pure internal pressure)
2:1	(pressure vessel loading)
1:1	
0:1	(pure axial loading)

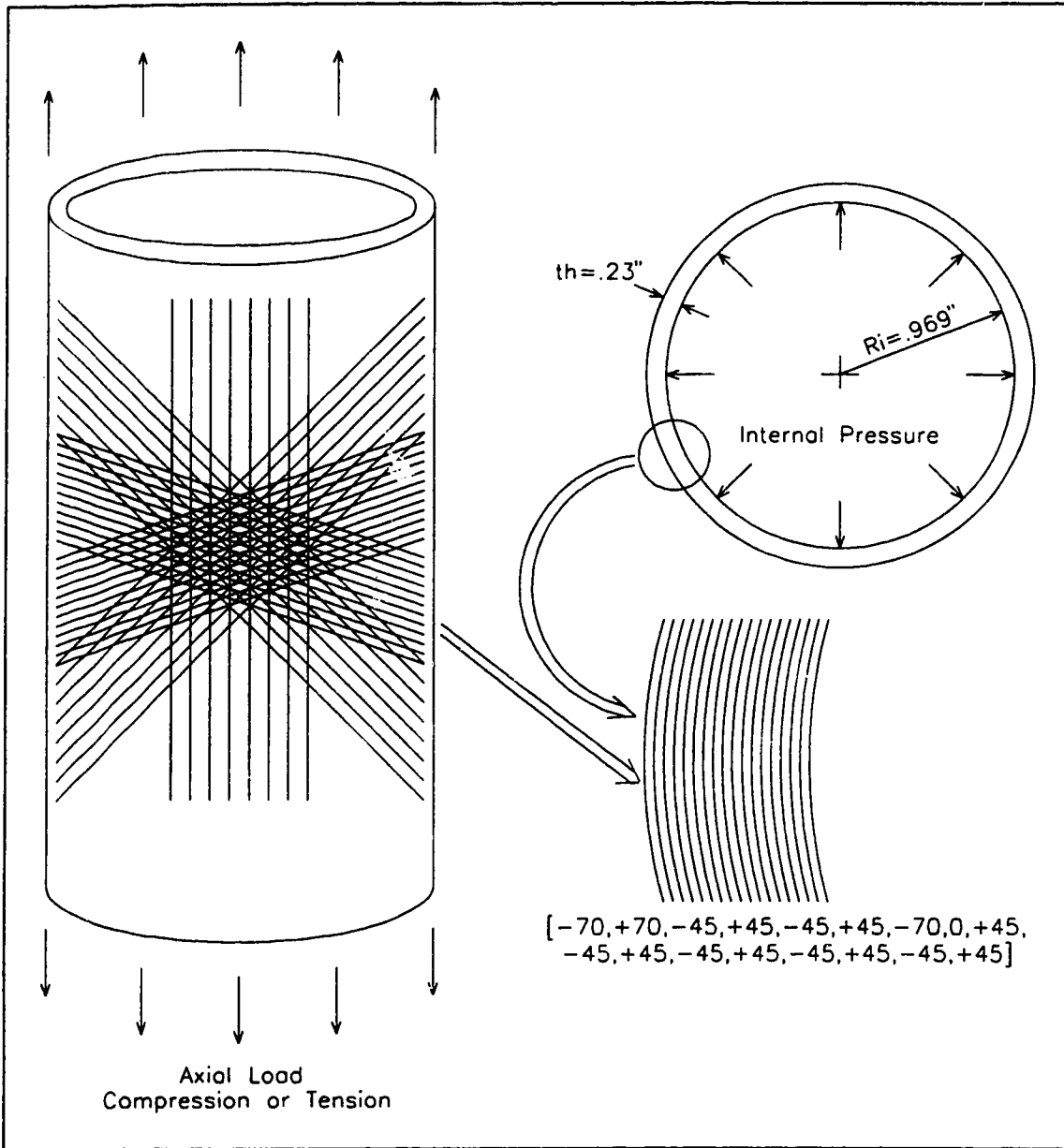


Figure 5-1 Sketch of shell geometry and direction notation.

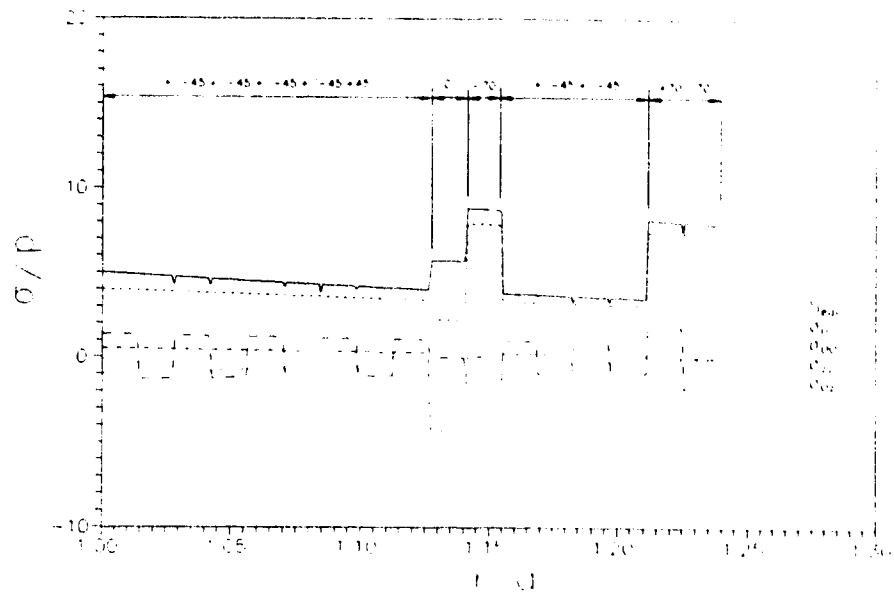


Figure 5-2a Variation of stress through the thickness for a biaxial load ratio of 1H:0A.

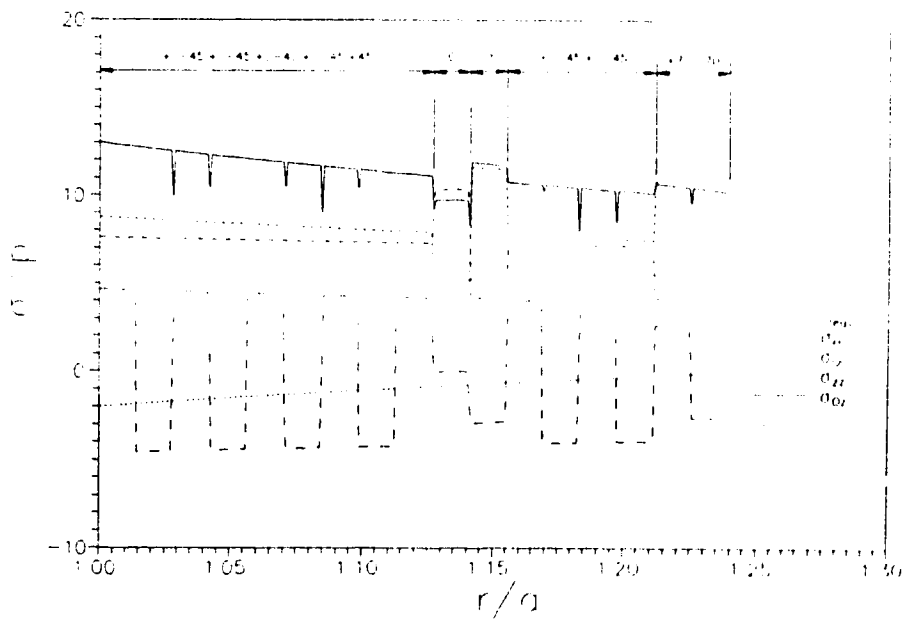


Figure 5-2b Variation of stress through the thickness for a biaxial load ratio of 2H:1A.

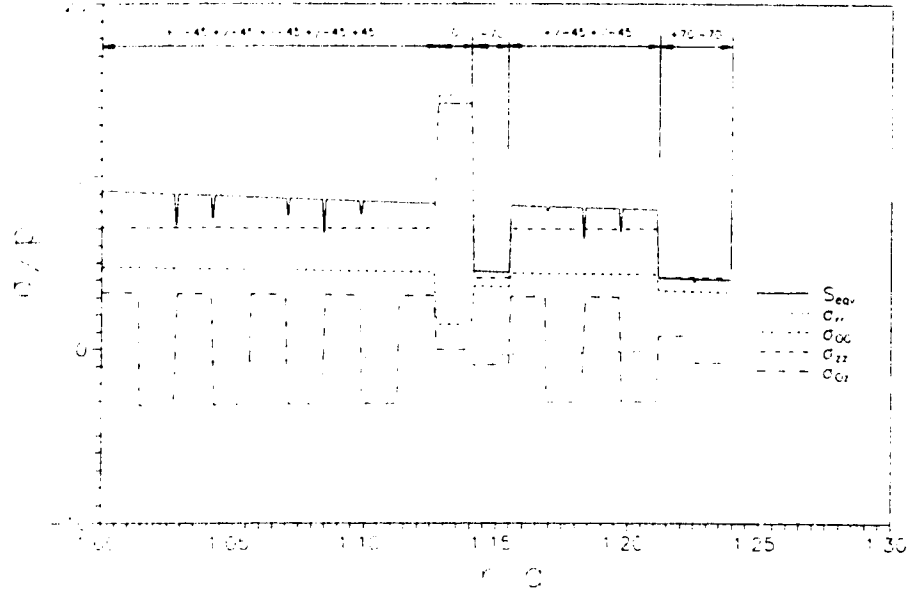


Figure 5-2c Variation of stress through the thickness for a biaxial load ratio of 1H:1A.

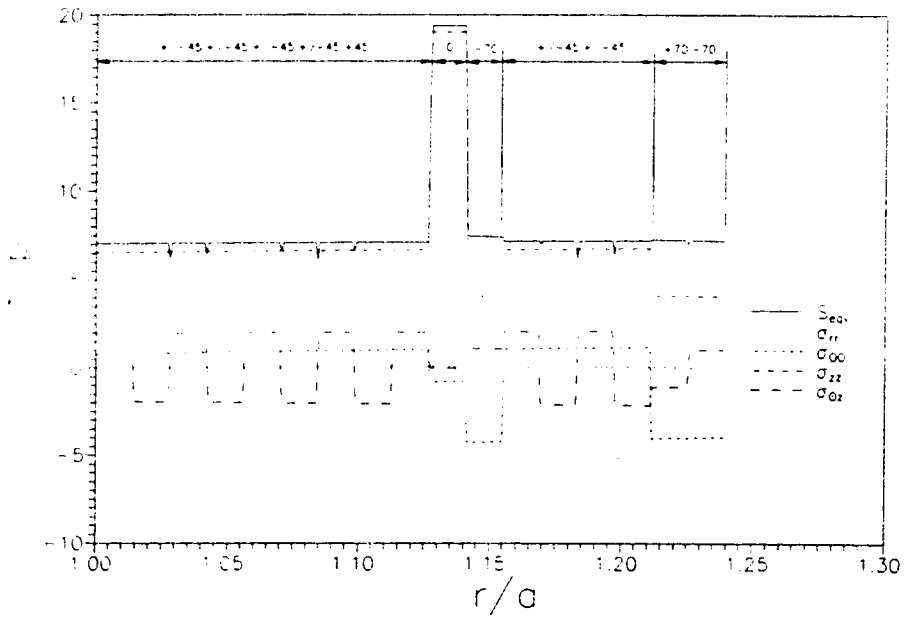


Figure 5-2d Variation of stress through the thickness for a biaxial load ratio of 0H:1A.



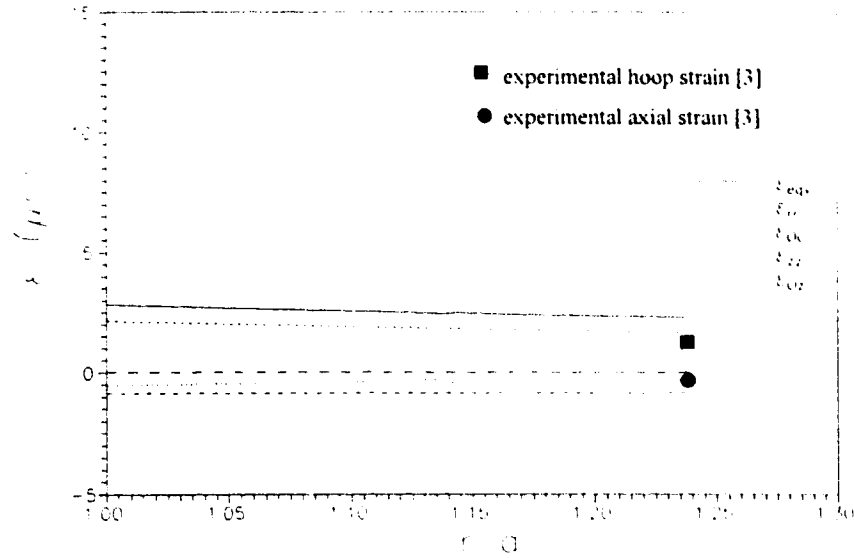


Figure 5-3a Variation of strain through the thickness for a biaxial load ratio of 1H:0A. The measured strain from a physical experiment [3] is superimposed on this plot.

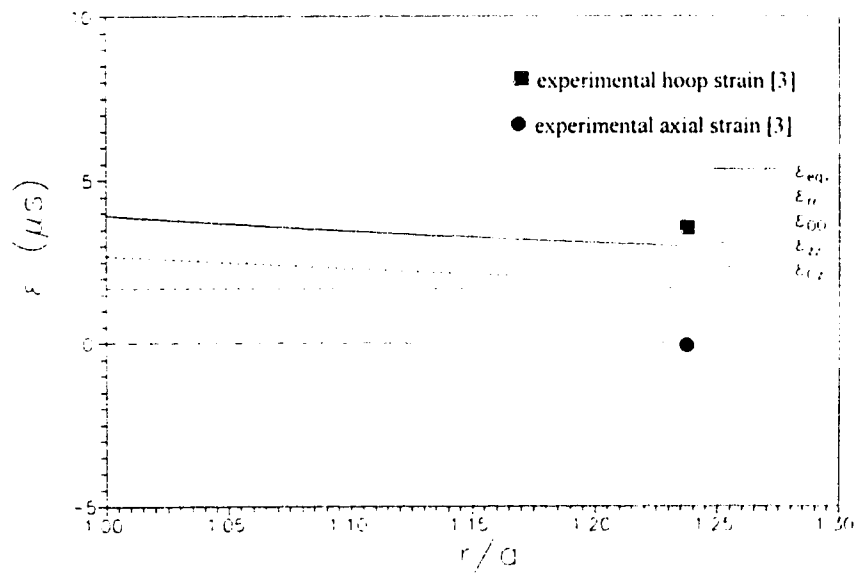


Figure 5-3b Variation of strain through the thickness for a biaxial load ratio of 2H:1A. The measured strain from a physical experiment [3] is superimposed on this plot.

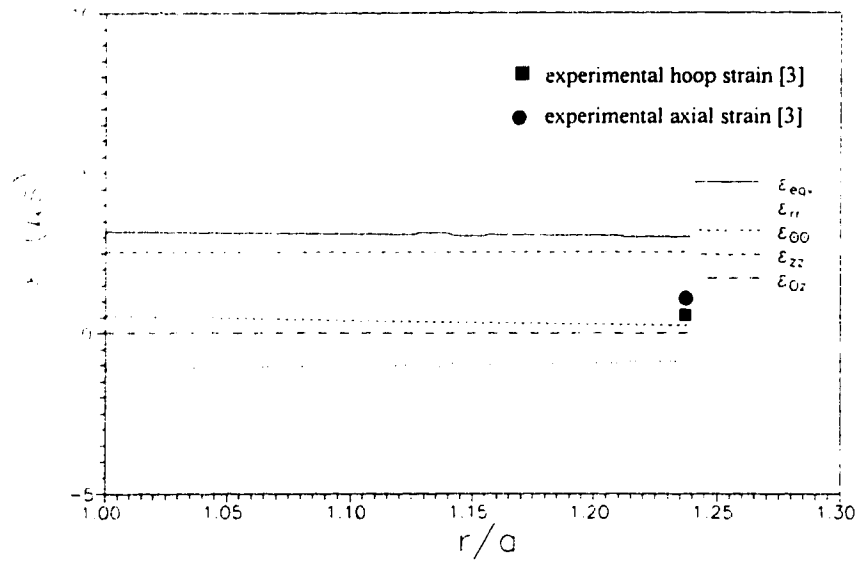


Figure 5-3c Variation of strain through the thickness for a biaxial load ratio of 1H:1A. The measured strain from a physical experiment [3] is superimposed on this plot.

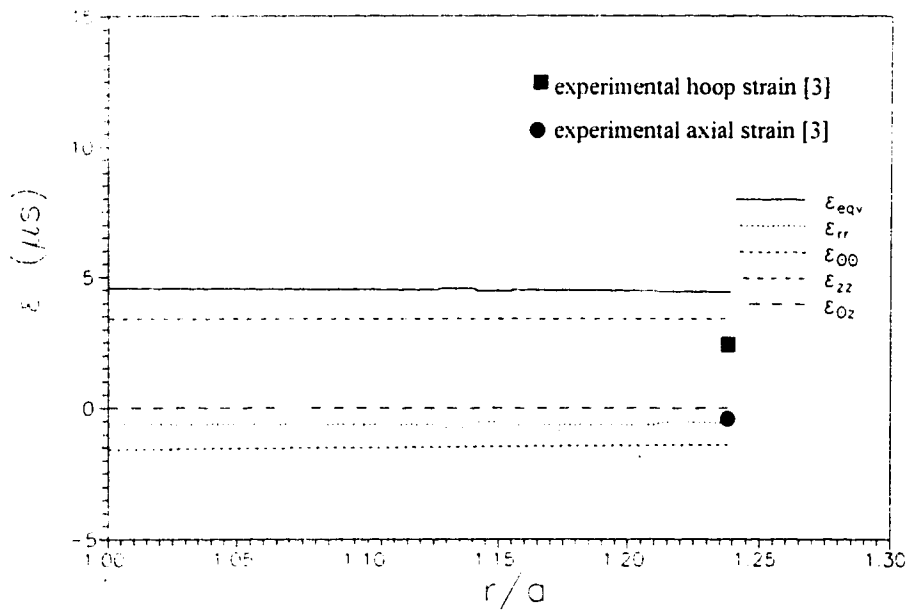


Figure 5-3d Variation of strain through the thickness for a biaxial load ratio of 0H:1A. The measured strain from a physical experiment [3] is superimposed on this plot.

## REFERENCES

- [1] Engineered Materials Handbook (1988), Vol. 1, Composites, ASM INTERNATIONAL, p. 144.
- [2] Timoshenko, S. (1956), Strength of Materials, Part II, Advanced Theory and Problems, D. Van Nostrand Company, Inc., New York, NY, USA.
- [3] Carroll, M. (1994). " Lay-up Rate Effects on Fibreglass/Epoxy Laminates and Tubulars", M.Sc. Thesis, University of Alberta, Edmonton, Alberta, p. 107-109.

## **CHAPTER 6**

### **CONCLUSIONS**

Four internal pressure problems for which there are no analytical solutions have been analysed using the finite element method. Syncrude Canada Limited's coker burner vessels are large steel pressurized vessels 54 feet [17 m] in diameter and 68 feet [21 m] tall. The extremely large size of these vessels and the 14 nozzles piercing them represent complex geometry that is not amenable to analytical studies. Pressurized laminate composite cylindrical shells with the general lay-up  $[+\theta, -\theta, +\theta, +\theta, -\theta, +\theta]$  and multi-directional laminate composite cylindrical shells represent another problem for analysts because the material properties of such shells vary through their thickness, and for thick walled vessels the classical laminate theory may not apply. Finite element models of the coker burner pressurized vessels and the pressurized composite shells were developed, and stress/strain analyses were performed.

The results from these analyses have provided an insight into the stress-strain and displacement responses of the pressure vessels considered, and have also pointed out design guides for pressure vessels.

#### **ANALYSIS OF A LARGE STEEL PRESSURIZED VESSEL**

A finite element model of Syncrude Canada Limited's two coker burner pressurized vessels complete with all of the vessels' major nozzle openings was developed in order to

determine the stress-strain and displacement response of the pressure vessels subjected to an internal pressure. This analysis was accomplished by applying the finite element submodelling technique in a new way that overcomes the difficulty of obtaining an adequate element discretization of curved and complex pressure vessel geometry.

The results from this analysis demonstrated that heavy reinforcement pads used on the shell side of nozzle-shell junctures constrain the shell such that a part of the load is carried by bending. Carrying the load by bending is not as efficient as by membrane, and stress concentrations and bending deformation are evident at the reinforcement pad boundaries. The results show that the required reinforcement located in the nozzle wall instead of the shell wall would permit the shell to deflect close to a membrane fashion. Thus, the results were used to increase the information on the effect of nozzle reinforcement configurations on the stress-strain response of the pressure vessel shell.

The plastic limit of two of the nozzle-shell intersection regions of the coker burner pressure vessels were determined for the case of combined external loading and internal pressure. Inplane or outplane moments combined with internal pressure and inplane or outplane shear forces combined with internal pressure were simulated and an elastic-plastic analysis was performed. The results of this analysis were used to demonstrate that combined outplane moment and internal pressure is the critical case of the loading combinations considered. These results were also used to calculate the elastic stiffnesses of the nozzle-shell connections. This information is valuable to piping designers in order for them to take advantage of the flexibility of the shell. Without this information, piping must be designed under the conservative assumption of an infinitely stiff shell.

The results from these analyses were compared quantitatively and qualitatively to results from physical experiments found in the literature and found to agree well. However, it was noted that the peak stresses at nozzle-shell intersections can be 50% lower than that reported from the experiments. Therefore, it is concluded that finite element results should be interpreted and evaluated by those who are qualified in the methods and interpretation of finite element techniques and results.

### **ANALYSIS OF PRESSURIZED LAMINATED CYLINDRICAL SHELLS**

A laminated composite cylindrical shell with the general ply stacking sequence  $(-\theta, -\theta, +\theta, +\theta, -\theta, +\theta)$  was modelled using the finite element method in order to determine the angle  $\theta$  that would yield minimum diametral strain. The results from this analysis were used to demonstrate that the angle  $\theta$  which yields minimum diametral strain is dependent on the ratio of the average circumferential stress to the average axial stress. This conclusion suggests that the ply stacking angle  $\theta$  must be designed for the specific end use loading conditions in order to minimize the diametral strain with the most efficient use of material. As well, the results from this analysis were used to show that no significant reduction in diametral strain is achieved by increasing the ply stacking angle  $\theta$  above  $70^\circ$  for biaxial load ratios that are hoop stress dominant. The displacement results from this analysis were compared quantitatively against experimental results from the literature and found to agree to within 25%.

Laminated composite cylindrical shells with the multi-directional ply stacking

sequence [ $\pm 70^\circ, \pm 45^\circ, \pm 45^\circ, -70^\circ, 0^\circ, -45^\circ, \pm 45^\circ, \pm 45^\circ, \pm 45^\circ, \pm 45^\circ$ ] were analysed in order to determine the stress-strain response of the shells. The results from this analysis were used to demonstrate that the variation of the stress through the thickness of the shells is strongly dependent on the orientation angle of the individual layers. The combination of fibres orientated at  $0^\circ$  and at  $70^\circ$  was shown to provide stiffness in the axial and in the circumferential directions, respectively. This conclusion suggests that the multi-directional composite cylindrical shells considered will perform well under combined or individual internal pressure and axial loading.

These results were also used to demonstrate that the average value of stress across a section through the thickness of multi-directional composite cylindrical shells does not represent a good indication of the stress developed in the section. The average value of strain for such shells, however, does represent a good indication of the strain developed in the section.

The strain results from the analysis of the multi-directional shells were compared against the strain measurements from physical experiments from the literature and found to agree well.

## **APPENDIX A**

### **SUBMODELLING TECHNIQUE DETAILS**

The finite element mesh of the burner vessel global model is too coarse to obtain satisfactory results in the nozzle-shell intersection regions because of the high local stress gradients developed in these regions. The mesh of this model is adequate, however, to produce accurate results away from these regions. The submodelling technique was used in order to improve the accuracy of the results in the nozzle-shell intersection regions.

In order to improve on the results of the burner vessel global model, there were two options available. The first was to reanalyse the entire global model with greater mesh refinement. The second was to develop a more finely meshed model of only the nozzle-shell intersection region. The first option was considered too costly to be practical because of the analysis time and hardware requirements. Further, the curved geometry typical of pressure vessels makes this first option very difficult or impossible. The latter option is the submodelling technique. With this technique, the boundary of the submodel represents a cut through the global model. Displacement results from the finite element solution of the global model are prescribed as the displacement boundary conditions for the submodel. This technique is illustrated in Figure A-1.



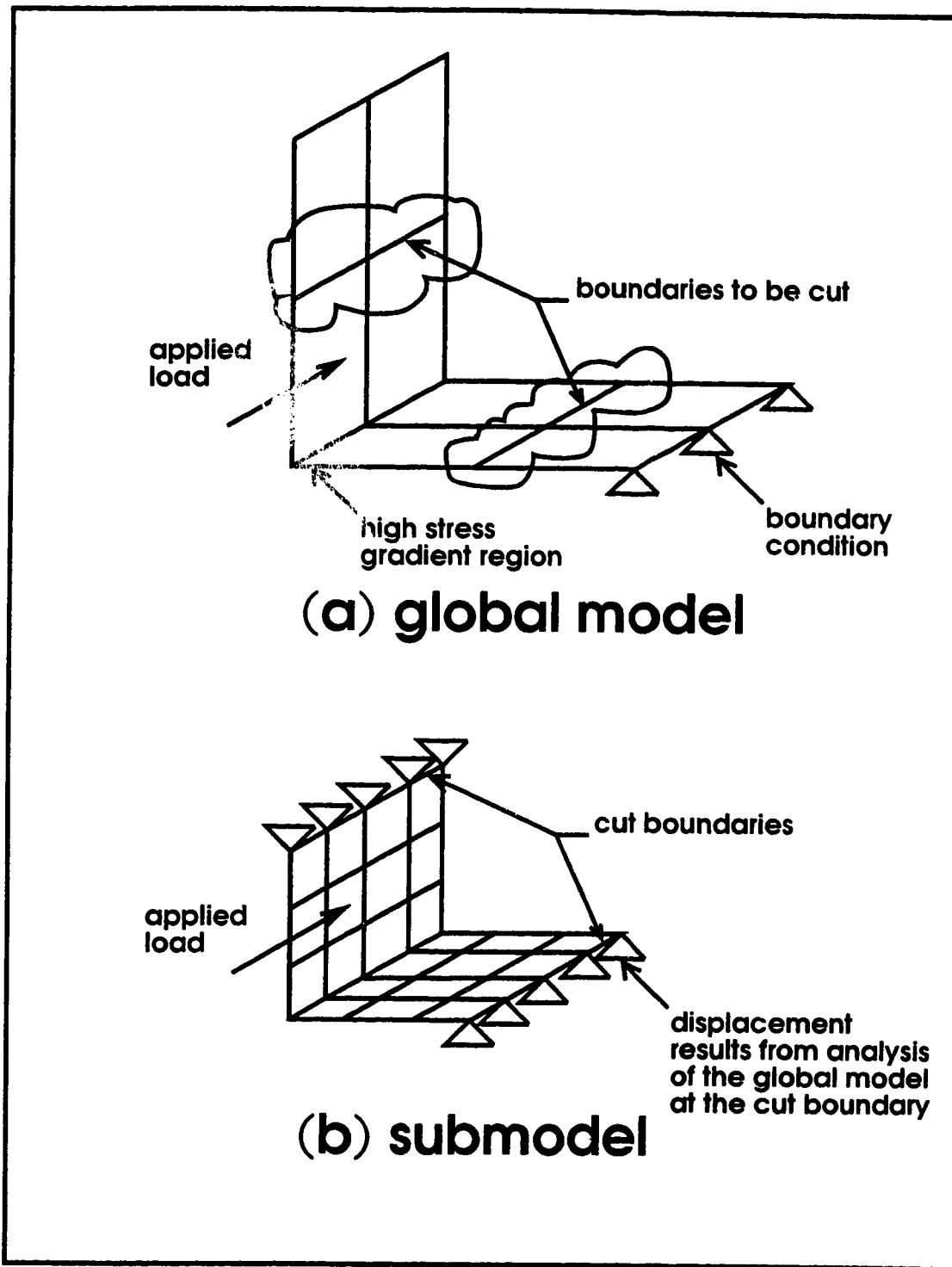


Figure A-1: Example of the submodelling technique. The finite element displacement results from the global model analysis are prescribed as displacement boundary conditions on the cut boundary of the submodel.

## APPENDIX B

### SHELL ELEMENT DETAILS

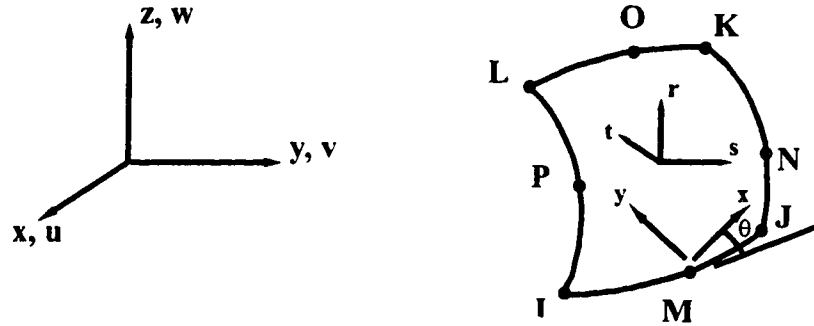


Figure B-1: Direction notation and nodal labelling for SHELL93 nodal degrees of freedom.

The ANSYS program's SHELL93 8 node shell element uses the displacement shape functions given by Equations B.1, B.2, and B.3. The direction notation for  $u$ ,  $v$ , and  $w$  and the nodal labelling scheme is illustrated in Figure B-1.

$$\begin{Bmatrix} u \\ v \\ w \end{Bmatrix} = \sum_{i=1}^8 N_i \begin{Bmatrix} u_i \\ v_i \\ w_i \end{Bmatrix} + \sum_{i=1}^8 N_i \frac{r_i}{2} \begin{bmatrix} a_{1,i} & b_{1,i} \\ a_{2,i} & b_{2,i} \\ a_{3,i} & b_{3,i} \end{bmatrix} \begin{Bmatrix} \theta_{x,i} \\ \theta_{y,i} \end{Bmatrix} \quad (\text{B.1})$$

where:

$$\begin{aligned} N_i = & \frac{1}{4} ((1-s)(1-t)(-1-s-t) + (1+s)(1-t)(-1+s-t) \\ & + (1+s)(1+t)(-1+s+t) + (1-s)(1+t)(-1-s+t) \\ & + (1-s)(1-s)(1-t) + (1+s)(1-t)(1-t) \\ & + (1-s)(1-s)(1+t) + (1-s)(1-t)(1-t)) \end{aligned} \quad (\text{D.3})$$

and

- $u_i, v_i, w_i$  = motion of node  $i$
- $r$  = thickness coordinate
- $t_i$  = thickness at node  $i$
- $\{a\}$  = unit vector in  $s$  direction
- $\{b\}$  = unit vector in plane of element normal to  $\{a\}$
- $\theta_{s,i}$  = rotation of node  $i$  about vector  $\{a\}$
- $\theta_{b,i}$  = rotation of node  $i$  about vector  $\{b\}$

## Stress-Strain Relationships

Equation B.2 gives the stress strain relationship used to calculate the stress components for each element:

$$\begin{Bmatrix} \sigma_{11} \\ \sigma_{22} \\ \sigma_{33} \\ \sigma_{23} \\ \sigma_{13} \\ \sigma_{12} \end{Bmatrix} = \begin{bmatrix} BE & B\nu E & 0 & 0 & 0 & 0 \\ B\nu E & BE & 0 & 0 & 0 & 0 \\ 0 & 0 & 0 & 0 & 0 & 0 \\ 0 & 0 & 0 & G & 0 & 0 \\ 0 & 0 & 0 & 0 & G/f & 0 \\ 0 & 0 & 0 & 0 & 0 & G/f \end{bmatrix} \begin{Bmatrix} \epsilon_{11} \\ \epsilon_{22} \\ \epsilon_{33} \\ \epsilon_{23} \\ \epsilon_{13} \\ \epsilon_{12} \end{Bmatrix} \tag{B.2}$$

$$B = 1/(1-\nu^2)$$

where:

$$f = \left\{ \begin{array}{l} 1.2 \\ 1.0 + 0.2 \frac{A}{25t^2} \end{array} \right\}, \text{ whichever is greater}$$

$$E_x = \text{Elastic Modulus} \tag{D.2}$$

$$\nu = \text{Poisson's Ratio}$$

$$G = \frac{E}{2(1+\nu)}$$

The properties used for these material constants in this analysis are detailed in Section 2.2. This stress strain relationship assumes that the material properties are isotropic.

## APPENDIX C

### PLASTIC LIMIT LOAD DETAILS

The purpose of this appendix is to detail the calculation of the plastic limit loads of nozzles S6 and N7 opening into Syncrude Canada Limited's coker burner pressure vessels. The loading conditions considered are internal pressure combined with external outplane moment, internal pressure combined with external inplane moment, internal pressure combined with external outplane shear, and internal pressure combined with external inplane shear. The limit loads herein calculated are discussed in detail in Chapter 3 and summarised in Table 3-1 of this thesis.

The calculation of the limit loads was performed using the intersection of the elastic response and the tangent of the plastic behaviour. Figure 3-5 demonstrates this approach. The external load - deflection response of the nozzle intersection regions is plotted in Figures C-1 to C-6. Superimposed on each of these figures are two dashed lines tangent to the elastic and plastic response, respectively. The plastic limit load is defined as the magnitude of the external load at the intersection point of these two lines.

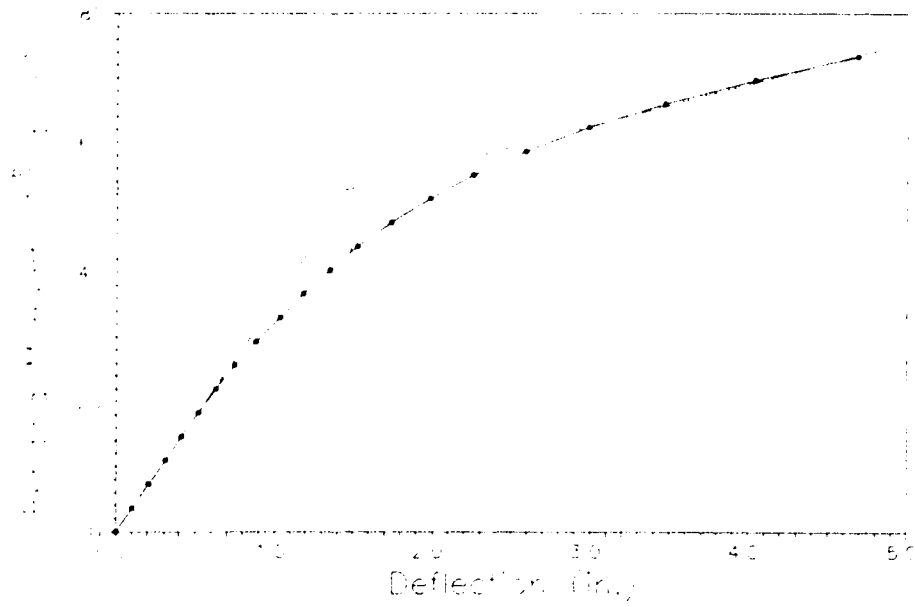


Figure C-1: Bending moment verses deflection for nozzle S6 subjected to an outplane bending moment.

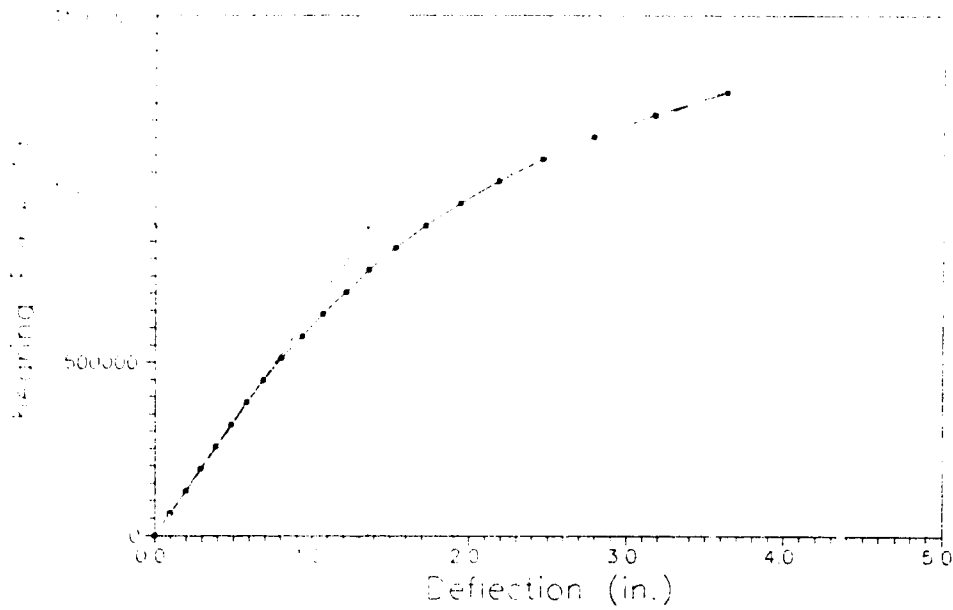


Figure C-2: Shearing load verses the deflection for nozzle S6 subjected to an inplane shearing force.

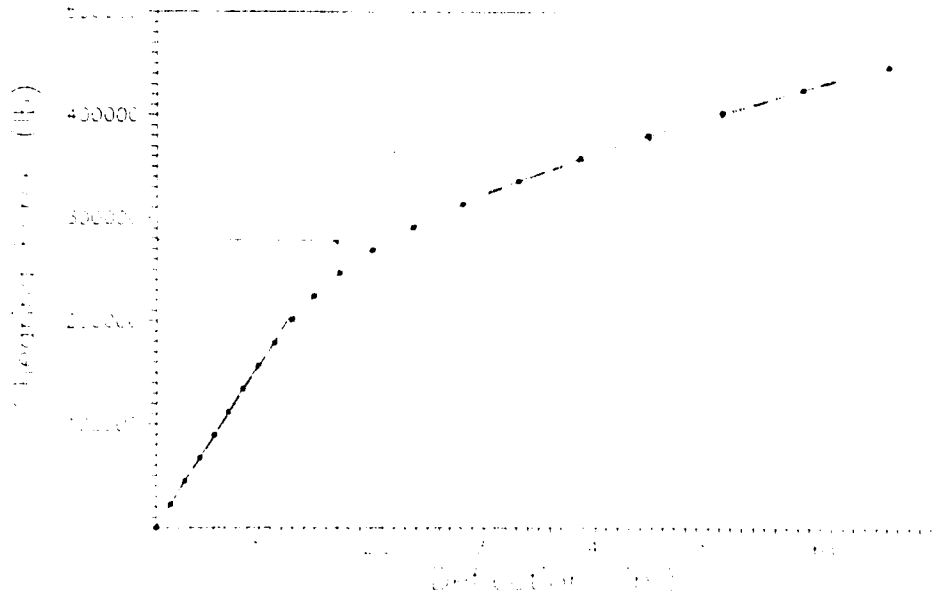


Figure C-3: Shearing load versus deflection for nozzle N7 subjected to an inplane shearing force.

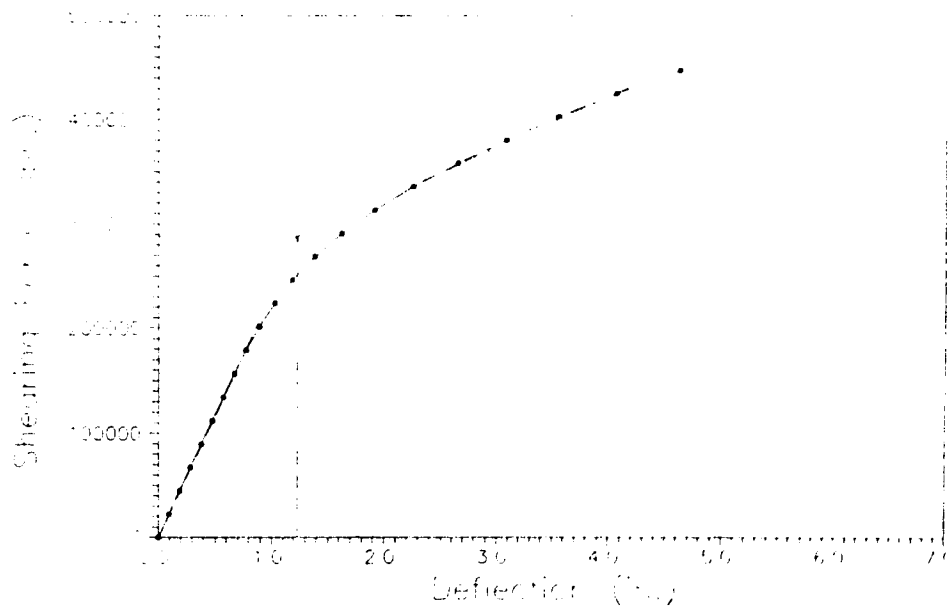


Figure C-4: Shearing load versus deflection for nozzle N7 subjected to an outplane shearing

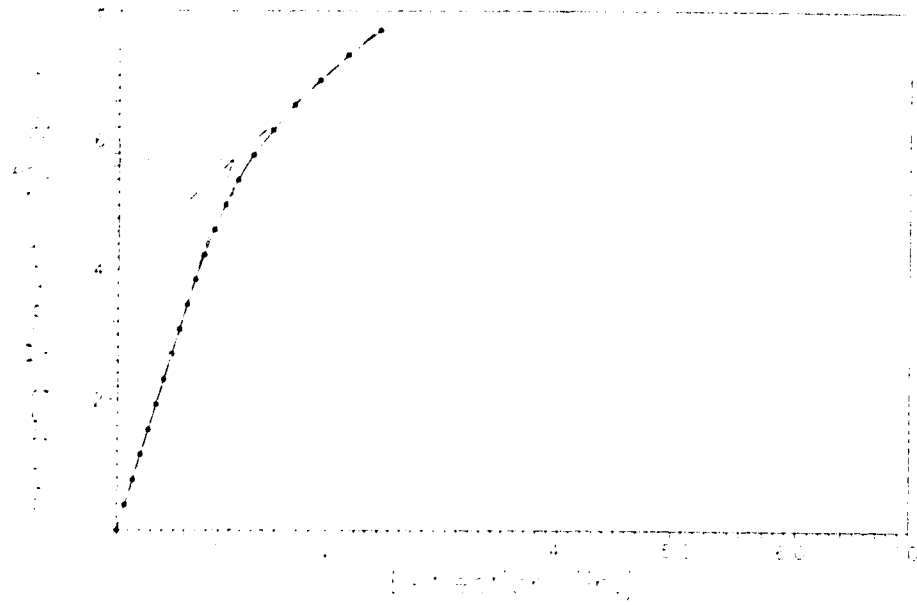


Figure C-5: Bending moment verses deflection for nozzle N7 subjected to an inplane moment.

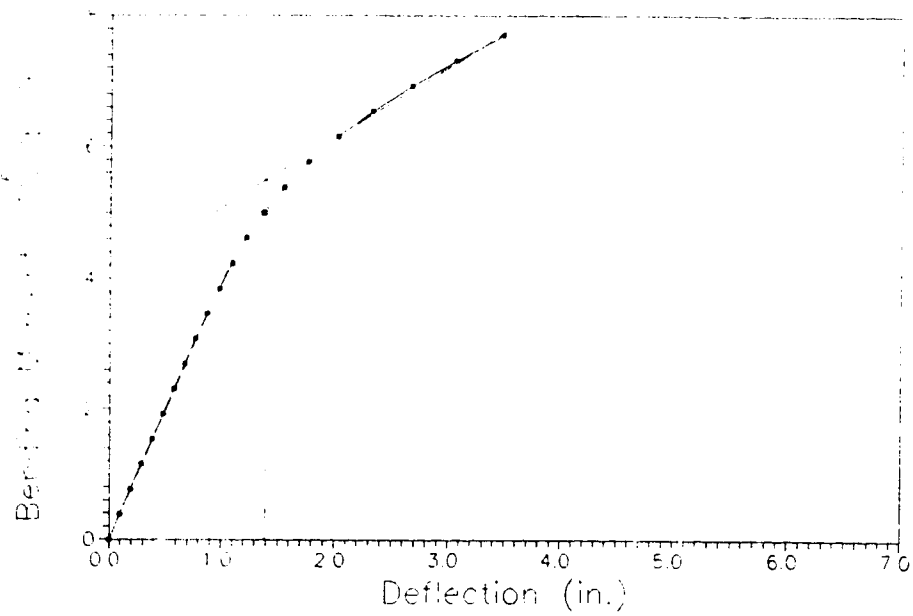


Figure C-6: Bending moment verses deflection for nozzle N7 subjected to an outplane bending moment.



## APPENDIX D

### BRICK ELEMENT DETAILS

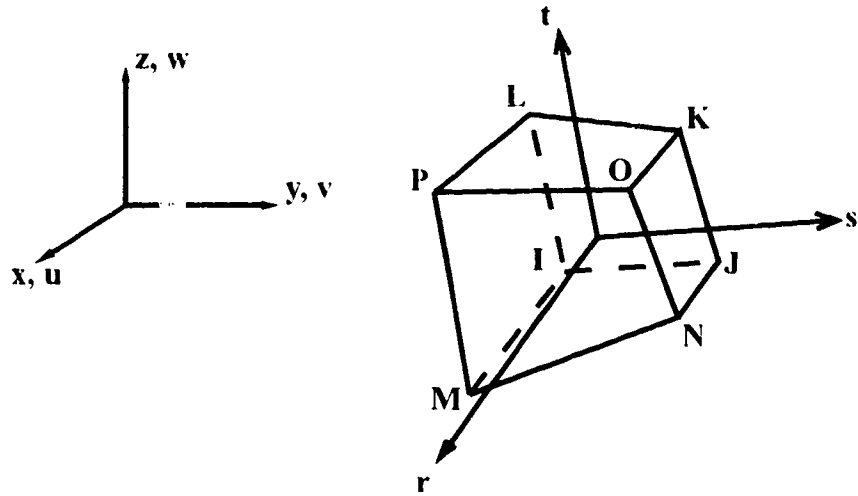


Figure D-1: Direction notation for SOLID64 displacements and nodal degrees of freedom.

The ANSYS program's SOLID64 8 node brick element uses the displacement shape functions given by Equations D.3, D.4, D.5, and D.6. The direction notation for  $u$ ,  $v$ , and  $w$  and the nodal labeling scheme is illustrated in Figure D-1.

$$\begin{aligned}
 u = \frac{1}{8} & (u_I (1-s)(1-t)(1-r) + u_J (1+s)(1-t)(1-r) \\
 & + u_K (1+s)(1+t)(1-r) + u_L (1-s)(1+t)(1-r) \\
 & + u_M (1-s)(1-t)(1+r) + u_N (1+s)(1-t)(1+r) \\
 & + u_O (1+s)(1+t)(1+r) + u_P (1-s)(1+t)(1+r))
 \end{aligned} \tag{D.3}$$

$$\begin{aligned}
 v = \frac{1}{8} & (v_I (1-s)(1-t)(1-r) + v_J (1+s)(1-t)(1-r) \\
 & + v_K (1+s)(1+t)(1-r) + v_L (1-s)(1+t)(1-r) \\
 & + v_M (1-s)(1-t)(1+r) + v_N (1+s)(1-t)(1+r) \\
 & + v_O (1+s)(1+t)(1+r) + v_P (1-s)(1+t)(1+r))
 \end{aligned} \tag{D.4}$$

$$\begin{aligned}
 w = & \frac{1}{8} (w_J (1-s)(1-t)(1-r) + w_I (1+s)(1-t)(1-r) \\
 & + w_K (1+s)(1+t)(1-r) + w_L (1-s)(1+t)(1-r) \\
 & + w_M (1-s)(1-t)(1+r) + w_N (1+s)(1-t)(1+r) \\
 & + w_O (1+s)(1+t)(1+r) + w_P (1-s)(1+t)(1+r))
 \end{aligned} \tag{D.5}$$

$$u_i, v_i, w_i = \text{motion of node } i \tag{D.6}$$

No rotational degrees of freedom are present in the formulation of the SOLID64 element, and this is consistent with the axisymmetric analyses performed of the laminated shells.

### Stress-Strain Relationships

Equation D.1 gives the stress strain relationship for a transversely isotropic material consistent with the three dimensional model used in the analysis of the laminated cylindrical shells.

$$\begin{Bmatrix} \epsilon_{11} \\ \epsilon_{22} \\ \epsilon_{33} \\ \epsilon_{23} \\ \epsilon_{13} \\ \epsilon_{12} \end{Bmatrix} = \begin{bmatrix} \frac{1}{E_1} & -\frac{\nu_{12}}{E_1} & -\frac{\nu_{12}}{E_1} & 0 & 0 & 0 \\ -\frac{\nu_{12}}{E_1} & \frac{1}{E_2} & -\frac{\nu_{23}}{E_2} & 0 & 0 & 0 \\ -\frac{\nu_{12}}{E_1} & -\frac{\nu_{23}}{E_2} & \frac{1}{E_2} & \frac{2(1+\nu_{23})}{E_2} & 0 & 0 \\ 0 & 0 & 0 & 0 & \frac{1}{G_{12}} & 0 \\ 0 & 0 & 0 & 0 & 0 & \frac{1}{G_{12}} \\ 0 & 0 & 0 & 0 & 0 & 0 \end{bmatrix} \begin{Bmatrix} \sigma_{11} \\ \sigma_{22} \\ \sigma_{33} \\ \sigma_{23} \\ \sigma_{13} \\ \sigma_{12} \end{Bmatrix} \tag{D.1}$$

The following relationships are assumed:

$$\begin{aligned}
 E_2 &= E_3 \\
 \nu_{12} &= \nu_{13} = \nu_{23} \\
 G_{12} &= G_{13} \\
 G_{23} &= \frac{E_3}{2(1 + \nu_{23})}
 \end{aligned}
 \tag{D.2}$$

Equation D.1 contains four independent material constants: E1, the elastic modulus along the fibre direction; E2, the elastic modulus transverse to the fibre direction;  $\nu_{12}$ , Poisson's ratio; and G12, the shear modulus. The properties used for these material constants in this analysis are detailed in Section 4.2.